Curved concrete crownwalls on vertical breakwaters

Finite Element Analysis

Lára Margrét Gísladóttir

Delft University of Technology

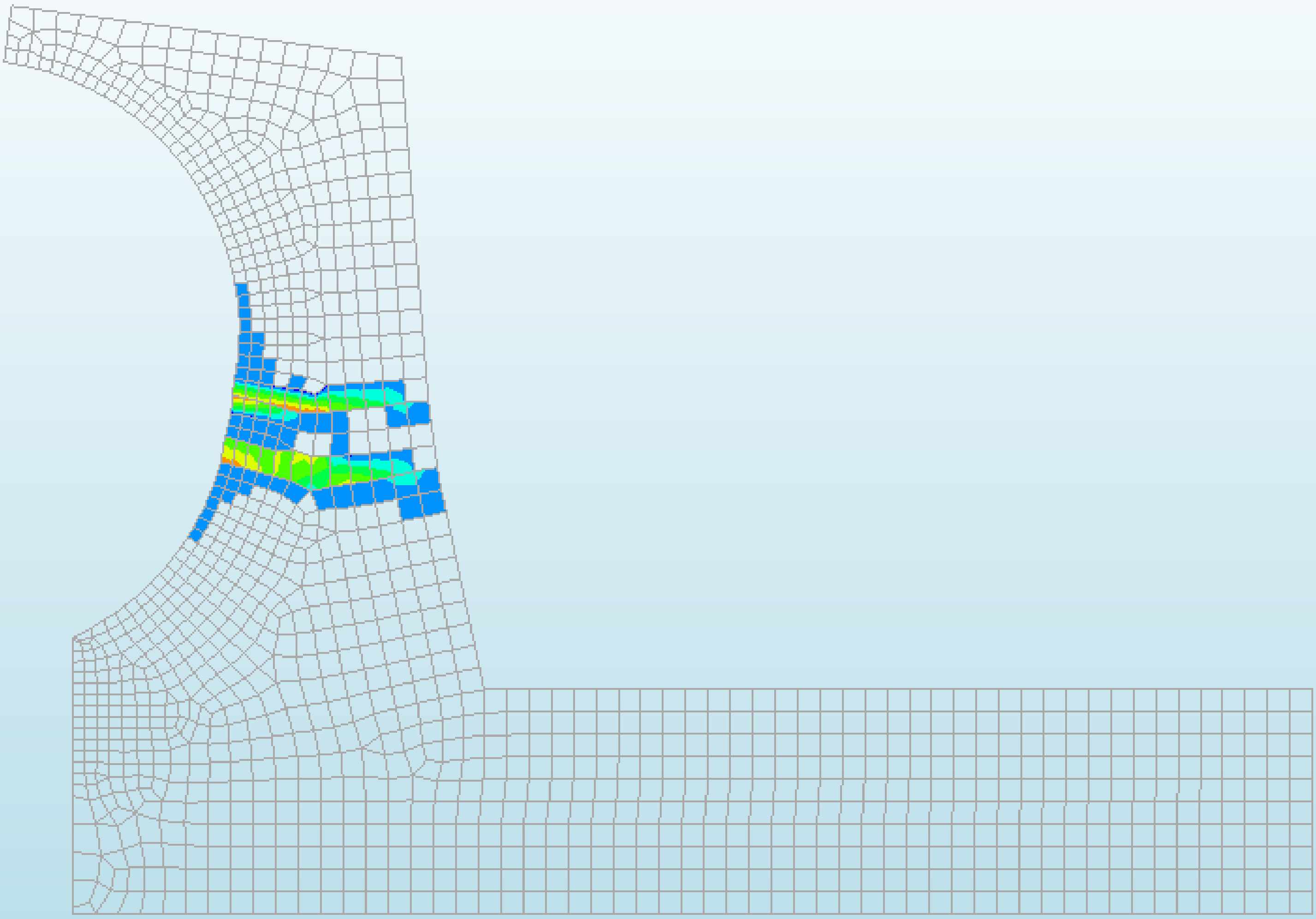

Curved concrete crownwalls on vertical breakwaters

Finite Element Analysis

by

L.M. Gísladóttir

in partial fulfilment of the requirements for the degree of Master of Science
at the Delft University of Technology,
to be defended publicly on Friday February 24, 2023.

Student number:	5363543	
Thesis committee:	Dr. ir. A. Antonini,	TU Delft, supervisor
	Ir. D. Dermentzoglou,	TU Delft
	Prof. dr. ir. M. A. N. Hendriks,	TU Delft
	Prof. dr. ir. M. R. A. van Gent,	TU Delft
	Dr. ir. M. Castellino,	Sapienza University of Rome

Preface

This master's thesis, titled ”Curved concrete crownwalls on vertical breakwaters”, is the final project to finish my master's degree in Structural Engineering, specialising in Hydraulic Structures, at TU Delft. Throughout my studies, I developed an interest in the dynamics of ocean waves and wave loading on structures. I am, therefore, very thankful that I had the opportunity to work on this topic during my thesis, as it combines the fields of wave loading by ocean waves and structural engineering very well.

This thesis would not have been possible without the help of my thesis committee, who all gave valuable guidance. First, I would like to thank Alessandro Antonini, the chair of my thesis committee and daily supervisor, for always being available for me when I needed assistance and giving me very valuable advice on how to progress with my work. I would also like to thank Myrta Castellino for all her help and for coming up with the idea of analysing a fully curved crownwall and providing me with all the data I needed to perform this analysis. I am very thankful to Max Hendriks for helping me with the finite element modelling of the structure and for all the advice regarding the structural dynamics part of the project. I thank Dimitris Dermentzoglou for sharing his knowledge on the subject and methodology, and for his insightful suggestions throughout the project. Finally, I thank Marcel van Gent for showing interest in my thesis project and giving valuable input to improve the quality of the project.

I would like to give special thanks to my family and boyfriend, Sigurður, for their endless love and encouragement. I am very grateful for having been able to share this academic journey with Sigurður, who is also finishing his master's degree in Structural Engineering. Their support has allowed me to reach my goals and finish this degree.

Lára Margrét Gísladóttir
Delft, February 2023

Summary

Crownwalls are often placed on top of vertical composite breakwaters to reduce overtopping. Adding a seawards facing overhang (recurve or bullnose) at the top of crownwalls has successfully reduced overtopping even further without increasing the freeboard of the crownwall. Vertical breakwaters are often placed in deep water conditions meaning that the structure is subjected to non-breaking waves. However, studies have shown that recurved crownwalls can be subjected to impulsive wave loads due to the *Confined-Crest Impact* (C-CI) phenomenon (Castellino et al., 2018a). The confinement of the wave, by the recurve, creates the impulsive nature of the force, as at the moment the wave is deflected seawards, at a high-speed flow, the incoming wave crest stops the return flow. These large impulsive pressures can cause the failure of crownwalls, as happened to the recurved crownwall in Civitavecchia Harbour, Italy.

Various recurves and overhangs have been designed and applied to vertical breakwater crownwalls. The effects of different geometries have also been studied, such as different exit angles, radii and lengths of overhang. Crownwalls with a fully curved face are most often used in seawalls where they are subjected to wave load by breaking waves, but using the fully curved shape for a vertical breakwater crownwall has recently been tested with physical model tests by Dermentzoglou (2021). That study showed that wave loading on the fully curved crownwall was increased compared to a vertical crownwall. This thesis aims to investigate further the wave loading by non-breaking waves and the dynamic response of a fully curved crownwall and compare it to the well-known shape of a recurved crownwall. Pressure-time series from CFD numerical simulations of three different wave states will be analysed to determine how the structure is loaded, as the wave load can be quasi-static, dynamic or impulsive. It will also be investigated whether the C-CI phenomenon occurs for the fully curved crownwall as it does for the recurved crownwall. Through offline one-way coupling of CFD-generated pressure-time series and a FEM model, the dynamic response of the fully curved crownwall will be analysed. This is the same method as used by Dermentzoglou et al. (2021) in their analysis of the recurved crownwall. The dynamic analysis will show whether the fully curved crownwall fails under the wave load by these wave states and its structural performance can be compared to that of the recurved crownwall under the same wave loading. In this thesis, it will also be investigated whether the wave load acting on the fully curved crownwall can be accurately calculated with the extension of Castellino et al. (2021) to the Goda method, for static wave load on recurved crownwalls.

Through CFD numerical simulations, wave pressure on the crownwall is measured for 100 s for three regular wave states: W5 with wave height $H = 5m$ and wave period $T = 8s$, W6 with $H = 6m$ and $T = 8s$ and W7 with $H = 7m$ and $T = 11s$. To obtain the total force, the pressure distribution at each time is integrated over the height of the crownwall. The pressure distributions at the moment of maximum total force show that for W6 and W7, the C-CI phenomenon is evident as there is a pressure increase at the top of the curve of the crownwall. For W5, however, the pressure distribution resembles the trapezoidal distribution. Due to the considerable wave steepness of W6, 6%, and the relatively large vertical wave velocity, $2.4m/s$, the largest wave hits the crownwall differently from other waves, which results in a maximum pressure located just above the centre of the curve and a relatively large total force. Waves with force and pressure impacts with an impulsive impact type are found in all three wave states. By integrating the pressure- and force-time series over the impact duration, the impulses can be determined. Both the force and pressure impulses are found to be much less variable than the maximum force and pressure values. The C-CI phenomenon is stronger for the recurved crownwall than the fully curved crownwall as the confinement of the wave is greater. However, due to the momentum the wave gains travelling up the fully curved face, the pressure and total force acting on the fully curved crownwall are larger. A more in-depth analysis of the CFD-generate wave load of

the fully curved crownwall is needed to understand better, for example, the loading by steep waves and the C-CI phenomenon for the fully curved shape.

The crownwall is modelled via the finite element analysis software Diana FEA 10.5. The model is in 2D with plane-strain elements and a linear material model for concrete in strength class C35/45. The crownwall is modelled both with (*supported*) and without (*unsupported*) an additional supporting wall behind it. The impulse duration of the pressure impulses in W6 and W7 are less than four times the natural period of the structure and are, therefore, in the dynamic domain of the crownwalls. Dynamic linear analysis of the unsupported and supported crownwalls shows that the tensile stresses in the centre of the curve of the crownwall exceed the tensile strength of the concrete for W6 and W7. For the recurved crownwall, the tensile stresses did not exceed the tensile strength of the concrete for any wave state. Nonlinear analysis of the fully curved crownwall further showed that cracks propagate through the entire cross-section of both the unsupported and supported crownwalls at the centre of the curve. This indicates total failure of the crownwalls. Having an additional supporting wall behind the crownwall did not significantly affect the failure, although the cracks were more concentrated in one area in the cross-section. The significant difference in the structural response of the fully curved and recurved crownwalls was found to be due to the significant difference in the bending moment exerted on the critical cross-section by the wave load. The width of the fully curved crownwall at the centre of the curve is equal to the width of the recurved crownwall, which also reduces the structural resistance. It is evident that steel reinforcement bars are needed to increase the structure's bending resistance or the width of the crownwall needs to be increased. Re-entrant corners and sharp changes in boundary conditions should also be avoided as they cause singularities in the stress field. Regarding the geometry of the curve of the crownwall, these results support the findings of other studies that increasing the radius of the curve increases the wave load.

The static wave load is calculated with the Goda method, using the extension of Castellino et al. (2021) to account for the C-CI phenomenon. The calculation method overestimates the wave load of all wave states, but the resulting pressure distribution is relatively close to the pressure distribution at the moment of maximum pressure as measured by the CFD numerical model. The largest difference is however for W6, where the pressure distribution is affected by the large wave steepness and vertical wave velocity, and does therefore not have the maximum pressure in the top of the curve of the crownwall, as assumed by the calculation method. The method is therefore considered useful for the preliminary design of fully curved crownwalls with wave steepness less than 6% and vertical wave velocity less than $2.4m/s$. However, as the wave load is transient and the pressure impulses are in the dynamic domain of the structure, the dynamic response can not be ignored in the final design. This can be done either with a dynamic analysis or by applying a sufficiently large dynamic amplification factor (DAF) to the static analysis. It should be kept in mind though that using a DAF to estimate the dynamic amplification might be an oversimplification of the dynamic response of the crownwall, as it is not an SDOF system.

It is concluded that the fully curved crownwall is less favourable than the recurved crownwall. For the same wave states, the fully curved crownwall is subjected to larger wave forces than the recurved crownwall. The fully curved crownwall is also larger than a recurved crownwall, with the same freeboard, and therefore requires more use of concrete. Due to the shape of the fully curved crownwall, the maximum tensile stresses are 2.5-3 times higher than those in the recurved crownwall. More use of steel reinforcement bars is therefore also needed. It would, however, be interesting to investigate further fully curved crownwalls on vertical breakwaters with different geometries, such as a different radius of the curve, to see if their design can be improved.

Contents

Nomenclature

Abbreviations

Abbreviation	Definition
C-CI	Confined-Crest Impact
CFD	Computational Fluid Dynamics
FEM	Finite Element Method
W5/6/7	Wave state 5, 6 and 7
FC	Fully curved
R	Recurved
DAF	Dynamic Amplification Factor

Symbols

Symbol	Definition	Unit
a	Wave amplitude	[-]
d	Water depth	[m]
f_{cm}	Compressive strength of concrete	[MPa]
f_{ctm}	Tensile strength of concrete	[MPa]
f_{cut}	Cut-off frequency	[Hz]
f_n	Eigenfrequency	[Hz]
g	Gravitational acceleration	[m/s^2]
k	Wavenumber	[rad/m]
s	Wave steepness	[%]
u_z	Vertical wave velocity	[m/s]
z_j	Vertical point of application of wave force by wave j	[m]
A_i	Area surrounding each probe i on the crownwall	[m^2]
B_r	Overhang length	[m]
E	Young's modulus	[GPa]
F_T	Total force	[kN]
F_H	Horizontal force	[kN]
F_V	Vertical force	[kN]
G_f	Fracture energy	[N/m]
H	Wave height	[m]
I_P	Pressure impulse	[Pas]
I_F	Force impulse	[kNs]
L_0	Deep water wavelength	[m]
M	Bending moment	[kNm]
P	Pressure	[Pa]
P_{Im}	Impulsive pressure	[Pa]
P_{qs+}	Maximum quasi-static pressure	[Pa]
R_c	Freeboard	[m]

Symbol	Definition	Unit
T	Wave period	[s]
T_d	Impulse duration	[s]
T_n	Natural period of the structure	[s]
U	Ursell number	[-]
α	Rayleigh mass-proportional damping coefficient	[s]
β	Rayleigh stiffness-proportional damping coefficient	[s^{-1}]
ρ	Density	[kg/m^3]
ζ	Damping ratio	[-]
ν	Poisson's ratio	[-]
σ_c	Compressive stresses	[MPa]
σ_t	Tensile stresses	[MPa]
ω	Angular frequency	[rad/s]

1

Introduction

Breakwaters are frequently needed to create safe navigation and mooring conditions inside ports and harbours. These breakwaters can either be rubble mound or composite vertical breakwaters made of concrete caissons on top of a rubble mound foundation (Takahashi, 2002). The latter type is often used to protect harbours in deep water conditions in the Mediterranean Sea, where waves are usually non-breaking (De Girolamo et al., 2019). Crownwalls can be placed on the crests of rubble mound breakwaters and on top of vertical breakwaters to reduce the breakwater's required crest height and overtopping discharges (Pedersen & Burcharth, 1993; EurOtop, 2018).

As means to reduce wave overtopping even further, crownwalls are often designed with an overhang or bullnose (i.e. rectilinear or recurved crownwall) or with a fully curved face. The seaward-facing overhang at the top of the structure confines and deflects up-rushing water from the incoming wave, significantly reducing overtopping without increasing the height of the crownwalls (EurOtop, 2018; Castellino et al., 2018a; Dermentzoglou, 2021). However, studies have shown that wave loading increases compared to a vertical crownwall. The time and space distribution of the wave pressures on the crownwall then become important, as the forces acting upwards under the overhang are impact loads with short impulse duration which may cause a significant dynamic response in stiff structures such as crownwalls (Kortenhaus et al., 2003; Kisacik et al., 2012; Castellino et al., 2018a; Chen et al., 2019). Figure 1.1 shows three examples of curved crownwalls. The figure on the top left shows a slender reinforced concrete crownwall with a curved face constructed in the harbour of Málaga, Spain, on a vertical composite breakwater (Negro et al., 2018). The other two figures show typical curved crownwalls from The United Kingdom, which are part of a seawall (Google, n.d.; Castellino et al., 2018b).

In this thesis, the focus will be on vertical breakwater crownwalls in deep water conditions. Structural failures of such crownwalls have been reported in Civitavecchia Harbour in Italy (see figure 1.3a) (Castellino et al., 2018a), on Pico Island in Azores (Martinelli et al., 2018), in Strand in South Africa (Schoonees et al., 2014) and on the island of Albrán in Spain (Valdecantos et al., 2014). Sliding and overturning are also known failure mechanisms of vertical breakwater crownwalls, as such failures have been reported in Spain (Valdecantos et al., 2014; Negro et al., 2018). There is still a lack of design standards for recurved walls (Castellino et al., 2018a) and in light of these failures, there is increased interest in understanding the structural behaviour of curved crownwalls in order to improve their design.

(a) Málaga, Spain (Negro et al., 2018). **(b)** Penhryn Bay, Wales (Google, n.d.).

(c) Scarsborough, England (Castellino et al., 2018b).

Figure 1.1: Examples of fully curved concrete crownwalls.

1.1. Literature review

Many studies have been made on wave loads on vertical seawalls and crownwalls and their dynamic response. Bagnold (1939) was one of the first to study impulsive pressures from breaking waves on a vertical seawall, which was done by laboratory tests in a flume. He showed that due to thin cushions of air in breaking waves, the shock pressures on the vertical seawall are much greater than normal hydrostatic pressures. Bagnold (1939) also found that pressure impulses are more easily predictable than the maximum pressure for breaking wave impacts, as the impulse is independent of the thickness of the air cushions. Further research on impulsive wave forces on upright breakwaters and their dynamic response was later performed by, i.e. Oumeraci et al. (1992), Oumeraci and Kortenhaus (1994), Goda (1994), Shimosako et al. (1994), Takahashi et al. (1998) and more recently Cuomo et al. (2010, 2010). They studied the dynamic response of composite breakwaters, which gave guidelines for further research and the dynamic design of these types of structures. Oumeraci and Kortenhaus (1994) highlighted the importance of dynamic analysis of vertical breakwater under impulsive wave load, showing that for an impulse duration larger than the structure's natural period, the response of the structure was amplified by dynamic effects. They also found that for impulsive loads with a duration shorter than 25% of the structure's natural period, the load shape did not affect the response but rather that the area under the load curve, the impulse, determines the response.

In 1978, Ramkema (1978) found that for the design of storm surge barrier gates with a protruding element (overhang), Bagnold's piston model (Bagnold, 1939) would be the most appropriate mathematical model to describe wave impacts by standing waves on the structure. Ramkema added to this model and took into account the compressibility of air.

Cooker and Peregrine (1990, 1995) developed a mathematical model to predict pressure impulses on a vertical breakwater due to breaking waves, *pressure-impulse theory*, based on the findings of Bagnold (1939), that pressure impulses are more constant than maximum pressure for a given wave state. Wood and Peregrine (1996) then showed that the *pressure-impulse theory* could analytically predict pressure impulses on coastal structures with overhangs. Later, Kisacik et al. (2012, 2014) used small-scale model tests to analyse the wave loading by breaking waves on a vertical structure with a horizontal overhang, with the Pier of Blankenberge (Belgium) as a reference for such a structure. Based on the *pressure-impulse theory*, they developed a prediction model for the upwards impact loads acting on the horizontal overhang. The small-scale test results showed that two individual impulsive impacts act on the structure for every incoming wave, the first on the vertical wall and the second on the corner between the vertical wall and horizontal overhang.

Chen et al. (2019) developed a new method to determine the reaction forces of hydraulic structures with an overhang subjected to impulsive wave loading, where the pressure impulse is the primary design variable. They found that the calculated pressure impulses with Cooker and Peregrine (1995) *pressure-impulse theory* agreed with the physical model test results. Pressure impulses by standing wave impacts on vertical structures with a relatively short overhang (i.e. storm surge barrier gates) at water level height have been studied by De Almeida et al. (2019) and De Almeida and Hofland (2020, 2021). Their studies showed that for a shorter overhang, the impact loads were higher and less variable with a shorter load duration. Additionally, they found that the pressure impulses over the width of the structure were less variable than the maximum pressure values. The *pressure-impulse theory* may be used for preliminary load estimations on vertical structures with short overhangs under wave loading by standing waves (De Almeida & Hofland, 2021). The *pressure-impulse theory* has further been used by Tieleman et al. (2021) to predict impulsive wave loads by standing waves on a flood gate, as they found that the response of the flood gate was in better correlation with the pressure impulses than the maximum pressure values.

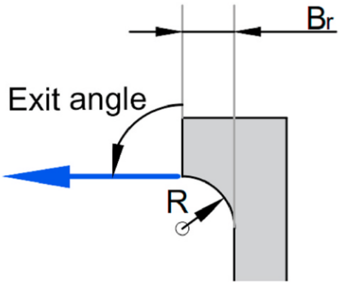

Figure 1.2: Exit angle, length of overhang B_r and radius R of a recurved crownwall (van Gent, 2021).

The effects of recurved parapets on the wave load and overtopping of vertical seawalls have also been studied. Figure 1.2 shows an example of a recurved parapet where B_r is the length of the overhang and R is the radius of the curve (van Gent, 2021). In the figure, the exit angle of the recurve is 90°. Kortenhaus et al. (2003) found that recurved parapets on vertical seawalls can reduce overtopping significantly and that wave loading, by non-impulsive waves, increases by a factor of 1.1-1.8 with an increasing exit angle (see figure 1.2) for seawalls with freeboard to wave height ratio $R_c/H_s < 1.5$. With physical model testing on a vertical wall with a seaward-facing overhang/bullnose, Pearson et al. (2005) found that the wave load was highly impulsive and that the horizontal forces were increased by a factor of 2 compared to a vertical wall. Large-scale experiments by Stagonas et al. (2014, 2020) on breaking wave impacts on a vertical seawall with a recurved parapet showed that for an increasing exit angle and overhang length, the wave load also increased. However, they found that once the exit angle was up to 90°, increasing the length of the overhang did not significantly increase loading.

1.2. Background

Castellino et al. (2018a) has studied the large impulsive forces on recurved parapets under non-breaking deep water wave conditions. Using Computational Fluid Dynamic (CFD) simulations, this numerical study compared wave pressures and forces acting on a recurved parapet to the wave pressures and forces acting on a vertical wall of the same height and in the same wave conditions. The recurved crownwall in the study replicates the crownwall in Civitavecchia Harbour, which failed during a storm (see figure 1.3a). As Figure 1.3b shows, the recurved parapet rests on a concrete caisson on a flat seabed with a constant 20 m water depth at the toe (still water level).

The results show that vertical and horizontal forces acting on the entire structure significantly increase when the top of the breakwater is shaped as a recurve and the load is impulsive. These large impact loads acting on recurved concrete crownwalls can lead to failure, as happened to the crownwall in Civitavecchia Harbour. Like Kortenhaus et al. (2003) and Stagonas et al. (2014, 2020), Castellino et al. (2018a; 2018b) also found that a larger angle of the recurve resulted in a larger load increase. It was found that the maximum force increase, compared to a vertical breakwater, occurs when the opening angle of the recurved parapet is 90° and that when the radius of the curve is increased, the forces acting on the parapet also increase. However, the effect of the increase in radius was not as much as that of the increase in exit angle. In the same way, overtopping volumes decreased with the increasing exit angle (Castellino et al., 2018a).

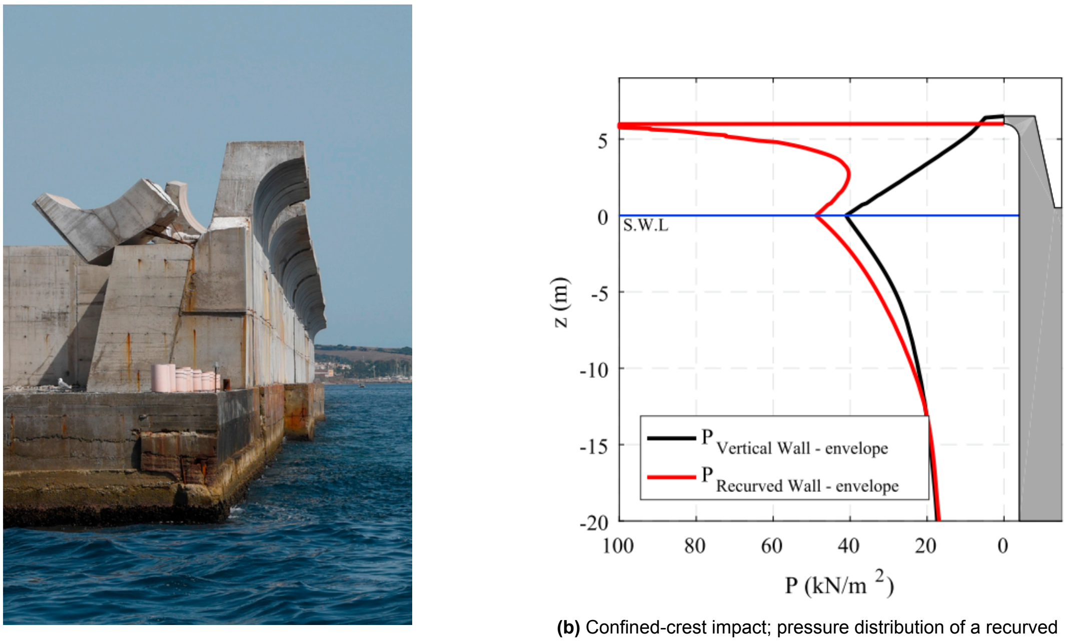

(a) Failure of recurved crownwall in Civitavecchia Harbour.

(b) Confined-crest impact; pressure distribution of a recurved crownwall compared to a vertical crownwall.

Figure 1.3: Study of Castellino et al. (2018a) on the wave loading of the recurved crownwall in Civitavecchia Harbour, which failed in a storm in 2015.

The confinement of the up-rushing water by the overhang generates large impulsive pressures, defined by Castellino et al. (2018a) as confined-crest impact (from now on referred to as C-CI). When the wave has reached the top of the crownwall and is deflected seawards by the recurve, it gains momentum, which increases both the horizontal and vertical forces acting on the breakwater. The confinement of the wave creates the impulsive nature of the force, as at the moment the wave is deflected seawards, at a high-speed flow, the incoming wave crest stops the return flow (Castellino et al., 2018a). The C-CI phenomenon affects the whole breakwater, not only the recurved top part, as shown in figure 1.3b, as pressure increases all along the height of the crownwall and down to $z = -10m$. The impulsive pressure at the top of the recurved parapet can be up to ten times larger than the pressure inflicted on a purely vertical wall (Castellino et al., 2018a). The existence of the C-CI phenomenon has been confirmed by Martinelli et al. (2018) with physical model testing of the same recurved shape of a crownwall for both regular and irregular waves. The results of the physical model tests showed very similar force values and impact shapes to those of the numerical model for the same wave states. The influence of the exit angle could also be seen with the physical model tests, where increasing the exit angle lead to an increase in wave load (Martinelli et al., 2018). For calculations of static wave loading, the method of Goda (1974) is most widely used, as well as the extended Goda method by Takahashi (2002). However, Martinelli et al. (2018) found that the total force calculated with Goda's formulae greatly underestimated the measured total forces on the recurve crownwall. Castellino et al. (2021) proposed a method to extend the Goda's formulae for vertical breakwaters such that it could be valid for recurved crownwalls.

Dermentzoglou (2021) investigated which equations could be used to predict overtopping and loading from non-breaking waves on a fully curved crownwall. For waves with $\frac{U}{R_c/H} < 14.9$, where U is Ursell's number, R_c the freeboard of the crownwall and H the wave height, he found that the Goda's formulae could be used to predict the wave load. However, for waves with $\frac{U}{R_c/H} > 14.9$, wave impacts occurred, and Goda's formulae underestimated the wave load. Dermentzoglou (2021) also found that pressure impulses were more predictable than maximum pressures, further supporting the use of the *pressure-impulse theory* to predict wave loading on structures subjected to wave impacts.

To better understand the dynamic response of recurved parapet crownwalls to C-CI loading, Dermentzoglou et al. (2021) carried out a Finite Element analysis of the same crownwall as investigated by Castellino et al. (2018a) and Martinelli et al. (2018). Offline one-way coupling of the CFD pressure time series by Castellino et al. (2018a) and a time-varying Finite Element analysis was used in the study. Three different concrete classes (C25/30, C30/37 and C35/45) were tested to investigate the effects of material properties on the structural behaviour and to try to determine what caused the failure of the Civitavecchia crownwall. At the time of the failure of the crownwall, it was estimated that the maximum wave, causing the failure, had a wave height of 5 m and a wave period of 8 s. The FEM analysis results of Dermentzoglou et al. (2021) did however not show a failure of the recurved crownwall for a wave state with those wave characteristics, suggesting that the crownwall might be built of concrete with a strength class lower than C25/30. For a wave state with a wave height of 7 m and wave period of 11 s, small cracks of 0.22 mm in width formed in the front face of the crownwall, with concrete strength class C25/30, and propagated halfway through the cross-section (Dermentzoglou et al., 2021).

1.3. Aims and objectives

Fully curved crownwalls are frequently used in seawalls, see figures 1.1b-1.1c, where they are subjected to broken waves. However, there are gaps in the knowledge of the loading and structural behaviour of fully curved concrete crownwalls on vertical breakwaters subjected to non-breaking waves. The design of the shape of the fully curved crownwall comes from *Sapienza University of Rome*, see figure 1.4, and is the same shape as studied by Dermentzoglou (2021). He showed, with physical model tests, that wave impacts occur for regular waves with steepness $s = 3 - 4\%$. This study aims to further increase the knowledge on the wave loading and dynamic response of concrete crownwalls with a fully curved face under wave loading by non-breaking waves. The following research question and sub-questions have been formed:

What is the 2D dynamic response of a crownwall with a fully curved face to impulsive wave loading by non-breaking waves?

- How does the wave loading and dynamic response of a fully curved crownwall compare to that of a recurved crownwall?
- How does is effect the structural response of the crownwall to add a supporting wall behind it?
- How accurately does the extended Goda method for C-CI wave load by Castellino et al. (2021) estimate the wave load on the fully curved crownwall?
- How can this knowledge be used to give design recommendations regarding the geometry of curved crownwalls?

This study is connected to the 2D FEM analysis of Dermentzoglou et al. (2021) on a recurved crownwall. Numerically generated pressure-time series of the same wave states as used by Dermentzoglou et al. (2021), will first be analysed to determine the loading of the structure. By analysing the pressure distribution along the height of the two different shapes of crownwall, important insight can be gained into the shapes' effects on the structures' loading. As Dermentzoglou et al. (2021) has shown, the wave load may be impulsive for some wave states and it is important for the structural analysis to evaluate the impulse duration, T_d, compared to the natural period of the structure T_n. Through offline one-way coupling, the pressure-time series will be applied to a FEM model in Diana FEA 10.5 and a dynamic structural analysis will be performed. The results of the structural analysis will be compared to the results of Dermentzoglou (2021) to estimate the structural performance of the fully curved crownwall compared to the recurved crownwall. To estimate the applicability of the extension by Castellino et al.

(2021) to the Goda method to account for the C-CI phenomenon, the static load on the fully curved crownwall will be calculated and compared to the maximum pressure distribution of the numerically generated pressure-time series. Structural static analysis will also be performed for the calculated static wave load and the resulting displacements and stresses compared to those of the dynamic linear analysis.

1.4. Scope and structure of report

The structural analysis will be performed in 2D for normally incident regular waves. Therefore, three-dimensional effects, such as oblique waves and the finite length of the crownwall, are excluded. The three wave states have wave steepness $s = 3.7 - 6\%$ and dimensionless freeboard $R_c/H = 0.92 - 1.30$. As shown in figure 1.3b, the seabed is assumed to be flat.

The only failure mechanism studied is a structural failure of the crownwall, i.e. cracking. Sliding or overturning will not be accounted for in the FEM model. Due to the one-way coupling of the numerically generated wave load and the FEM model, the deflection of the structure is not accounted for in the wave load. That means that the wave load might be slightly overestimated at the top of the crownwall, where deflection is assumed to be the largest. To be consistent with the FEM model of Dermentzoglou et al. (2021), no reinforcement bars will be included in the FEM model.

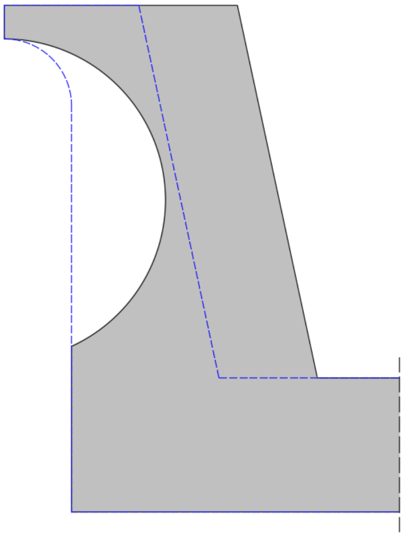

Figure 1.4: Fully curved crownwall (gray shape) compared to recurved crownwall (blue dashed line).

The structure of the report is as follows. In chapter 2, the numerical model used to generate the wave load is introduced, and wave characteristics and the method used to analyse the pressure and force impacts are described. Chapter 2 also includes a description of the FEM model in Diana FEA, a mesh sensitivity analysis, modal analysis, Rayleigh damping coefficients and a description of the chosen nonlinear model. In chapter 3, the results of the analysis of the wave load and the static and dynamic structural analyses are presented. In chapter 4, a comparison is made between the recurved and fully curved crownwalls. The differences in wave loading and structural response are discussed. Chapter 5 discusses the results of the structural analysis of the fully curved crownwall, the stability of the crownwall and how the geometry of the curve has effects on the loading. Finally, in chapter 6, the conclusions of the thesis are presented, the research questions are answered, and design recommendations are given.

2

Methods

In this chapter, the wave load and FEM model will be introduced. In order to be able to compare the fully curved crownwall to the recurved crownwall, the wave states used in this thesis are the same as the ones used by Castellino et al. (2018a) and Dermentzoglou et al. (2021) in their analyses of the wave load and structural response of the recurved crownwall. The crest freeboard and the overhang length of the fully curved and recurved crownwalls are also the same, $R_c = 6.5m$ and $B_r = 1m$ respectively. The same FEM modelling software, Diana FEA 10.5, as was used by Dermentzoglou et al. (2021) is also used in this study, with the same material properties and the same boundary conditions.

2.1. Wave load

2.1.1. Wave characteristics and pressure time series

The 2D pressure time series were obtained from numerical simulations in the IHFOAM solver (Higuera et al., 2014) which is based on OpenFOAM® (Higuera et al., 2013a, 2013b) and includes the incompressible 3D Reynolds-averaged Navier-Stokes (RANS) conservation equations (Castellino et al., 2018a). Some basic assumptions that were made regarding the numerical simulation are that the seabed and the structure are impermeable and water and air are incompressible. The numerical model set-up is further described in Castellino et al. (2018a).

Table 2.1 shows the three wave states that are used in the analysis and their corresponding wave height (H), wave period (T), deep water wave length (L_0), wave steepness ($s = H/L_0$), relative freeboard (R_c/H), wave height over water depth (H/d) and the Ursell number (U). These are non-breaking regular waves. The water depth (d) in front of the crownwall is $20\ m$ and the seabed is assumed flat. These variables are visualized in figure 2.1. The deep water depth and non-breaking wave conditions are typical for vertical breakwaters on the Mediterranean coast, e.g. in the harbour of Civitavecchia, Italy (Castellino et al., 2018a).

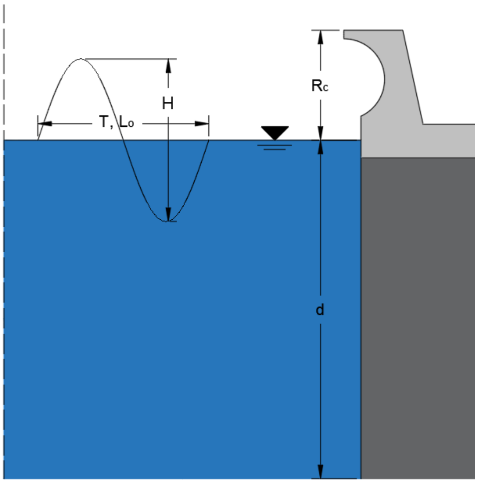

Figure 2.1: Wave characteristics: H is wave height, T is wave period and L_0 is the deep water wave length. R_c is the freeboard and d is the water depth at the toe of the breakwater.

Table 2.1: Wave characteristics of numerically simulated wave conditions.

Wave state [-]	H [m]	T [s]	L_0 [m]	s [%]	R_c/H [-]	H/d [-]	U [-]
W5	5	8	100	5	1.30	0.25	4.9
W6	6	8	100	6	1.08	0.3	5.9
W7	7	11	189	3.7	0.92	0.35	16.4

A total of 131 measuring points (probes) are located all along the front face of the caisson and crownwall that measure pressure over a time of 100 s. On the vertical part of the wall, the distance between the probes varies from 0.25 m to 0.1 m (the probes are closer together near the curve), while on the curved part, there is a probe at every 5°. As only the crownwall is modelled in the FEM model, only the top 56 probes are considered and re-numbered such that probe one is located at the bottom of the crownwall and probe 56 at the top, see Figure 2.2. To reduce computational time, only the first 80-85 s of the pressure time series are applied to the FEM model, as the last two waves in all three wave states are relatively smaller than the first 6-8 waves and purely quasi-static. Figure 2.2 shows the pressure time series from wave state 7 for three different measuring points on the face of the crownwall. It can be seen how the maximum instantaneous pressure values increase higher up in the curve and how the impact profiles take the well-known shape of a church roof, with an initial maximum impact pressure P_{Im} followed by a slowly varying quasi-static pressure with a second peak P_{qs+} (see also figure 2.4).

Figures 2.3 show the time series of the total force acting on the crownwall. The total force, F_T, is simply the integral of the pressure along the height of the wall at each moment in time. It can be seen that for wave states 5 and 6, where the waves have a period of $T = 8s$ there are eight waves in the first 80 seconds of the time series, while for wave state 7, where the waves are longer and have a period of $T = 11s$, there are a total of 6 waves. The wave load will be further analysed and discussed in chapter 3.1.

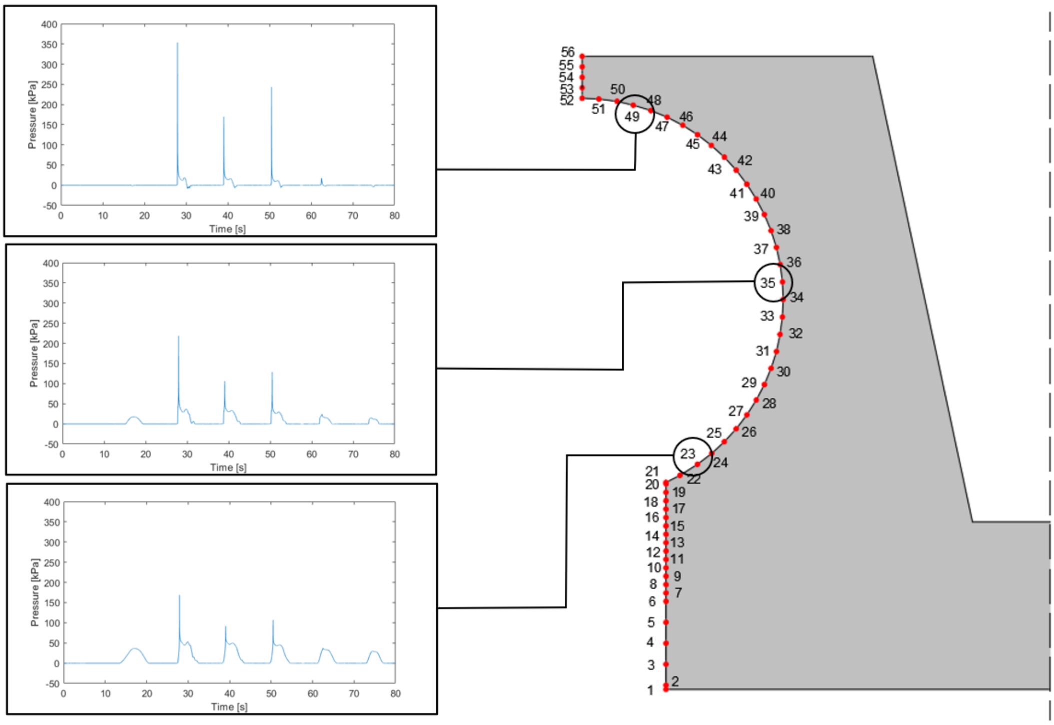

Figure 2.2: Pressure time series at different measuring points on the fully curved crownwall for W7.

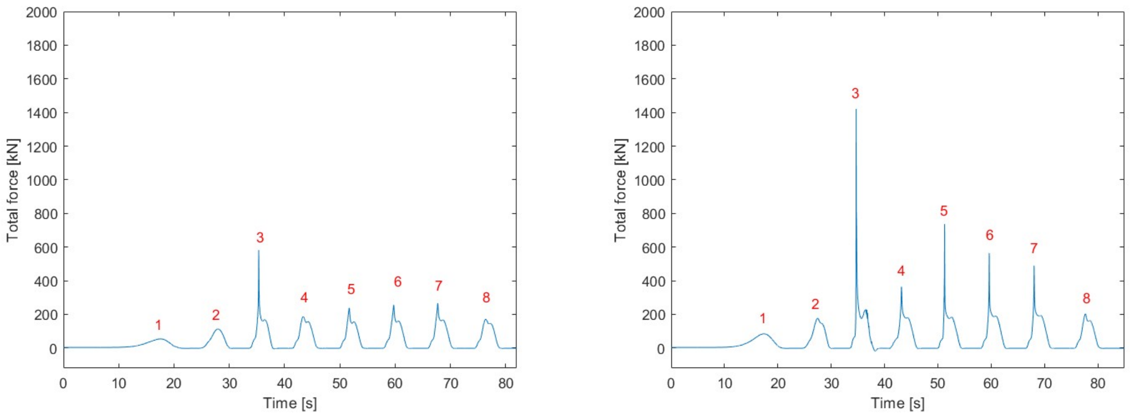

(a) F_T of W5 ($H = 5m$, $T = 8s$).

(b) F_T of W6 ($H = 6m$, $T = 8s$).

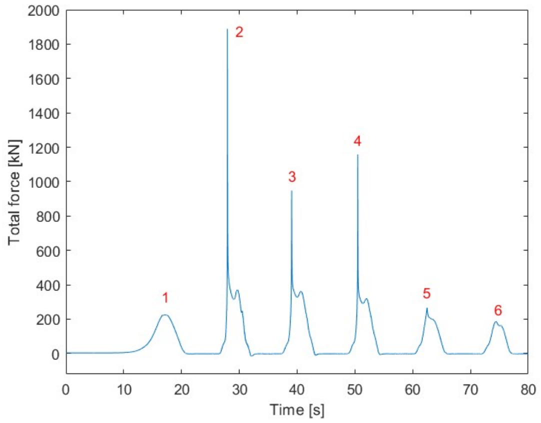

(c) F_T of W7 ($H = 7m$, $T = 11s$).

Figure 2.3: Total time series of the total force of the three wave states.

2.1.2. Pressure impacts and loading domain

Kortenhaus and Oumeraci (1999) developed a method to identify different types of wave impacts from a force time series. According to this method, an impact can be defined as impulsive if the maximum horizontal force is larger than 2.5 times the maximum quasi-static horizontal force:

$$F_{H,max}/F_{H,qs+} > 2.5.$$

Streicher et al. (2019) later added to this method a definition of a dynamic impact, where the ratio between the two force values is in the range of 1.2-2.5. This method can also identify the type of pressure impacts based on a pressure time series (Huang et al., 2022). Table 2.2 shows the definition of the pressure impact types and figure 2.4 shows the pressure time series of the three largest wave impacts at measuring points 23, 33 and 49 for W7. This method is used to identify the pressure impact type along the height of the crownwall for all three wave states.

Table 2.2: Definition of pressure impact types (Huang et al., 2022).

Pressure impact types	P_{Im}/P_{qs+}
Quasi-static	< 1.2
Dynamic	$1.2 - 2.5$
Impulsive	> 2.5

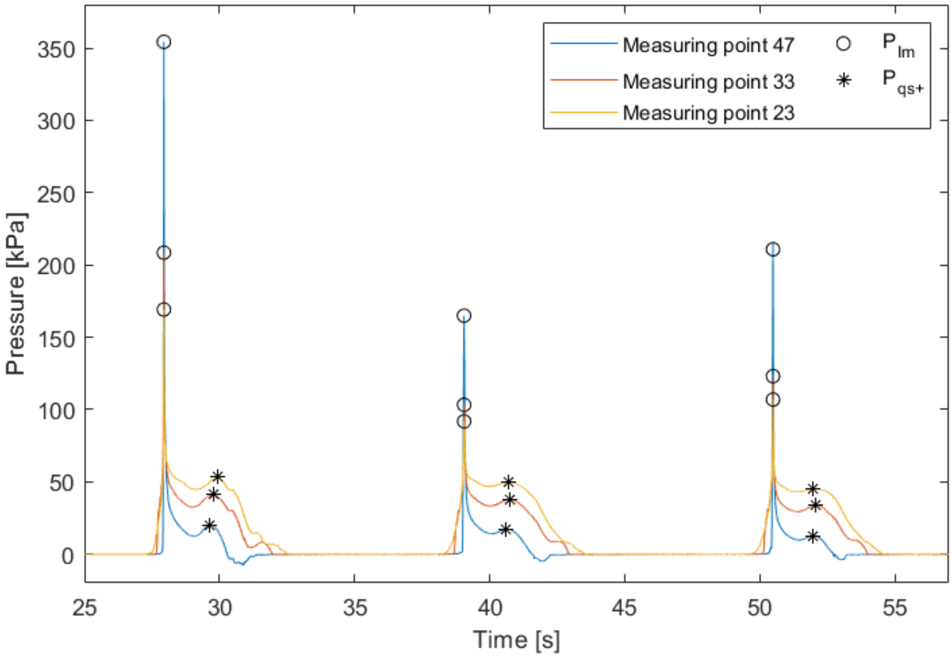

Figure 2.4: Pressure time series at measuring points 23, 33 and 47 for W7 ($H = 7m, T = 11s$).

The impulse, I_P, and impulse duration, T_d, can now be determined for the pressure impacts that are defined as dynamic or impulsive by table 2.2. First, a beginning and end point of the impulse in time need to be determined (t_a and t_b respectively) and the impulse is then taken as the integral of the pressure-time series between those two points (Cooker & Peregrine, 1995):

$$I_P = \int_{t_a}^{t_b} P(t)\,dt \tag{2.1}$$

Various different methods have been introduced to determine impulse duration of force and pressure impacts (Cooker & Peregrine, 1990; Oumeraci & Kortenhaus, 1994; Wood et al., 2000; Cuomo et al., 2010). Using a low-pass filter with a specific cut-off frequency, f_{cut}, to separate the high-frequency impulsive load from the low-frequency quasi-static load has become a widely used method (Chen et al., 2019; De Almeida & Hofland, 2020; Huang & Chen, 2020). The cut-off frequency can be determined by using a continuous 1D wavelet transform (CWT) (Chen et al., 2019; Huang & Chen, 2020) or as a function of the frequency of the incident waves (De Almeida & Hofland, 2020). Dermentzoglou (2021) has also shown that a smoothing function can be used to separate the impulse from the quasi-static load.

As mentioned by De Almeida and Hofland (2020), due to significant variations in pressure impact profiles, there is no single method to determine the pressure impulse. To address this, they developed a method based on various pressure impact profiles obtained by physical model tests of wave loading on a vertical wall with an overhang that can be used consistently to define pressure impulses. After the quasi-static and impulsive parts of the load have been split using a low-pass third-order Butterworth filter, the beginning of the impulse is defined as the point where the pressure becomes larger than 20% of the maximum quasi-static pressure (P_{qs+}) and the end of the impulse is defined as the point where the difference between the original pressure-time series and the filtered quasi-static pressure-time series becomes less than 20% of P_{qs+} (De Almeida & Hofland, 2020). The cut-off frequency for the low-pass third-order Butterworth filter, used by De Almeida and Hofland (2020), is set equal to two times the frequency of the incident wave.

Figure 2.5 shows the energy spectrum of the pressure-time series of W7 at probe 51 at the top of the curve of the crownwall. The incident wave frequency for this wave state is $f_{W7} = 0.09 Hz$. The red line in figure 2.5 represents the second harmonic of the incident wave, or the frequency equal to two times f_{W7}. As the figure shows, there is still quite some energy in higher harmonics and therefore, cut-off frequencies equal to five (blue line), ten (green line) and twenty (orange line) times f_W are also tested for all three wave states.

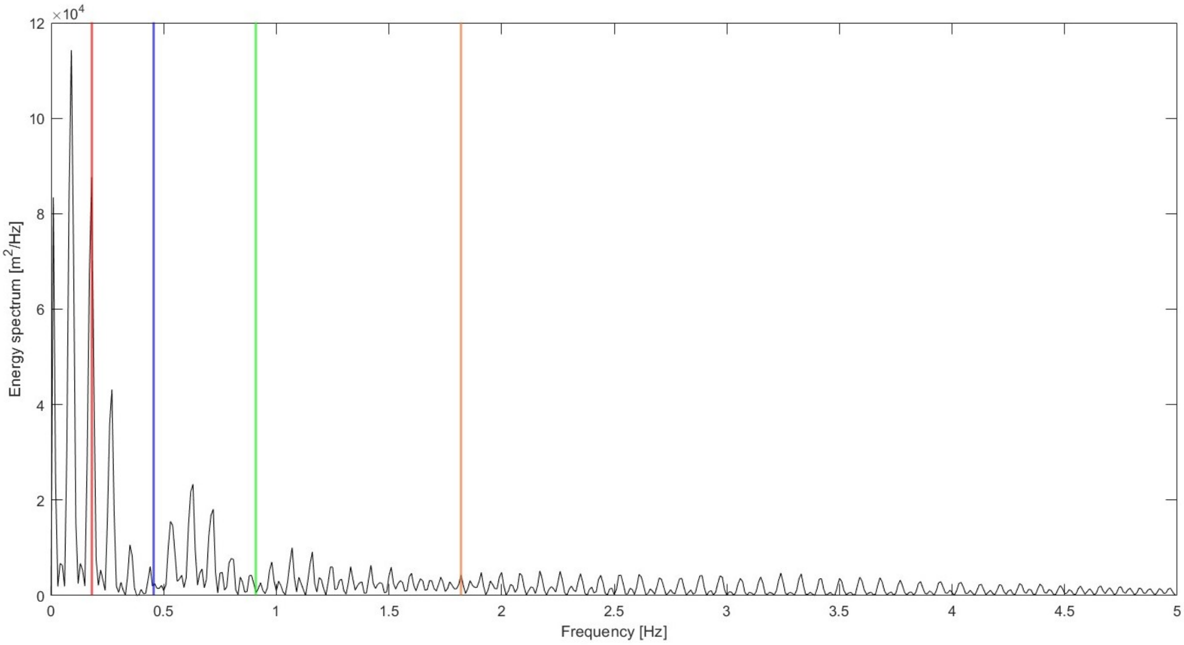

Figure 2.5: Energy spectrum of the pressure-time series of W7 ($H = 7m$, $T = 11s$) at probe 51. The red, blue, green and orange lines represent frequencies equal to two, five, ten and twenty times the frequency of the incident wave, respectively.

Figure 2.6 shows the results of the low-pass filtering with the different cut-off frequencies. For $f_{cut} = 2f_{W7}$ and $f_{cut} = 5f_{W7}$ (red and blue lines respectively), the filtered pressure series do not follow the quasi-static part of the original series very well. For the larger cut-off frequencies (green and orange lines), the filtered series follow the quasi-static part of the original pressure series well, but a second peak is formed at the location of the impulse. This is not coherent with the method of De Almeida and Hofland (2020), so low-pass filtering can not be used in this analysis to separate the impulsive and quasi-static parts of the load. The impulse durations will instead be determined by hand, using the first derivative of the pressure-time series to help determine the beginning and end points, t_a and t_b.

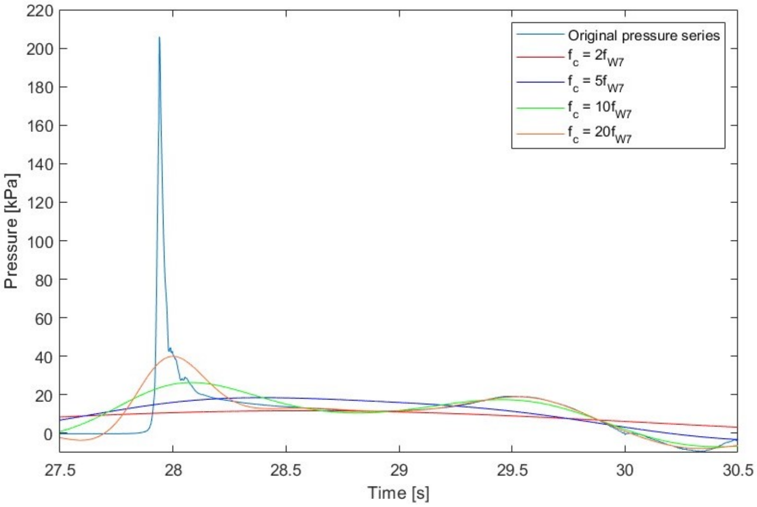

Figure 2.6: Original pressure-time series of the maximum pressure impact of W7 at probe 51. Filtered pressure-time series with different cut-off frequencies: $f_{cut} = 2f_{W7}$ in red, $f_{cut} = 5f_{W7}$ in blue, $f_{cut} = 10f_{W7}$ in green and $f_{cut} = 20f_{W7}$ in orange

Figure 2.7 shows how the derivative method is used for four different probes on the crownwall and the pressure-times series of the largest wave in W7. For the upper part of the curve, see probe 51 in figure 2.7a, the increase in pressure is sharp and the beginning of the impulse, t_a, is taken as the point where the pressure rises above zero. For probes lower on the wall, the rise in pressure is not as sharp and the first derivative is used to determine where the slope of the pressure-time series starts to increase and that indicates the beginning point of the impulse (see 2.7d-2.7h). Similarly, for the endpoint t_b, the first derivative is used to determine where the slope decreases. A line is then drawn between t_a and t_b and the impulse, I_P, is equal to the integral of the pressure-time series above that line. This method is not as consistent as the method of De Almeida and Hofland (2020) and there is always some uncertainty when choosing the beginning and end points by hand, but using the first derivative of the pressure-time series offers a vital guideline and reduces uncertainty. As this method is quite time-consuming, only the time series of the pressure at probes 9, 23, 28, 33, 37, 42, 47 and 51 are analysed. These probes should give a good idea of the loading conditions along the wall.

The next step is to consider the structure's natural period and determine the loading domain of the wave load. By looking at the ratio between the pressure impulse duration, T_d, and the natural period of the structure, T_n, the impulses can be divided into three loading domains: quasi-static, dynamic and impulsive (Humar (2002), cited by Chen et al. (2019)). Table 2.3 shows how each domain is defined by the ratio between T_d and T_n. Determining the loading domain is an important step, as the type of structural analysis is heavily dependent on it. If the wave load is in the dynamic domain of the crownwall, a time history analysis of the dynamic response of the structure is needed, while for a wave load in the quasi-static domain, a simple static analysis is sufficient (Chen et al., 2019).

Table 2.3: Loading domains (Chen et al., 2019).

Loading domain	T_d/T_n
Quasi-static	≥ 4
Dynamic	$0.25 - 4$
Impulsive	< 0.25

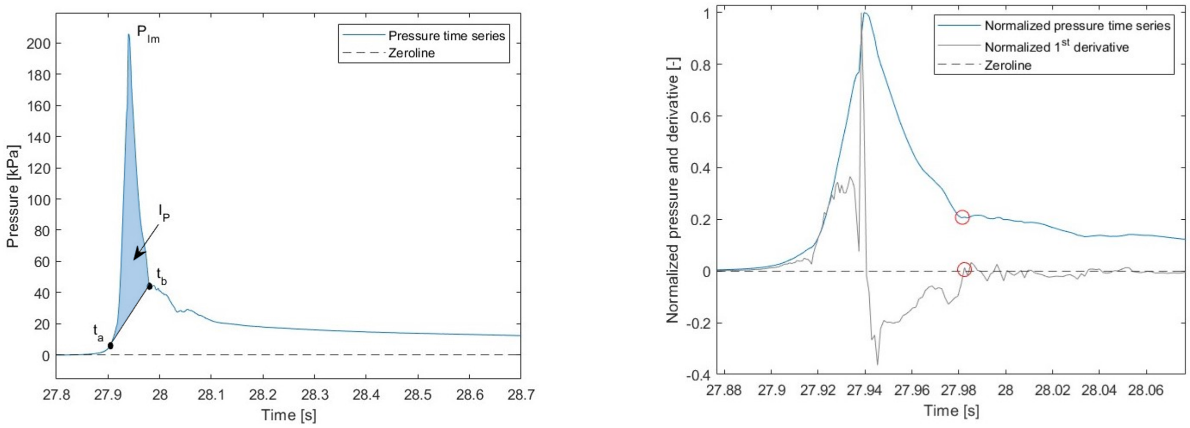

(a) Pressure impulse at probe 51.

(b) Norm. pressure impulse and the 1st derivative at probe 51.

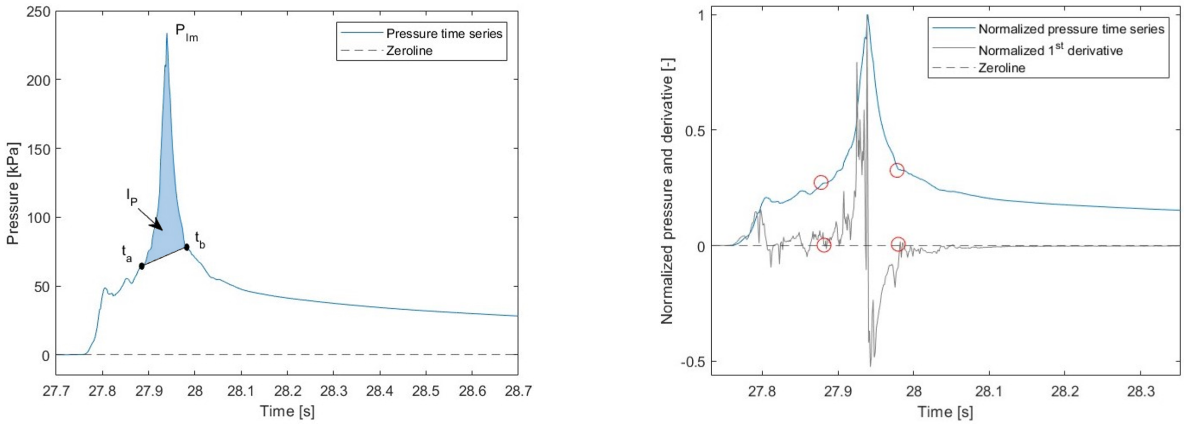

(c) Pressure impulse at probe 37.

(d) Norm. pressure impulse and the 1st derivative at probe 37.

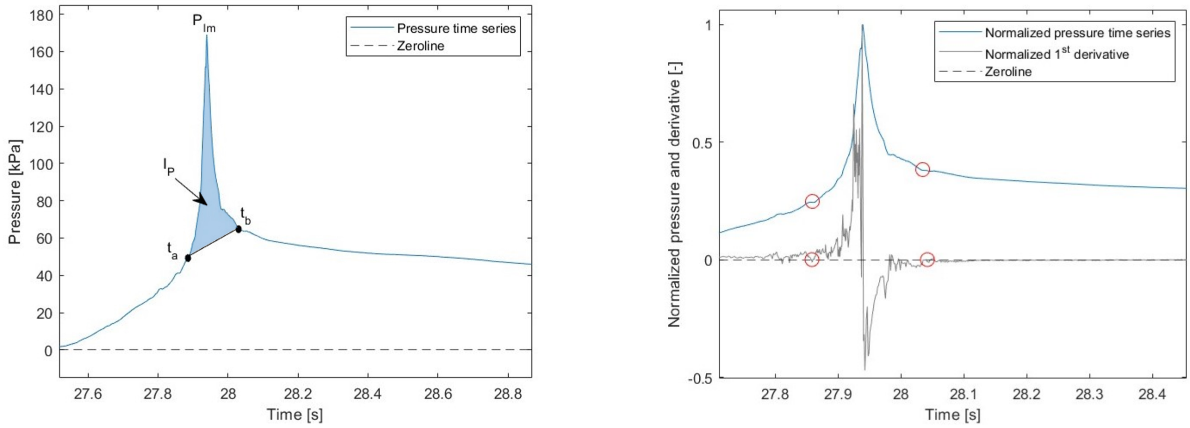

(e) Pressure impulse at probe 23.

(f) Norm. pressure impulse and the 1st derivative at probe 23.

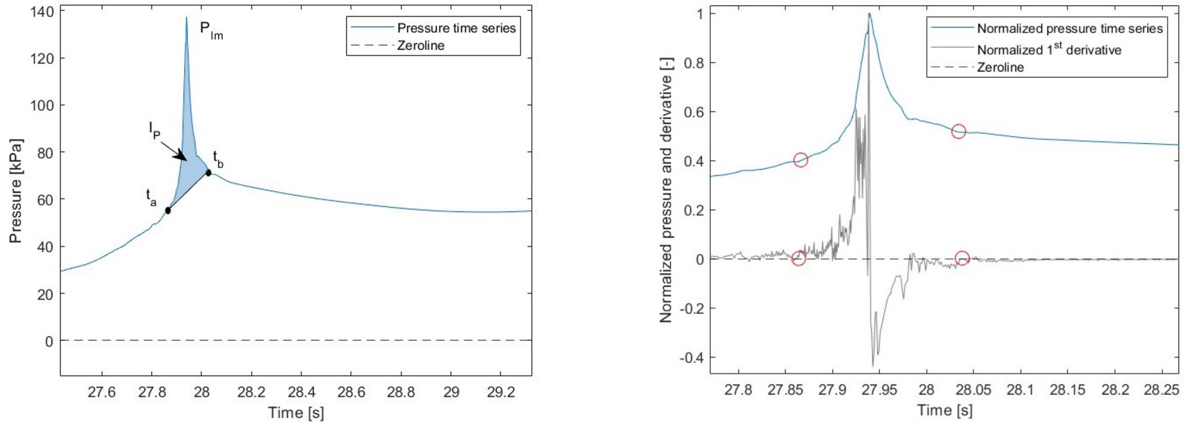

(g) Pressure impulse at probe 9.

(h) Norm. pressure impulse and the 1st derivative at probe 9.

Figure 2.7: To the left: pressure time series for the largest wave in W7, showing the beginning and end points of the impulse (t_a and t_b) and the impulse (I_P) is the area above the black line. To the right: the pressure normalized with the maximum pressure (P_{Im}), the first derivative of the pressure normalized with the maximum derivative and the red circles indicate how the derivative is used to help determine the beginning and end points of the impulse.

2.2. Finite element model

2.2.1. 2D Model set-up and assumptions

The crownwall is modelled in 2D in the XY plane with plane-strain elements, meaning that the out-of-plane strain components are zero and there will be no out-of-plane deformation. This model type is suitable for modelling infinitely long structures (DIANA FEA BV, 2021), an assumption made for the crownwall in the 2D analysis. The model thickness is $1\ m$ and the mesh type is quadrangle/hexahedron with a quadratic mesh order.

Figure 2.8 shows the dimensions and boundary conditions of the fully curved crownwall. Like the crownwall in Civitavecchia, it is assumed that the fully curved crownwall is constructed on top of a precast concrete caisson. In practice, the precast concrete caissons are transported to the location of the seawall, where the crownwall is either cast in situ on top of the caissons or precast and placed on top. Therefore, the crownwall is not rigidly connected to the caissons and can slide under large horizontal loading. For simplicity, in this analysis, the connection between the crownwall and the caisson is modelled as a fully rigid connection and the crownwall is not allowed to slide. This assumption might lead to slightly larger stresses in the concrete than can be expected in reality because if the wall slides, some of the energy of the wave load acting on the crownwall will be dissipated by the sliding motion and therefore, less energy goes into deflecting the vertical part of the crownwall.

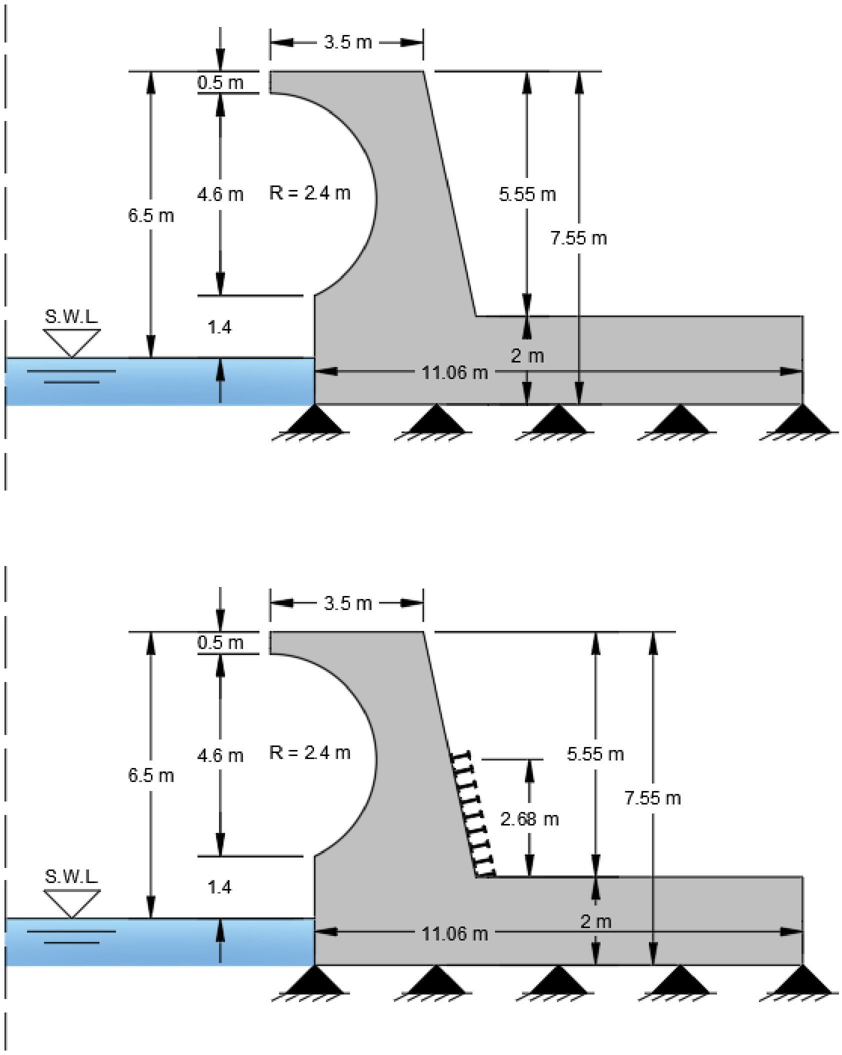

Figure 2.8: Rigidly supported fully curved crownwall with a freeboard height of $6.5\ m$. Two models are made of the wall with different boundary conditions: with a stiff boundary interface representing an additional supporting wall, *supported* (lower); and without a stiff boundary interface, *unsupported* (upper)

In Civitavecchia harbour, an additional concrete wall was constructed behind the crownwall (Dermentzoglou et al., 2021). Dermentzoglou et al. (2021) modelled this additional wall as a boundary interface with high stiffness. In this analysis, the fully curved crownwall is modelled with two different boundary conditions, as shown in Figure 2.8, with and without this stiff boundary interface. The two models will be referred to as the ***supported*** and ***unsupported*** crownwall, respectively. In this way, the analysis results of the *supported* crownwall can be directly compared to the results of Dermentzoglou et al. (2021) as the same boundary conditions are used. The effect of the additional wall can then be estimated by comparing the results of the analyses of the *unsupported* and *supported* walls. The boundary interface has a normal stiffness of $1 \cdot 10^{12}\ N/m^3$ and a shear stiffness of $1 \cdot 10^{6}\ N/m^3$.

No reinforcement bars will be included in the analysis of the crownwall. In that way, high tensile stress areas can be identified from the linear analysis and the number of reinforcement bars needed can be estimated. If the linear analysis results show tensile stresses that are larger than the tensile strength of the concrete, a nonlinear analysis will be performed to determine crack formation. According to Eurocode 2 (EN 1992-1-1, 2004), the crownwall is in exposure class XS3 (tidal, splash and spray zones) and should therefore be constructed from concrete in strength class C35/45. The Young's modulus for this strength class is $E = 34\ GPa$ (EN1992-1-1, 2004), the mass density of concrete is taken as $\rho = 2400\ kg/m^3$ and the Poisson's ratio as $\nu = 0.2$.

2.2.2. Mesh sensitivity analysis

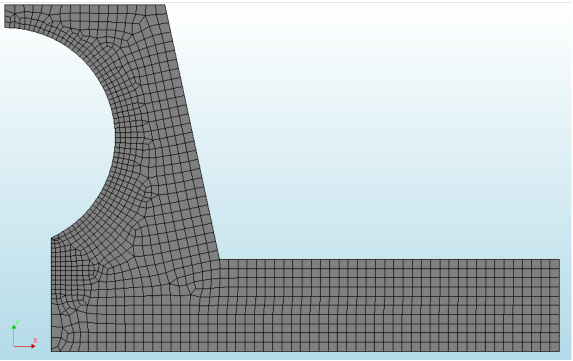

Figure 2.9: Meshing of the crownwall in Diana FEA with mesh size 0.2 m. Mesh refinement in the curve of the crownwall where cracks are expected.

A structural eigenvalue analysis is performed to determine the first five eigenfrequencies of the structure for varying mesh sizes. The change in eigenfrequencies with mesh refinement is then used to determine the structure's sensitivity to the mesh size. This is done only for the unsupported wall and the same mesh size is used for the supported wall. Figure 2.10 shows the results of the mesh sensitivity analysis. The figure shows on the right y-axis in blue, the eigenfrequencies normalized with the eigenfrequency for a 1 m mesh for each eigenmode. It can be seen that there are relatively small changes in the eigenfrequencies when the mesh size is reduced, as for the smallest mesh size of 0.05 m, the eigenfrequencies are 96-98% of the eigenfrequency for a mesh size of 1 m, depending on the mode. Figure 2.10 also shows, on the left y-axis in black, the number of elements for each mesh size. The element count increases exponentially with decreased element size, which also increases the computational time of the analysis. A mesh size of 0.2 m is chosen for the model with regard to the convergence of the eigenfrequencies and the number of elements.

Figure 2.9 shows the meshed FE model. On the curved front face of the crownwall, nodes are located according to the measuring points in the CFD model, such that the pressure time series can be applied correctly to the FE model. Additional nodes are added in the curve of the wall to have a finer mesh where cracks are expected.

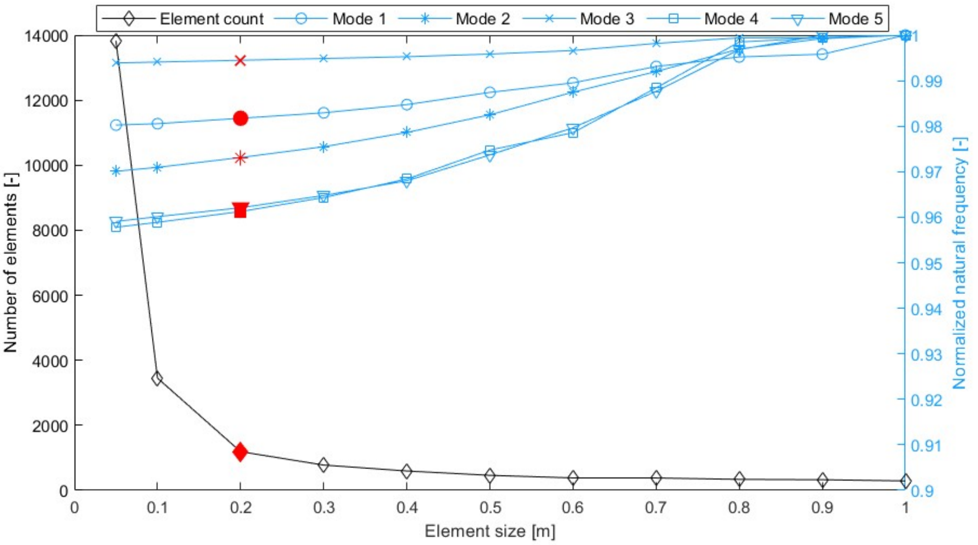

Figure 2.10: Results of mesh sensitivity analysis. A mesh size of 0.2 m is chosen, shown in red markers, with regard to the convergence of the eigenfrequencies and the number of elements.

2.2.3. Modal analysis and effective mass

Figures 2.11 and 2.12 show the results of the structural eigenvalue analysis for the chosen mesh size of 0.2 m. There is a resemblance between the modal shapes of the two crownwalls but the unsupported crownwall has lower eigenfrequencies than the supported crownwall, which is the result of the lower stiffness of that crownwall. For similar eigenfrequencies, the crownwalls have similar modal shapes as expected, where eigenmodes 1, 2, 4, 5 and 6 of the unsupported crownwall resemble eigenmodes 1 to 5 of the supported crownwall. In modes 1-5 of the unsupported crownwall and modes 1-4 of the supported crownwall the vertical part of the crownwall is activated while in modes 5 and 6, respectively, the back of the slab of the crownwall is also activated. It can be seen that the modal shape of eigenmode 3 of the unsupported crownwall (see figure 2.11c) does not exist when the wall is supported.

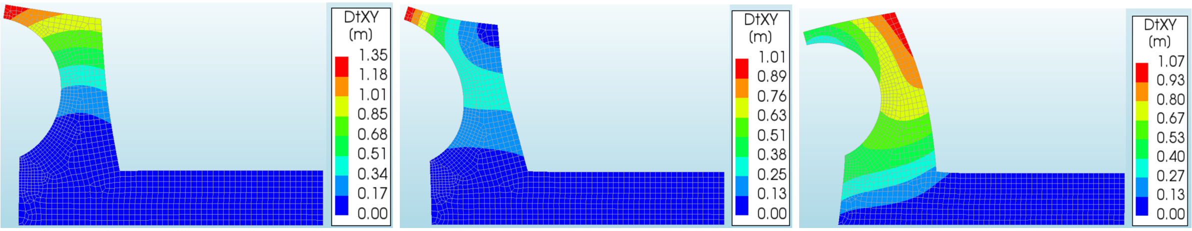

(a) Mode 1 - 32.8 Hz **(b)** Mode 2 - 89.1 Hz **(c)** Mode 3 - 153.2 Hz

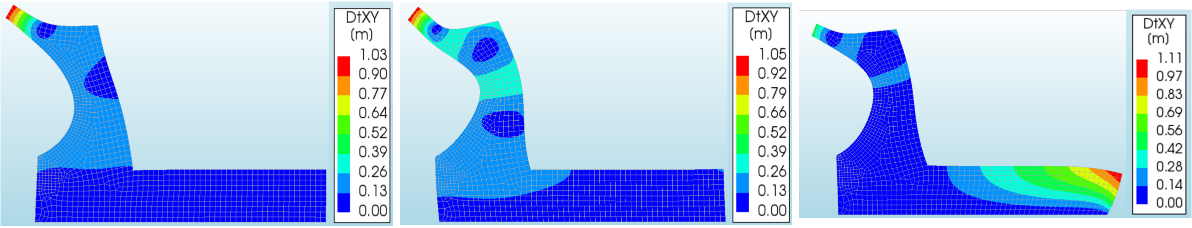

(d) Mode 4 - 178.0 Hz **(e)** Mode 5 - 263.5 Hz **(f)** Mode 6 - 299.2 Hz

Figure 2.11: The first six eigenmodes of the unsupported crownwall.

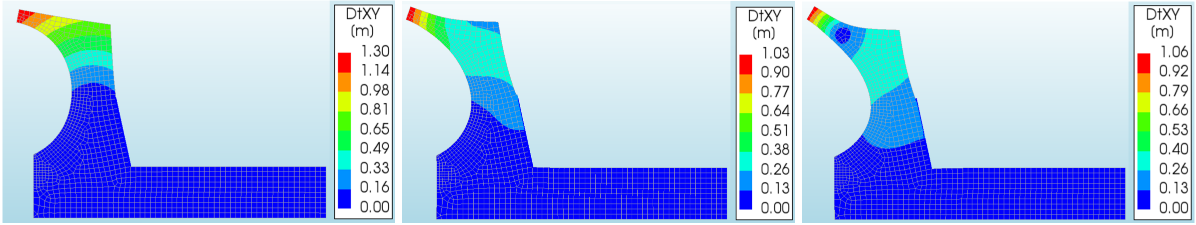

(a) Mode 1 - 42.6 Hz **(b)** Mode 2 - 118.5 Hz **(c)** Mode 3 - 166.5 Hz

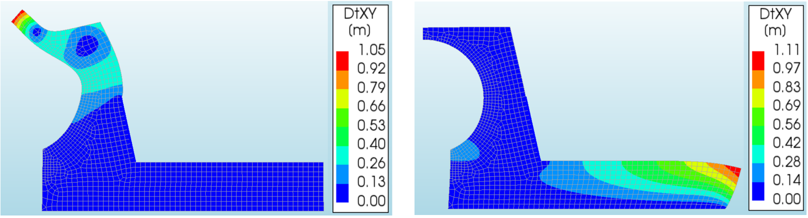

(d) Mode 4 - 284.8 Hz **(e)** Mode 5 - 296.3 Hz

Figure 2.12: The first five eigenmodes of the supported crownwall.

Table 2.4 shows the effective modal mass in the X-direction of each eigenmode, the percentage of the effective mass of the total mass of the structure and the cumulative percentage of the effective mass after each mode. The effective mass is a good indicator of the importance of each mode to the dynamic response of the structure. For both crownwalls, the first eigenmode is the dominant mode for the vertical part of the wall, as for the unsupported crownwall, mode 1 has the largest effective mass and for the supported crownwall, the only mode with a larger effective mass is mode 5 which only shows deformation of the slab. It can be assumed that the wave load, exerted on the crownwalls in this analysis, will have limited to no effect on the slab of the crownwall. It is more interesting to see that for the first eigenmodes, where the vertical part is activated, the mass percentage of the effective mass of each mode is larger for the unsupported crownwall. So, the supported crownwall is stiffer than the unsupported crownwall and there is less energy contained in each eigenmode involving the vertical part but more energy in the eigenmode that involves the back of the slab.

Table 2.4: Effective modal mass in the X-direction of the first five to six eigenmodes of the two crownwalls.

Crownwall	Eigenfrequency [Hz]	Effective mass [kg]	Mass percentage [%]	Cumulative mass percentage [%]
Unsupported	32.8	15647	18.4	18.4
	89.1	11944	14.1	32.5
	153.2	4716.4	5.6	38.1
	178.0	7997.7	9.4	47.5
	263.5	13242	15.6	63.1
	299.2	14635	17.2	80.3
Supported	42.6	8727.6	10.3	10.3
	118.5	5178.9	6.1	16.4
	166.5	308.8	0.4	16.8
	284.8	2383.2	2.8	19.6
	296.3	32538	38.3	57.9

2.2.4. Rayleigh damping

For the dynamic analysis, damping needs to be assigned to the models. Rayleigh damping is adopted to determine the damping matrix of the structure ($\bar{C}$), which is calculated as being linearly proportional to the mass ($\bar{M}$) and stiffness ($\bar{K}$) matrices:

$$\bar{C} = \alpha\bar{M} + \beta\bar{K}.$$

Here, α and β are Rayleigh damping coefficients. The damping ratio, ζ_n, is dependent on these two coefficients and the n-th eigenfrequency, f_n (Paultre, 2013):

$$\zeta_n = \frac{\alpha}{4\pi f_n} + \beta\pi f_n.$$

Table 2.5 shows the frequencies and damping ratios used for the calculation and the resulting damping coefficients for both crownwalls, unsupported and supported. The frequency f_1 is chosen as a frequency slightly lower than the first eigenfrequency of the structure and f_2 is chosen as the frequency where the cumulative effective mass of the structure has reached 90% of the total mass. For these two frequencies, the damping ratio ζ_n is set equal to 5%.

Table 2.5: Rayleigh damping coefficients.

Crownwall	f_1 [Hz]	f_2 [Hz]	ζ_1 [%]	ζ_2 [%]	α [s^{-1}]	β [s]
Unsupported	25	600	5	5	15.08	$2.5465 \cdot 10^{-5}$
Supported	35	950	5	5	21.21	$1.6158 \cdot 10^{-5}$

Figure 2.13 shows the damping ratio as a function of frequency for both crownwalls, the unsupported wall in blue and the supported wall in orange, where the circles indicate the first five eigenfrequencies. The figure shows how for $25\ Hz$ and $35\ Hz$ the damping ratio equals 5%, for the unsupported and supported walls respectively. For the first eigenfrequencies, the damping ratio is around 4% for both walls and for the second to the fifth eigenfrequencies, the ratio is about $2-3\%$.

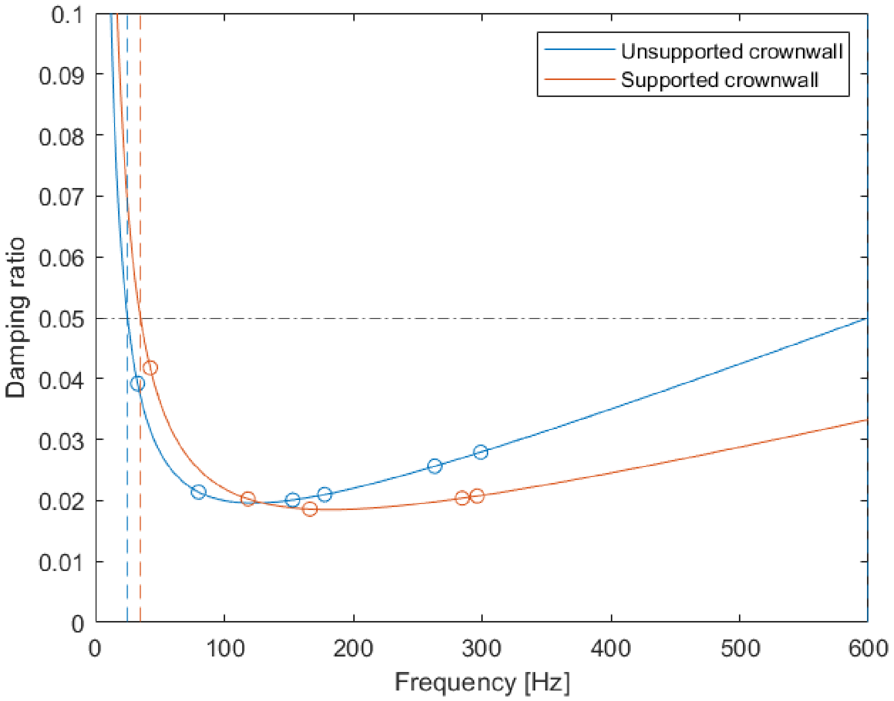

Figure 2.13: Damping ratio as a function of frequency, where the circles indicate the first five eigenfrequencies of the crownwalls.

2.2.5. Nonlinear model

A total strain-based crack model was selected as the nonlinear cracking model. The development of the constitutive model was based on the Modified Compression-field Theory by Vecchio and Collins (1986) and the 3D extension of that theory by Selby and Vecchio (1993). The total strain-based model is a so-called smeared crack model, which models cracking as a distributed effect over a specific area and the cracked material is assumed to be in a continuum. This makes it possible to describe the tensile and compressive behaviour of the cracked material with a stress-strain relation. An alternative to a smeared crack model is a discrete crack model. When using the discrete crack model, the crack is modelled as a displacement-discontinuity using an interface element to separate two solid elements. This a more accurate method to model cracks, as they are defined as a geometrical discontinuity in the concrete, but the smeared crack concept is more suitable for the finite element displacement method and requires less computational effort (Rots, 1991; DIANA FEA BV, 2021).

There are two possible approaches for the total strain-based model, the fixed crack approach and the rotating crack approach. The fixed crack approach evaluates the stress-strain relation in a fixed coordinate system and the crack's orientation is assumed constant. The rotating crack approach evaluates the stress-strain relation in a constantly rotating coordinate system that turns with the direction of the principal strain. As the name indicates, the crack's orientation continuously rotates as well. In the fixed crack approach, the crack may be loaded in shear and therefore, shear retention needs to be assumed, which is not required for the rotating crack approach (Rots, 1991; Naeimi & Moustafa, 2017; DIANA FEA BV, 2021). For the model's simplicity, the rotating crack approach is chosen for the analysis.

The compressive behaviour of the concrete is defined according to the compression curve in Eurocode 2 (EN 1992-1-1, 2004) presented in figure 2.14a. The compressive strength of the concrete is the same as for the linear material model, $f_{cm} = 43MPa$, the strain at maximum stress is $\varepsilon_{c1} = 0.00225$ and the strain at ultimate stress is $\varepsilon_u = 0.0035$ for concrete C35/45 (EN 1992-1-1, 2004). For the tensile behaviour of the concrete, a linear tension softening curve based on the fracture energy G_f is chosen and can be seen in figure 2.14b. Fracture energy is defined as the energy absorbed per unit area of the crack as it forms (Słowik, 2019) and it can be computed with the following equation from the Model Code 20210 (Fib, 2013):

$$G_f = 73{f_c}^{0.18}.$$

This gives $G_f = 144N/m$ for concrete C35/45. For smeared crack models, it is also common to relate the tensile behaviour to the crack bandwidth h, defined as the width over which the cracks are spread. As figure 2.14b shows, the area under the tension softening curve equals the fracture energy divided by the crack bandwidth. Govindjee's projection method is used for the crack bandwidth specification, which considers the crack's direction and the element's size in that direction.

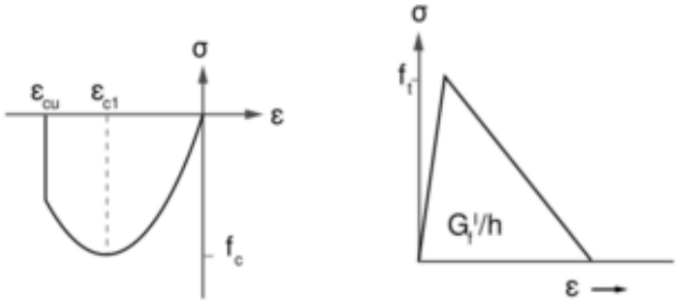

(a) Compression curve as defined in EN 1992-1-1.

(b) Linear tension softening curve based on fracture energy.

Figure 2.14: Compressive and tensile material behaviour for the total strain crack model (DIANA FEA BV, 2021).

3

Results

3.1. Wave load

3.1.1. Pressure impacts and loading domain

Figure 3.1 shows the pressure distribution at the moment of maximum total force for each wave of the three wave states. The localized maximum pressure is defined as the maximum pressure value along the height of the crownwall at the moment of the maximum total force. For waves 6 and 7 of wave state 5 (figure 3.1a), the pressure distribution resembles a trapezoidal distribution with maximum pressure values at the bottom of the wall. However, there is still a slight increase in pressure at the top of the curve (around probes 41-49). This indicates that the wave reaches the top of the curve, so the load has a small impulsive part but is mostly quasi-static. For wave 3, the largest wave of wave state 5, the maximum pressure, occurs at probe 45 at the top of the curve of the crownwall.

As figures 3.1b-3.1c show, for these larger waves characterized by impulsive load, the maximum pressure occurs at probes 47-49, and the pressure distribution is characterized by the C-CI phenomenon (Castellino et al., 2018a). For W6, wave 3, shown in yellow in figure 3.1b, results in the maximum pressure at probe 38. The pressure distribution at the moment of maximum total force for this wave is entirely different from any other wave in all three wave states. To investigate this further, figure 3.3 shows individual time frames of the video from the CFD model of wave 3 in W6 and figure 3.2 shows the time series of the total force of that wave. The red dots in figure 3.2 mark the force at the time of each time frame in figure 3.3. Figure 3.3 shows that for time t=34-34.4s, the water level at the face of the crownwall is increasing with the incoming wave crest. However, as the wave has not yet hit the curve of the crownwall, the total force is only slightly increasing as shown in figure 3.2. At time t=34.6s, the wave first hits the centre of the curve and then, at nearly the same instance, the lower part of the curve. The maximum total force is reached at time t=34.7s but at that time the wave has not yet reached the top of the curve as can be seen from figure 3.2e. At time t=35s, see figure 3.2f, the wave has reached the top of the crownwall, is deflected seawards and the total force is decreasing again. As figures 3.2d-3.2f show, the water column never completely fills the curve of the crownwall. Using linear wave theory, the maximum vertical velocity of each wave state can be computed using equation 3.1.

$$u_z = \omega a \frac{sinh[k(d+z)]}{sinh(kd)} cos(\omega t - kx) \tag{3.1}$$

where the angular frequency is $\omega = 2\pi/T$, the wavenumber is $k = 2\pi/L$ and the amplitude is $a = H/2$. The maximum vertical wave velocity of W6 is $u_{z,W6} = 2.4m/s$ while for W5 and W7, the maximum vertical wave velocity is $u_{z,W5/7} = 2.0m/s$. So, the maximum vertical velocity of W6 is 20% larger than the maximum vertical velocities of W5 and W7. As shown in table 2.1, W6 has the steepest waves with wave steepness $s = 6$% while W7 has the smallest steepness of $s = 3.7$%. Due to the large vertical velocity component and the large wave steepness the largest waves of W6 hit the crownwall in this manner instead of flowing up the curve.

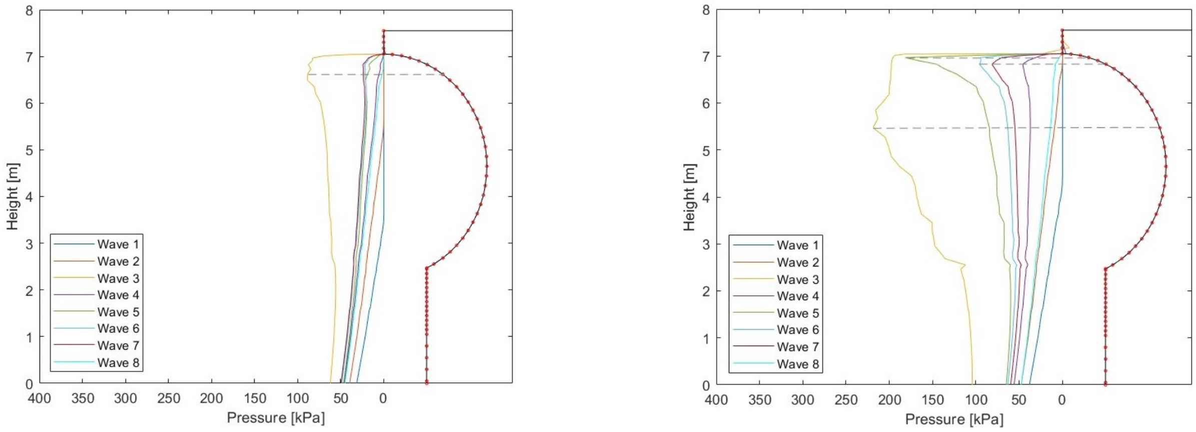

(a) W5 ($H = 5m$, $T = 8s$). **(b)** W6 ($H = 6m$, $T = 8s$).

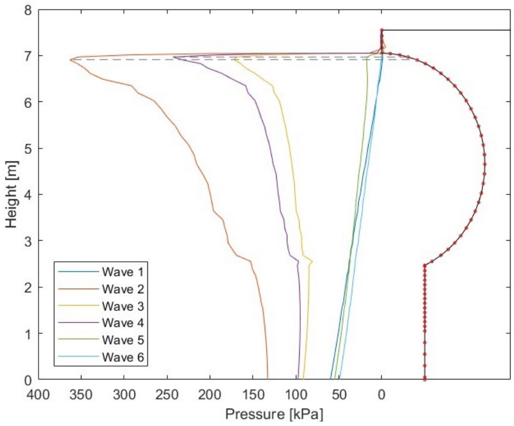

(c) W7 ($H = 7m$, $T = 11s$).

Figure 3.1: Pressure distribution along the height of the crownwall at the moment of maximum total force for each wave in the three wave states. The red dots on the crownwall represent the 56 probes and the grey dashed lines show the location of the maximum pressure for the largest waves.

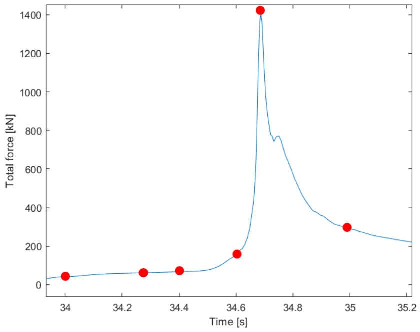

Figure 3.2: Time series of the total force of wave 3 in W6. The red dots represent each time frame in figure 3.3.

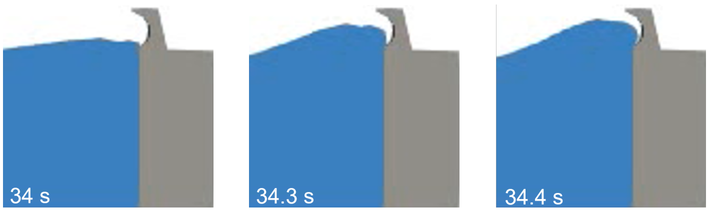

(a) Time frame at t=34s. **(b)** Time frame at t=34.3s. **(c)** Time frame at t=34.4s.

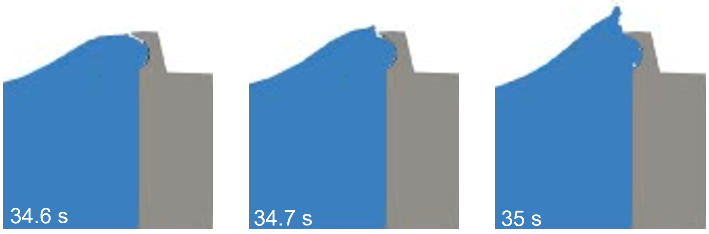

(d) Time frame at t=34.6s. **(e)** Time frame at t=34.7s. **(f)** Time frame at t=35s.

Figure 3.3: Time frames of the video from the CFD model of wave 3 of W6.

The third and largest wave state, W7, is the only one with a relative freeboard, R_c/H, smaller than 1 (see table 2.1). The large waves in W7 flow more smoothly up the curve of the crownwall than the waves in W6 and the water column fills the whole curve. The maximum pressure of the three largest waves occurs at probes 48 and 49. This is consistent with Dermentzoglou (2021) results, which showed with physical model tests on a fully curved crownwall under non-breaking wave loading, that higher and longer waves result in more significant loading and generate larger impacts. The shapes of the pressure distributions also compare well with the results of Dermentzoglou (2021).

The wave impacts are now analysed and defined as either quasi-static, dynamic or impulsive according to the conditions given in table 2.2 for the ratio between the maximum impact pressure and quasi-static pressure (P_{Im}/P_{qs+}). Waves that only show very small or no pressure at probe 51 are not included in this analysis, as they are not of interest regarding the structural analysis of the crownwall. The study includes wave 3 in W5; waves 3, 4, 5, 6 and 7 in W6 and waves 2, 3 and 4 in W7. The results are in table 3.1, where for each wave it is specified at which probes it is the quasi-static, dynamic or impulsive type. When compared to figure 3.6 of the total forces acting on the crownwall and figure 3.1 of the pressure distribution for the three largest waves of each wave state, it can be seen that as the waves get larger, they have an impulsive impact type at a larger portion of the wall. Most of the pressure impacts are defined as impulsive for the upper part of the curve but otherwise dynamic. However, the largest waves of W6 and W7 are defined as impulsive for the whole curve and are only dynamic at the lower part of the vertical part of the crownwall. The smallest wave of W6 is the only quasi-static wave, at the bottom of the crownwall.

Table 3.1: Pressure impact types at different probes on the crownwall.

Wave state	Wave number	Quasi-static	Dynamic	Impulsive
W5	3	-	1-29	30-51
W6	3	-	1-5	6-51
	4	1-2	3-34	35-51
	5	-	1-27	28-51
	6	-	1-30	31-51
	7	-	1-32	33-51
W7	2	-	1-11	12-51
	3	-	1-31	32-51
	4	-	1-26	27-51

The eigenfrequencies of the crownwalls first eigenmode are $32.8Hz$ and $42.6Hz$, for unsupported and supported wall respectively (see chapter 2.2.3). The natural periods of the two crownwalls are therefore $T_{n,unsup} = 1/32.8Hz = 0.030s$ and $T_{n,sup} = 1/42.6Hz = 0.024s$. Table 3.2 shows how the impulses are defined in the quasi-static, dynamic and impulsive domain of the crownwalls based on the impulse duration, according to the conditions given in table 2.3.

Table 3.2: Impulse duration for each loading domain of the crownwalls according to conditions given in table 2.3.

Crownwall	T_n [s]	Quasi-static [s]	Dynamic [s]	Impulsive [s]
Unsupported	0.030	$\geq$ 0.12	0.0075 - 0.12	$<$ 0.0075
Supported	0.023	$\geq$ 0.096	0.0060 - 0.092	$<$ 0.0060

The impulse durations for the waves in table 3.1 are determined according to the derivative method described in chapter 2.1.2, where the derivative of the pressure impacts is used to determine the beginning and end points of the impulses. The results are shown in figure 3.4. The one wave in W5 is shown in yellow, the waves in W6 are in various shades of blue, and the waves in W7 are in various shades of green. The wave impacts defined as impulses in table 3.1 are shown as diamonds and the dynamic impacts are shown as circles. The red dots on the crownwall indicate the probes. As stated before, this analysis is only performed for probes 9, 23, 28, 33, 37, 42, 47 and 51 as it is quite time-consuming. The black solid and dashed lines in figure 3.4 show where the dynamic and quasi-static domains of the unsupported and supported crownwalls split, at $T_d = 0.12s$ and $T_d = 0.096s$ respectively. Impulses to the right of the black lines are in the dynamic domain, and impulses to the left of the lines are in the quasi-static domain. No impulses reach the impulsive domains. The figure shows that those pressure impulses in the dynamic domain are in the top part of the curve, where the maximum pressures occur for most waves. The longest impulse durations are around the centre of the curve for all the waves rather than in the lower part. That is because, in the centre of the curve, the pressure rises more quickly than in the lower part of the crownwall, and therefore the impulse begins earlier.

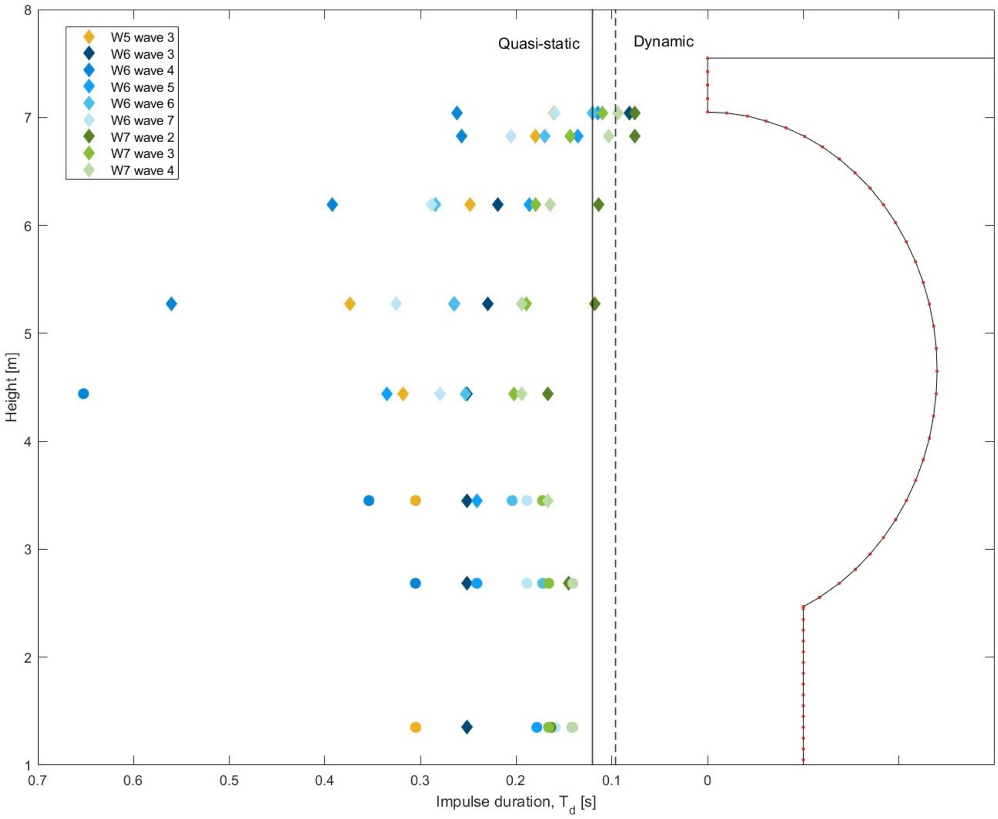

Figure 3.4: Impulse duration along the wall height for the waves in table 3.1.

As the unsupported crownwall has a longer natural period, there are more impulses in the dynamic domain of that crownwall than the supported crownwall. All three waves of W7 have at least one pressure impulse in the dynamic domain of the unsupported crownwall, and the largest wave (wave 2) has impulses in the dynamic domain from the centre of the curve to the top. The three largest waves of W6 (waves 3, 5 and 6) also have at least one pressure impulse in the dynamic domain, while the two smaller ones (waves 4 and 7) and the one wave of W5 are only in the quasi-static domain. For the supported crownwall, the largest two waves of W7 and the largest wave of W6 are in the dynamic domain at the top of the curve, while all other waves are only in the quasi-static domain. The wave with the longest impulse duration is wave 4 of W6, the smallest of the nine waves and the only wave defined as quasi-static at the bottom of the wall in table 3.1. These results confirm that a structural dynamic analysis of the crownwalls is needed for W6 and W7, but a dynamic analysis will also be performed for W5.

Figure 3.5 shows the resulting impulses (using equation 2.1) along the height of the wall. The largest impulses are for wave 3 in W6, which coordinates with the pressure distribution at the moment of maximum pressure shown in figure 3.1b. However, at the very top of the curve, the largest impulses are for wave 2 of W7, which is the largest overall wave. For all the waves, the largest impulses are above the centre of the curve, around probes 37-42, where the impulse duration is longer than at the very top and the pressure is larger than lower in the curve. The impulses are found to be much less variable for W6 and W7 than the maximum pressure values. This is in accordance with the findings of i.e. Bagnold (1939), De Almeida and Hofland (2020), and Dermentzoglou (2021) which all found that the variability in pressure impulses was much less than the variability in the peak pressures of wave impacts.

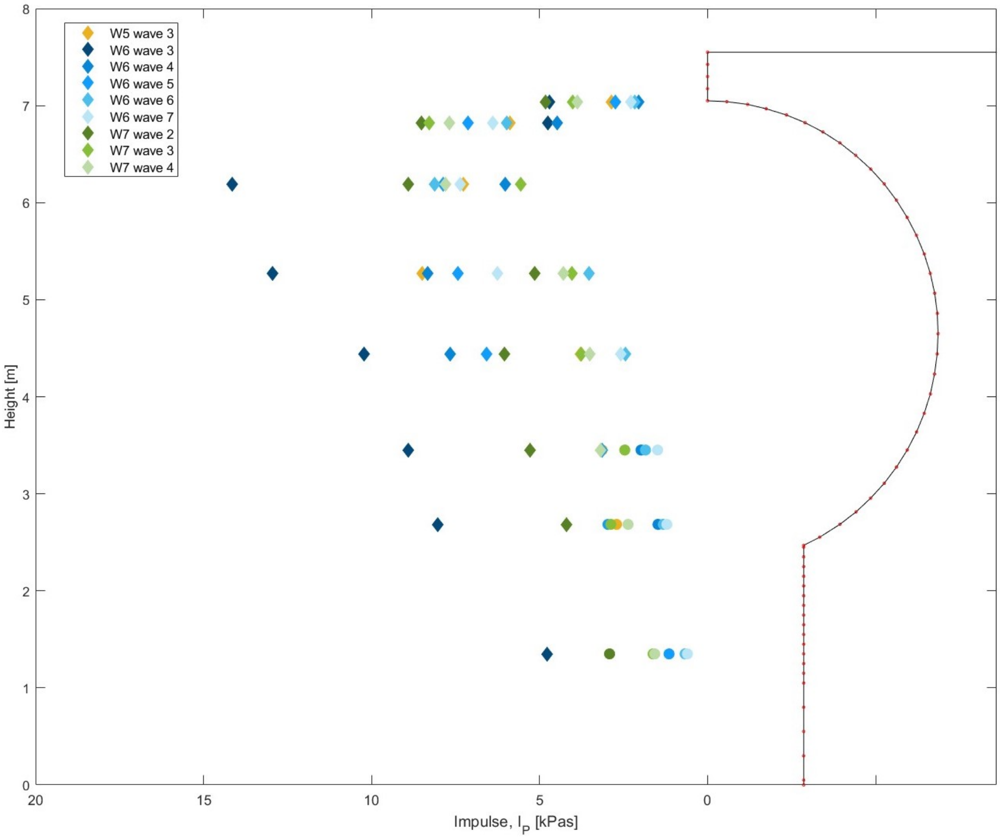

Figure 3.5: Impulses along the wall height for the waves in table 3.1.

3.1.2. Force

The total force, F_T, is simply the integral of the pressure along the height of the wall at each moment in time. Table 3.3 shows the maximum total force (F_T, max) of each wave, the ratio between the maximum total impact force and the maximum quasi-static force (for those waves that have an impulsive and quasi-static part), the impact type according to table 2.2 and the impulse. The derivative method described in chapter 2.1.2 and used for the pressure impacts is also used for the force impacts to determine the beginning and end points of the force impulses. For W5, only the largest wave is impulsive with an impulse of 34 kNs, W6 has four impulsive waves and W7 has three. As was found for the pressure impulses, the force impulses of W6 and W7 are much less variable than the maximum total forces. The large force impulse of wave 3 in W6 can again be explained by the unique pressure distribution shown in figure 3.1b, as that wave has high pressure along the height of the crownwall and the impulse duration is relatively long.

Figure 3.6 shows the time series of the total force acting on the crownwall for each wave state and the horizontal and vertical components. It can be seen from the figures that for each wave state, the quasi-static part of the load is relatively constant while the impulsive part varies greatly. The waves that result in the largest instantaneous total force are the 2nd or 3rd waves for all three wave states. This is consistent with the findings of Martinelli et al. (2018), where the force time series obtained by a physical model test of a recurved crownwall under wave loading were compared to the force-time series obtained by the numerical model test of Castellino et al. (2018a).

With increasing wave height, the wave load increases, as expected. It is interesting to see that the increase in wave height has more effect on the maximum instantaneous total force (the impact) than on the quasi-static part of the force, as the maximum total force ($F_{T,max}$) of W6 is 245% larger than the maximum total force of W5. However, the maximum quasi-static force ($F_{T,qs+}$) is only 135% larger. This might be explained by the fact that the waves in W5 are big enough to fill the curve of the crownwall but not big enough to result in an impact at the top of the curve (C-CI). When both the wave height and wave period are increased, it is the other way around where $F_{T,max}$ for W7 is about 130% larger than W6 and $F_{T,qs+}$ is about 160% larger. This can also be seen from the results in table 3.3, where the ratio $F_{T,max}/F_{T,qs+}$ for waves in these two wave states with similar $F_{T,max}$ is greater for waves in W6 than in W7. It is difficult to say for sure what is causing this based on only these two wave conditions. Still, it can be assumed that when the waves are big enough for C-CI to occur at the top of the curve, increasing the wave height and wave period has a greater impact on the quasi-static part of the load than the impulsive part.

Table 3.3: Maximum total force, impact type and impulse for each wave.

Wave state	Wave number [-]	$F_{T,max}$ [kN]	$\frac{F_{T,max}}{F_{T,qs+}}$ [-]	Impact type [-]	Impulse [kNs]
W5	1	55	-	Quasi-static	-
	2	110	-	Quasi-static	-
	3	580	3.5	Impulsive	34
	4	185	1.2	Dynamic	-
	5	240	1.5	Dynamic	-
	6	255	1.6	Dynamic	-
	7	265	1.6	Dynamic	-
	8	170	1.2	Dynamic	-
W6	1	84	-	Quasi-static	-
	2	175	1.2	Dynamic	-
	3	1420	6.2	Impulsive	81
	4	365	2.0	Dynamic	-
	5	735	4.0	Impulsive	36
	6	565	3.0	Impulsive	35
	7	490	2.6	Impulsive	34
	8	205	1.3	Dynamic	-
W7	1	225	-	Quasi-static	-
	2	1890	5.1	Impulsive	62
	3	950	2.6	Impulsive	44
	4	1160	3.6	Impulsive	45
	5	265	1.3	Dynamic	-
	6	185	1.1	Quasi-static	-

The total force can be split into horizontal and vertical components, as the load acts horizontally and vertically at the curved part of the crownwall. The horizontal component is much larger than the vertical component for all wave states, which is expected. Another factor to consider for the vertical force is the effect of the fully curved shape of the wall. The wave pressure acting on the lower part of the curve (probes 22-33) results in a negative vertical force acting downward, while the pressure acting on the top of the curve (probes 35-51) results in a positive vertical force acting upwards. So, if the waves are not large enough to put much pressure on the uppermost part of the curve, the result might be a small downward-acting vertical force. This is the case for W5, where only one wave in the wave series is big enough to result in a total vertical force acting upwards. For the three intermediate waves (waves 5, 6 and 7), the pressure on the upper part of the curve almost fully compensates the pressure on the lower part of the curve and the total vertical force is close to zero at the moment of maximum pressure (see figure 3.1a for the pressure distribution). The total vertical force acts downward for the four smallest waves (waves 1, 2, 4 and 8). For W6 and W7, the three smallest waves also result in a downward-acting total vertical force, while the larger waves result in an upward-acting force.

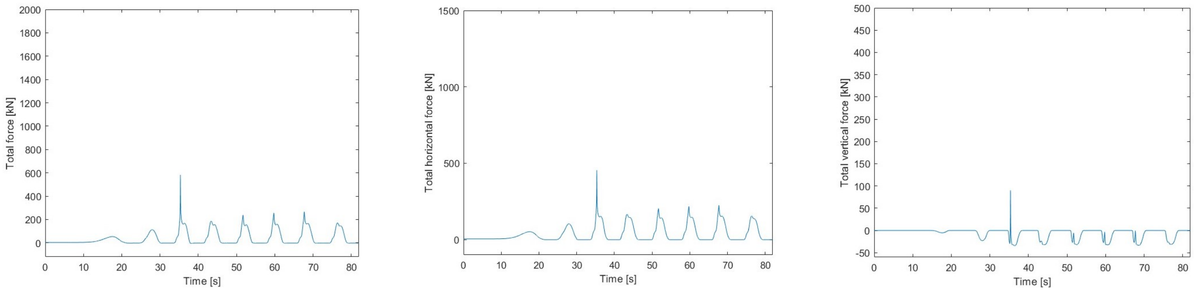

(a) Total force of W5. **(b)** Horizontal force of W5. **(c)** Vertical force of W5.

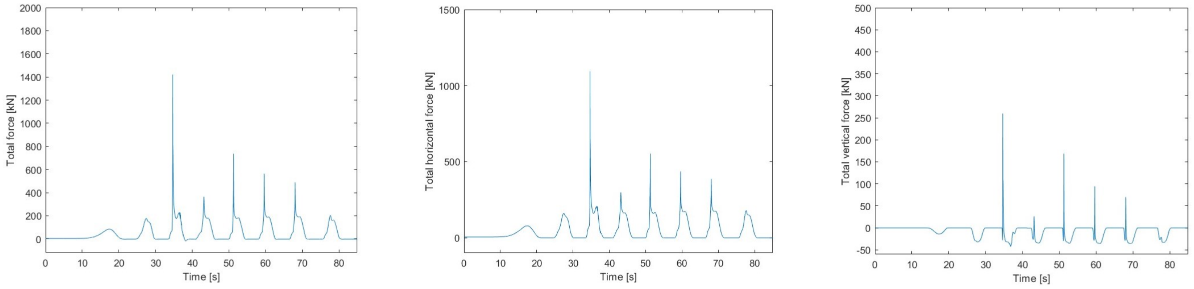

(d) Total force of W6 **(e)** Horizontal force of W6. **(f)** Vertical force of W6.

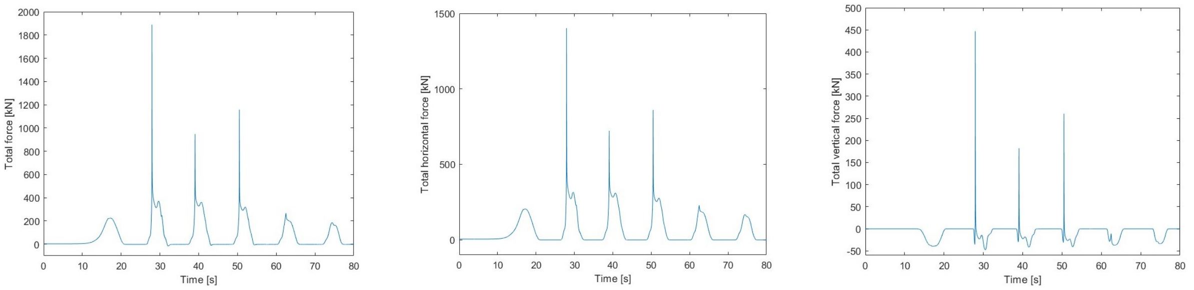

(g) Total force of W7. **(h)** Horizontal force of W7. **(i)** Vertical force of W7.

Figure 3.6: Time series of the total, horizontal, and vertical force.

The time series of the total force for the three wave states all show a change in the slope of the force when it is increasing. The force slowly increases at the beginning of the wave and then the slope of the force series rises sharply. The largest wave in W7 is taken as an example in figure 3.7. The wave starts acting on the crownwall at time t_1. At the moment of the increase in the slope of the total force series, time t_2, the wave has reached the curve of the crownwall and a negative vertical force can be seen. At t_3, the wave has reached the top of the curve and the vertical force becomes positive. The pressure then increases and reaches a maximum at t_4 (see figure 3.1c for the pressure distribution at that time), which results in the maximum total force. As the wave is deflected seawards by the crownwall and the water level falls, the pressure reduces again, creating a slowly varying quasi-static force until no force is acting on the crownwall anymore at time t_5.

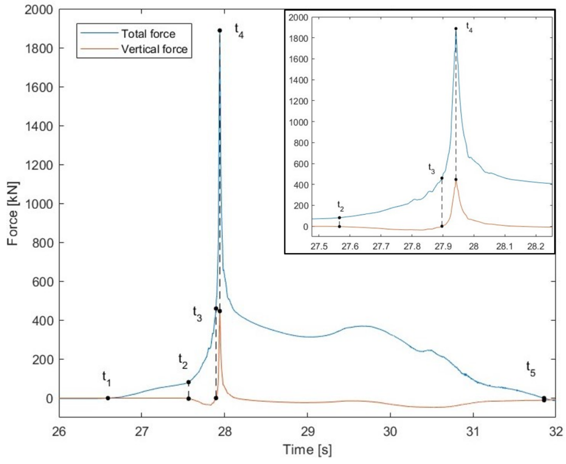

Figure 3.7: Total and vertical force of the largest wave in W7.

The point of application of the total force can be calculated using a weighted average of the force along the height of the wall for each wave j (Castellino et al., 2021):

$$z_j = \frac{\sum_{i=1}^{56} P_i A_i z_i}{P_i A_i} \tag{3.2}$$

where P_i is the pressure at each probe i, A_i is the area surrounding each probe and z_i is the vertical distance from the bottom of the crownwall to the probe. Figures 3.8a-3.8c show the point of application of the maximum total force for the three largest waves in each wave state. It can be seen that the largest wave in W7 is the only wave that results in a slightly upward total force, at about 2° angle compared to horizontal. The second and third largest waves in W7 also have the point of application close to the centre of the curve, but the total force is angled slightly downward. The maximum total force of the two largest waves of W6, waves 3 and 5, is located at almost the same location between probes 33 and 34, but wave 3 (the largest) has a lower point of application. The dominant factor in the location of the point of application is the pressure distribution (Dermentzoglou, 2021). As figure 3.1b shows (and has been discussed before), the pressure distribution of wave 3 in W6 is different from all other waves, which explains this relatively low point of application. For W5, the point of application of the maximum total force of the largest wave is located between probes 31 and 32. The total force of the second and third largest waves of W5 has a point of application in the lowest quarter of the curve, which is in accordance with the trapezoidal pressure distribution (see figure 3.1a).

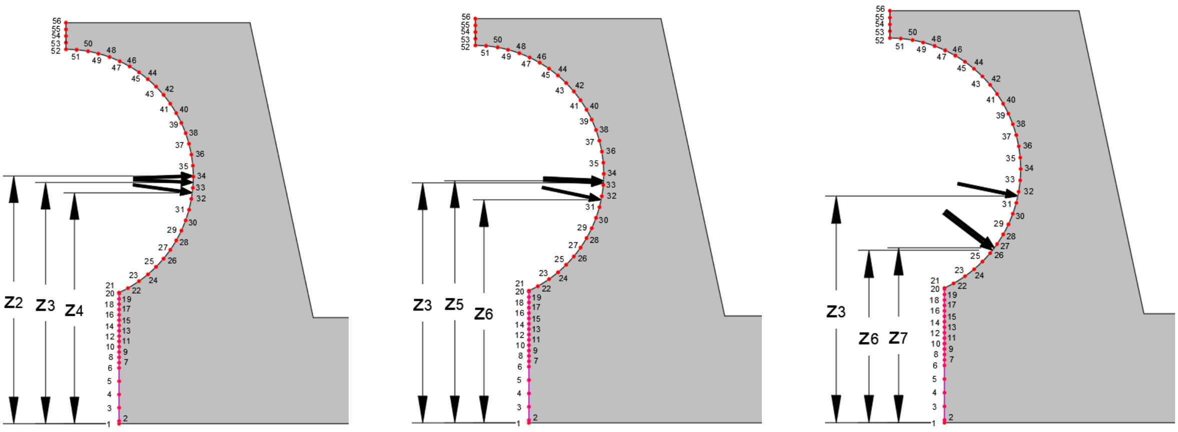

(a) W5 ($H = 5m, T = 8s$). **(b)** W6 ($H = 6m, T = 8s$). **(c)** W7 ($H = 7m, T = 11s$).

Figure 3.8: Point of application of the maximum total force of the three largest waves in each wave state.

3.2. Static analysis

The loads considered for the static analysis of the crownwall are the structure's self-weight, hydrostatic pressure and static wave pressure. Diana FEA considers the self-weight based on the input value of the mass density of concrete ρ. The hydrostatic pressure is computed as $P_W = \rho_W g d$, where ρ_W is the mass density of seawater, g is the acceleration due to gravity, and $d = 20m$ is the water depth in front of the crownwall. The method by Goda (1974) is widely used to calculate static wave pressure on vertical composite breakwaters. As a means to account for the C-CI phenomenon, Castellino et al. (2021) developed an extension to Goda's formulas, such that it can also be used for the static analysis of vertical breakwaters with a recurved parapet. The total static wave pressure is indicated by P_R and can be calculated using the following equation:

$$P_R = P_V(1 + \tilde{p}) \tag{3.3}$$

where P_V is the wave pressure acting on a vertical wall calculated with the Goda method and the factor $\tilde{p} = P_R/P_V$ is the parameterized wave pressure distribution, developed by Castellino et al. (2021). Three different equations are given for $\tilde{p}$ for three different heights along the wall: $\tilde{p}_1$ at S.W.L, $\tilde{p}_2$ at the centre of the curve and $\tilde{p}_3$ at the top of the curve. As the method was developed for a recurved crownwall but is used on a fully curved crownwall, some minor changes were made regarding applying the equations. The entire calculation method, assumptions and results can be found in appendix A. Figure 3.9b shows the three different pressure distributions that make up the total static load of W7 on the crownwall. Figure A.1 shows the static wave pressure on a vertical wall calculated with Goda's formulas P_V, figure 3.9b shows the parameterized wave pressure distribution for the curved crownwall $\tilde{p}$ and figure 3.9c shows the hydrostatic pressure P_W.

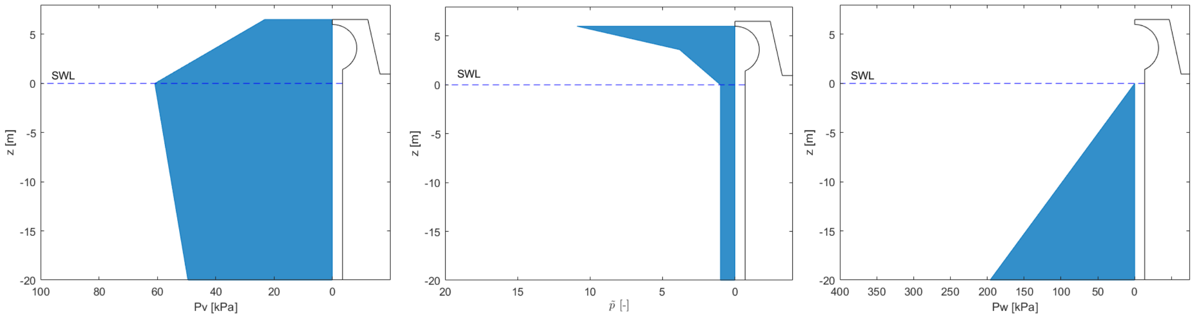

(a) Static wave pressure.

(b) Parameterized wave pressure distribution.

(c) Hydrostatic pressure.

Figure 3.9: Three pressure distributions that are combined into the total static pressure on the crownwall (W7: $H = 7m$, $T = 11s$).

When the total static wave pressure P_R has been computed using equation 3.3, the hydrostatic pressure is added to obtain the total static pressure on the crownwall. Figure 3.10 shows these results for the three wave states and the maximum pressure distribution of the CFD-generated pressure time series at the moment of maximum total force. It can be seen that the static pressure distribution, using the extended Goda method, fits quite well with the maximum pressure distribution for all wave states. The static maximum pressure at the top of the curve is slightly overestimated for all wave states and the pressure distribution along the whole wall for W5 and W7. Another thing that differs from the calculated static pressure is that the calculation method assumes that there will be pressure on the top of the crownwall above the curve. But as the CFD-generated pressure series shows, there will not be any pressure there as the curve deflects the wave seawards. Table 3.4 shows the maximum pressure, total force and point of application of the total force on the crownwall as a vertical distance from the bottom of the crownwall (equation 3.2), for the static load and CFD-generated wave load. The calculated maximum pressure is 2-11% larger than the maximum pressure of the CFD-generated pressure series, where the smallest difference is for W5 and the largest difference is for W6. The total force of the static load is however 5-35% larger, where the smallest difference is for W6 and the largest difference is for W5. This is due to the fact that the pressure difference along the height of the crownwall is the largest for W5, although the maximum pressure at the top is quite accurately estimated. The point of application of $F_{T,static}$ is also 0.1-0.5m higher than of F_T, where the largest difference is for W6. For both W6 and W7, $F_{T,static}$ is located above the centre of the curve and is acting upwards, at about 10° angle compared to horizontal.

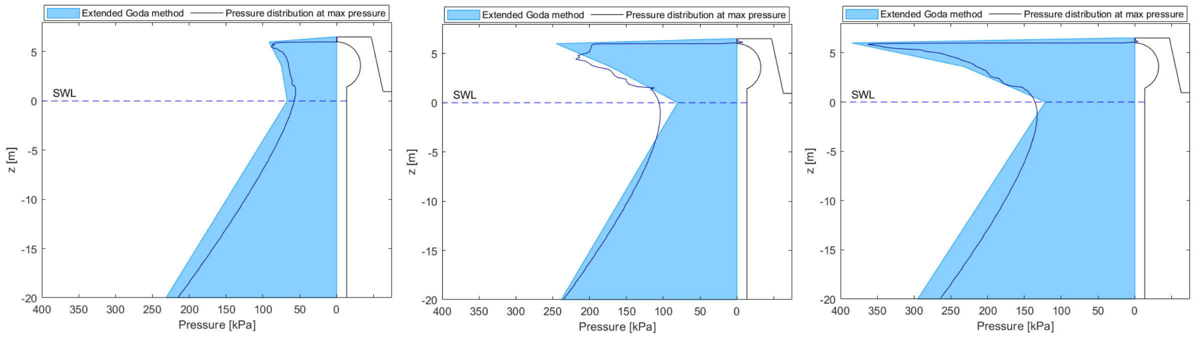

(a) W5 ($H = 5m, T = 8s$).

(b) W6 ($H = 6m, T = 8s$).

(c) W7 ($H = 7m, T = 11s$).

Figure 3.10: Total static pressure distribution shown as light blue surface and the pressure distribution at the moment of maximum pressure for each wave state shown as a dark blue line.

Table 3.4: Results of static load calculations compared to the CFD-generated wave load. P_{max} is maximum pressure, F_T is the total force and z is the the point of application of the total force as the vertical distance from the bottom of the crownwall.

Wave state	H [m]	T [s]	$P_{max,static}$ [kPa]	P_{max} [kPa]	$F_{T,static}$ [kN]	F_T [kN]	z_{static} [m]	z [m]
W5	5	8	92	90	785	580	4.3	4.2
W6	6	8	245	220	1495	1420	5.0	4.5
W7	7	11	384	360	2210	1890	5.1	4.7

The static wave and water pressure are applied to the FEM model in the same way as the CFD-generated pressure-time series. Static analysis is then performed for both the self-weight and the wave and water pressure, on both crownwalls and for all wave states. Figure 3.11 shows an example of the resulting stress distribution in the Y-direction of the two static load cases for W7 and the unsupported crownwall. It can be seen that the location of the centre of gravity of the head of the crownwall causes it to tilt to the left, causing compression in the front and tension in the back. As the wave load causes the crownwall to deflect to the right, there are tension stresses in the front and compressive stresses in the back, opposite to the self-weight. The displacements and stresses at each node for the two load cases are added to obtain the final results. The self-weight, therefore, reduces the maximum stresses and displacements but it has minimal effects on the stress and displacement distribution. The stress and displacement distributions of the final results will be identical to the resulting distribution of the static water and wave pressure (figure 3.11b-3.11d), as the self-weight results in much smaller displacements and stresses. The final results are in table 3.5. The table shows the maximum compressive and tensile stresses in global X- and Y-directions and the total displacement of probe 52 (see figure 2.2).

Comparing the results of the unsupported and supported crownwalls it can be seen that the tensile stresses in both X- and Y-direction are almost equal while the compressive stresses increase by about 70-100% in the X-direction and 55-80% in the Y-direction. The compressive stresses occur in the back of the crownwall. Therefore, it is fitting that adding the stiff boundary interface at the back face of the crownwall has greater effects on the compressive stresses than the tensile stresses. As figure 3.11 shows the high compressive stresses in the supported crownwall are much more localized than the high compressive stresses in the unsupported crownwall. Due to the higher stiffness of the supported crownwall, the displacement of probe 52 is about 30% less for all wave states. The tensile stresses in the Y-direction of W6 and W7 exceed the tensile strength of the concrete, $f_{ctm} = 3.2MPa$, which indicates that cracking will occur. The stress distribution of the stresses in the Y-direction, presented in figures 3.11b and 3.11d, show that the maximum tensile stresses are in the front of the crownwall, in the centre of the curve. These results are later compared to the results of the dynamic analysis, to estimate how reasonable it is to use the extended Goda method for the design of fully curved crownwalls.

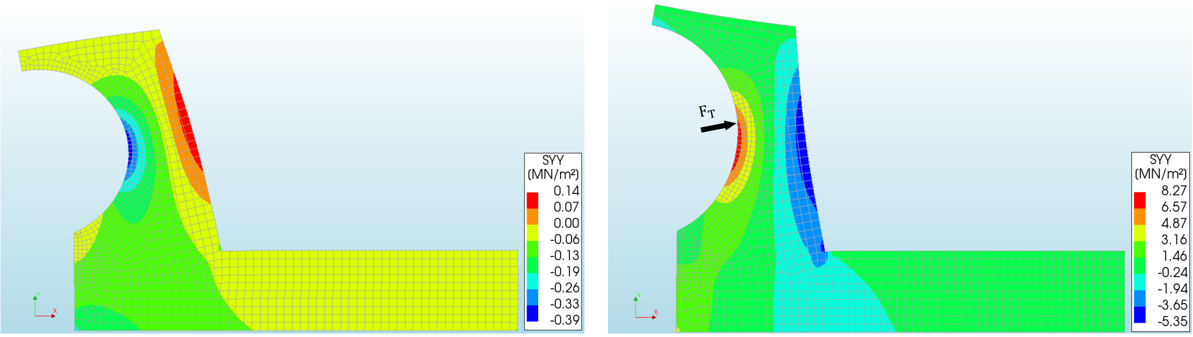

(a) Unsupported crownwall: self-weight.

(b) Unsupported crownwall: static water and wave pressure of W7.

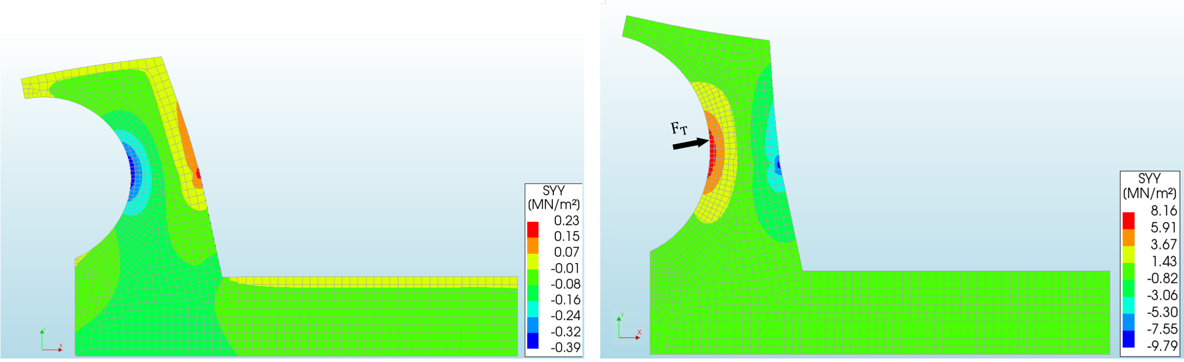

(c) Supported crownwall: self-weight.

(d) Supported crownwall: static water and wave pressure of W7.

Figure 3.11: Stress distribution of stresses in Y-direction as a result of applying self-weight and static water and wave pressure of W7.

Table 3.5: Static analysis results: maximum compressive (σ_c) and tensile (σ_t) stresses in global X- and Y-directions in the unsupported and supported crownwalls, for each wave state, and the total displacement of point 52 ($u_{XY,P52}$).

Crownwall	Wave state	H [m]	T [s]	$\sigma_{c,XX}$ [MPa]	$\sigma_{t,XX}$ [MPa]	$\sigma_{c,YY}$ [MPa]	$\sigma_{t,YY}$ [MPa]	$u_{XY,P52}$ [mm]
Unsupported	W5	5	8	-1.15	0.41	-1.45	1.68	0.77
	W6	6	8	-2.66	1.24	-3.41	5.00	2.18
	W7	7	11	-3.95	2.00	-5.22	7.89	3.41
Supported	W5	5	8	-1.93	0.41	-2.25	1.64	0.54
	W6	6	8	-5.24	1.24	-6.17	4.91	1.58
	W7	7	11	-8.09	1.99	-9.56	7.77	2.49

3.3. Dynamic analysis

3.3.1. Dominant mode

To identify the dominant mode of the unsupported and supported crownwalls a so-called virtual impact hammer test is performed. A time-varying triangular impulsive horizontal force is subjected to the top part of the crownwalls, the displacement time series is recorded at 43 points on the structures (see figure 3.14) and through Fourier transform the energy density spectrum of each point can be analysed. This same method was used by Dermentzoglou et al. (2021) to identify the dominant mode of a recurved crownwall. The force has a peak value of 800 kN and a duration of 2 ms (the same values as used by Dermentzoglou et al. (2021)). The duration is chosen such that the force is in the impulsive domain of the crownwalls: duration $<$7.5 ms for the unsupported crownwall and duration $<$6 ms for the supported crownwall.

Figure 3.12 shows the displacement time series in the x-direction of points 8, 16 and 34 of both the unsupported and supported crownwalls. The displacements are recorded for 7s to allow all the oscillation to damp down, but in the figures, only the first second is shown so that the most significant vibrations at the beginning of the time series can be seen more clearly. It can be seen that the displacements of the unsupported wall are larger than those of the supported wall and that the displacement at point 34, in the slab, is almost zero for both walls. It can also be seen that the period of the vibration of the unsupported crownwall is longer than that of the supported crownwall and the vibrations take slightly longer to die out. This is directly related to the eigenmodes of the two structures, as the unsupported crownwall has lower eigenfrequencies and therefore longer natural periods.

Figure 3.13 shows the energy density spectrum, on a logarithmic scale, of the 43 points. All density spectrums are in grey except the density spectrums of points 8, 16 and 34, which are shown in the same colours as the displacement time series: blue, orange and purple, respectively. The black dashed lines indicate the first five to six eigenfrequencies of the crownwalls. For both walls, it can be seen that there are clear energy peaks at the first eigenmode and another one close to the second eigenmode. The points at the top of the crownwall (6-16) have larger energy than points lower in the crownwall, as they have larger displacements. For the unsupported crownwall (figure 3.13a), there is a uniform reduction in energy between points, but for the supported crownwall (figure 3.13b), there is a visible gap in the spectrum at frequencies below 200 Hz. That is because the supporting wall greatly reduces the displacements of the points in the lower part of the vertical part of the crownwall (points 5-25).

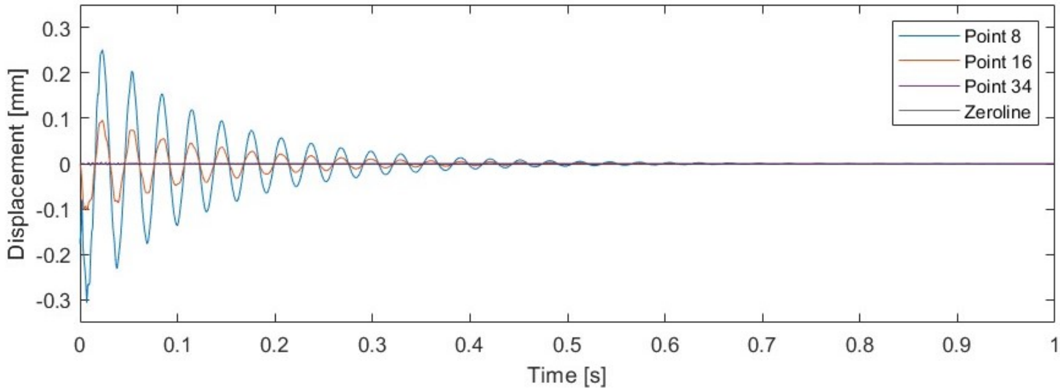

(a) Displacement time series of the unsupported wall.

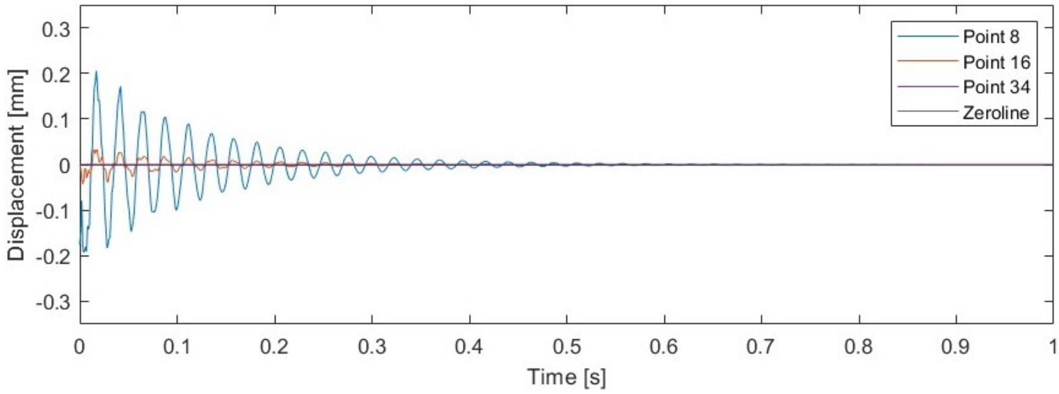

(b) Displacement time series of the supported wall.

Figure 3.12: Displacement time series in the x-direction of points 8, 16 and 34.

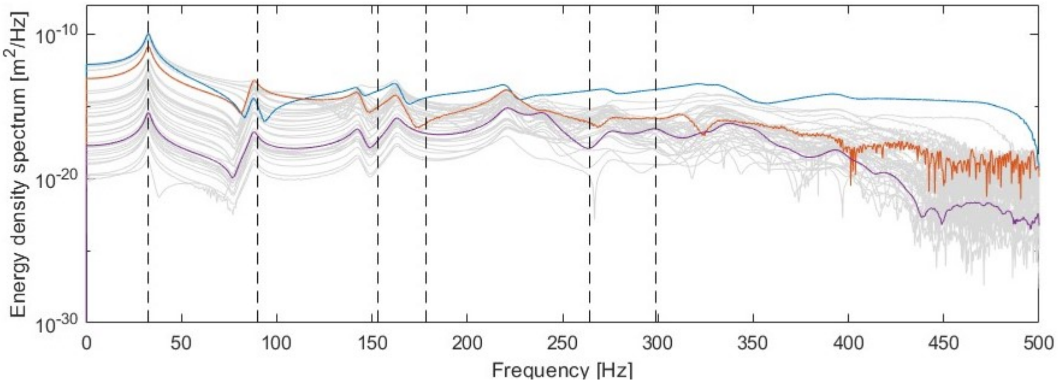

(a) Energy density spectrum of the unsupported wall.

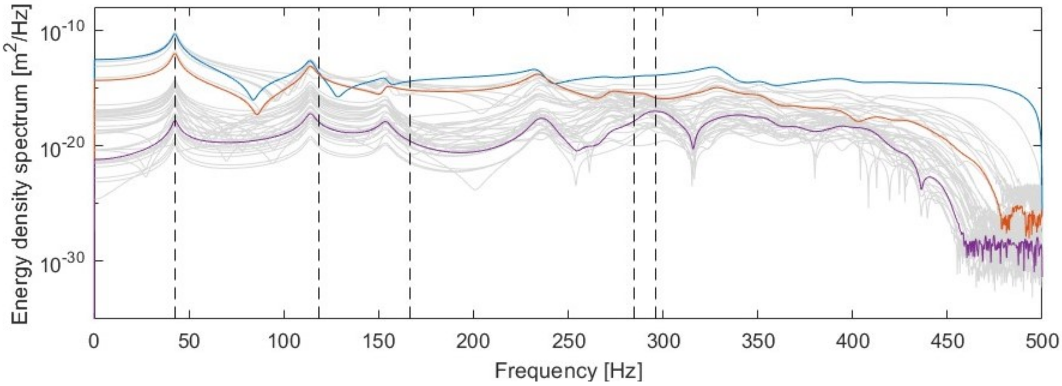

(b) Energy density spectrum of the supported wall.

Figure 3.13: Energy density spectrum, on a logarithmic scale, of all 43 points in light grey, points 8, 16 and 34 are shown in same colours as their displacement series in figure 3.12. The black dashed lines indicate the first five eigenfrequencies of the crownwalls.

The dominant mode of each point is defined as the frequency with the largest energy. For the unsupported wall, the dominant mode for most points is eigenmode 1. The only points with another dominant mode are points 29, 36, 38 and 43, which all have eigenmode 5 as the dominant mode and are all in the slab of the crownwall. For the supported wall, all points in the vertical part of the crownwall and in the front of the slab have eigenmodes 1 or 2 as the dominant mode. The points in the back of the slab have eigenmodes 4 or 5 as the dominant mode. Figure 3.14 shows the results where dominant mode 1 is shown in red, mode 2 in orange, mode 3 in purple, mode 4 in blue and mode 5 in green. This is in accordance with the effective mass shown in table 2.4, where it can be seen that the first eigenmode of both structures has the largest effective mass for the vertical part of the structure. The figures show that the unsupported crownwall has slightly more energy in the first eigenmode, as was expected given that the effective mass in the X-direction was 18.4% for the unsupported crownwall but 10.3% for the supported crownwall. For the supported crownwall, eigenmode 5 has the largest effective mass in the X-direction out of the first five eigenmodes, with 38.3% of the total mass of the structure activated. However, for the unsupported crownwall, eigenmode 6, which shows activation of the back of the slab, had 17.2% of the total mass of the structure activated. The results reflect this difference between the two crownwalls well, as the supported crownwall has eigenmode 5 as the dominant mode for most of the slab and it can be assumed that the slab plays a more critical role in the dynamic response of the supported crownwall than the unsupported crownwall.

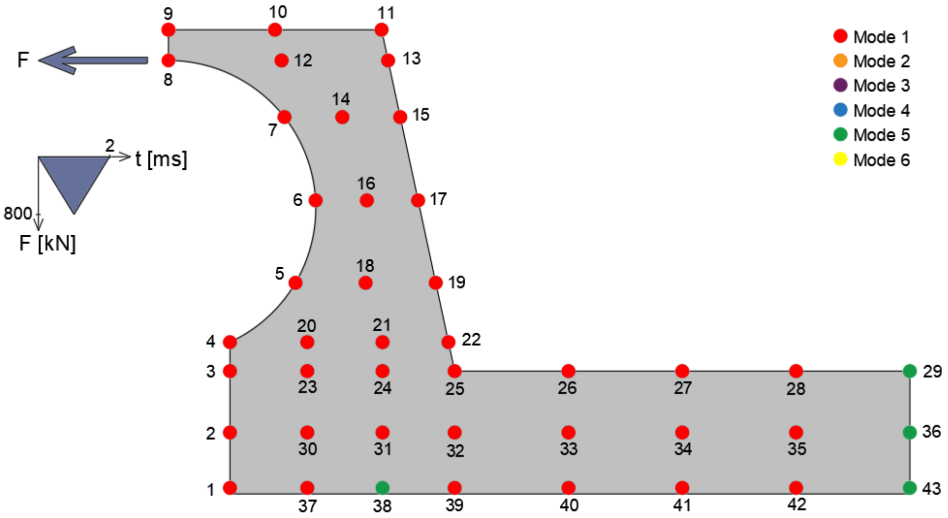

(a) Dominant modes of the unsupported crownwall.

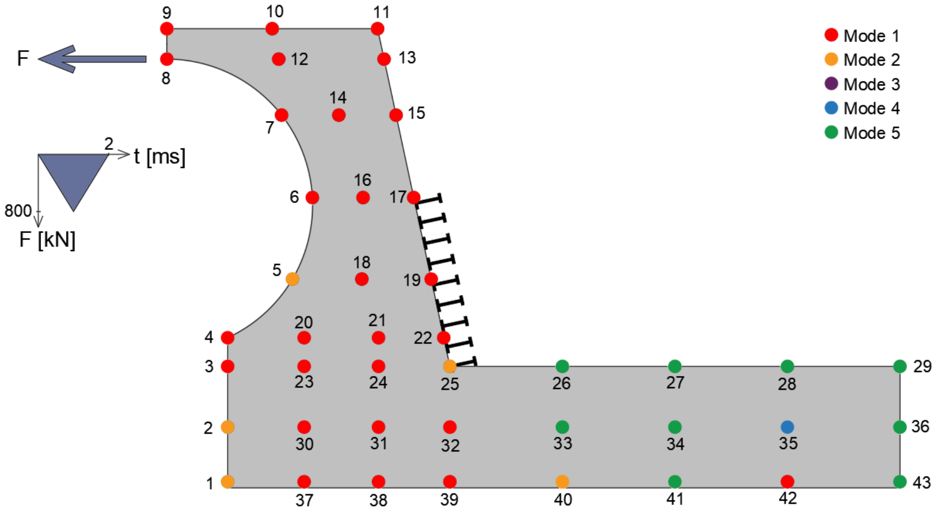

(b) Dominant modes of the supported crownwall.

Figure 3.14: The impact hammer time varying force, F, and the results of the dominant mode analysis.

3.3.2. Linear analysis

A linear dynamic transient analysis is performed for the unsupported and supported crownwalls, under wave loading from all three wave states. Concrete is weak in tension and the static analysis showed that for W6 and W7, high tensile stresses occur in the centre of the curve of the crownwall. As pressure impulses of W6 and W7 are in the dynamic domain of the crownwalls, a dynamic analysis is needed to evaluate the structural response. The linear analysis results will be used to compare the response of the crownwall to different wave states and see how the added supporting wall affects the dynamic response.

Figure 3.15 shows the wave pressure-time series and the resulting displacement-time series of probe 52 in XY-direction, for both crownwalls, for the largest wave in W7. The dark blue line shows the pressure-time series at the centre of the curve, the light blue line indicates the pressure-time series at the top of the curve, the orange line shows the displacement-time series of the unsupported crownwall and the dark orange line shows the displacement-time series of the supported crownwall. It can be seen that when the wave has reached the centre of the curve, the deflection of the top of the crownwall starts. It slowly deflects until the wave has reached the top of the curve when both the deflection and pressure increase sharply. At the moment of maximum pressure, the displacements also reach a maximum. The crownwalls then vibrate with the frequency of their first eigenmodes, 32.8 Hz for the unsupported crownwall and 42.6 Hz for the supported crownwall. This is due to the fact that the first eigenmode has its maximum modal ordinate at the top of the structure and as can be seen in figure 3.16, the displacements due to the wave load are largest at the top and the displacement distribution replicates the modal shape of the first eigenmode (see figures 2.11a and 2.12a). The maximum displacement of the supported crownwall is about 35% smaller than the maximum displacement of the unsupported crownwall.

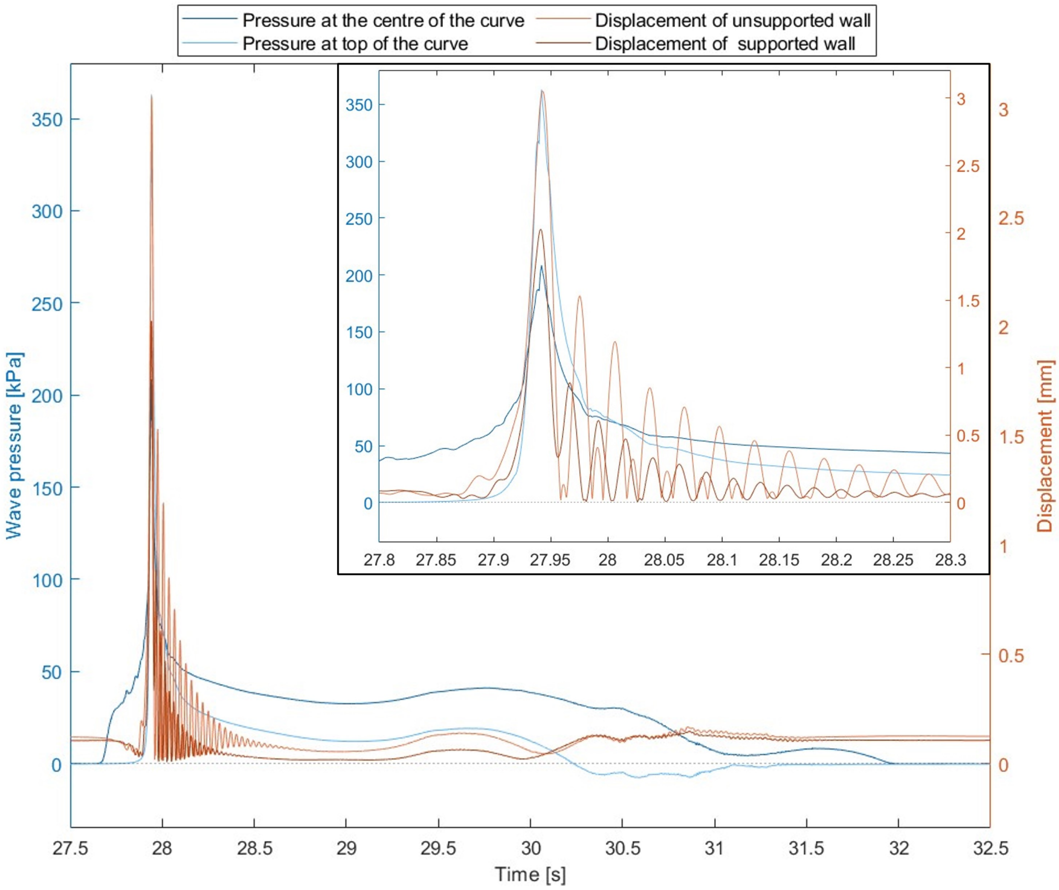

Figure 3.15: Pressure- and displacement-time series.

Figure 3.16 shows a contour plot of the displacements in the XY-direction of both the unsupported and supported crownwall at the moment of maximum deflection for W7, as well as the pressure distribution and the location of the total force at that moment. The vertical part of the unsupported wall is entirely free to deflect, while the supported wall can only deflect above the supporting wall. That means that the bending moment arm from the point about which they can deflect to the horizontal load is much smaller for the supported wall and therefore, the displacements are smaller. The eigenvalue analysis has also shown that the supported wall is stiffer and so, it is fitting that for the same applied force the displacements are smaller for the stiffer wall.

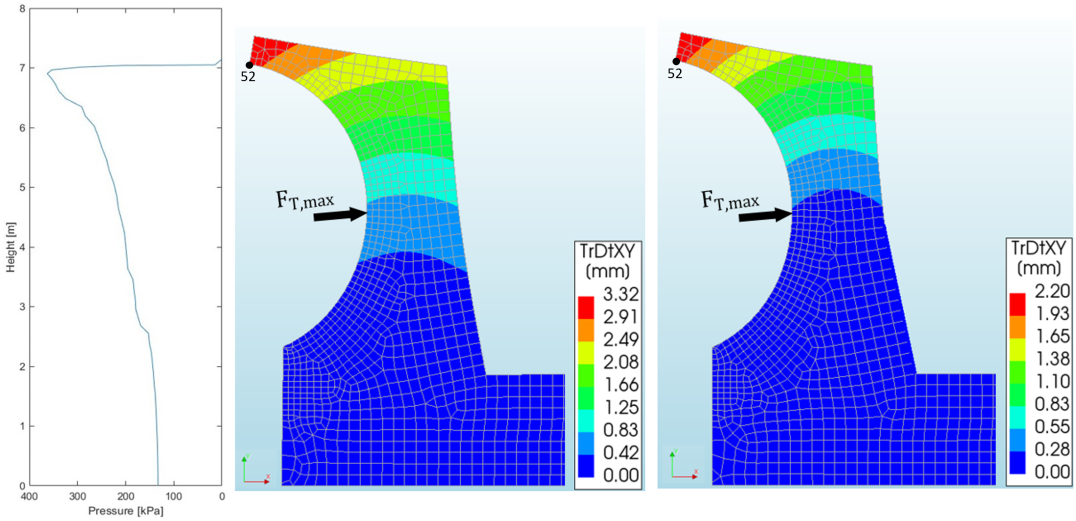

Figure 3.16: Displacement contour plots of W7 at the moment of maximum deflection, unsupported crownwall to the left and supported crownwall to the right. Also shown is the pressure distribution and the location of the total force at that moment.

The main results of the analysis are shown in table 3.6. The table shows the wave height (H) and wave period (T) of the wave states, the maximum compressive and tensile stresses in the X-direction ($\sigma_{c,XX}$ and $\sigma_{t,XX}$), maximum compressive and tensile stresses in the Y-direction ($\sigma_{c,YY}$ and $\sigma_{t,YY}$) and the total displacement of probe 52 at the top of the curve ($u_{XY,P52}$). The mean compressive strength of concrete in strength class C35/45 according to Eurocode 2 (EN 1992-1-1, 2004) is $f_{cm} = 43MPa$ and the mean tensile strength is $f_{ctm} = 3.2MPa$. It can be seen that none of the maximum compressive stresses (σ_c, shown as negative values) exceeds the compressive strength of the concrete, while for W6 and W7, the maximum tensile stresses (σ_t, shown as positive values) in the Y-direction exceed the tensile strength of the concrete for both the unsupported and supported crownwall. There is a significant increase of 210-280% in both compressive and tensile stresses between W5 and W6 for both crownwalls. At the same time, the increase in stresses is about 30-40% between W6 and W7 for both crownwalls. This is in correlation with the increase in the wave load between the wave states, as the increase in maximum total force (see table 3.3) between W5 and W6 is much larger than the increase in maximum total force between W6 and W7.

When the results of the unsupported and supported crownwalls are compared, it can be seen that in the X-direction, the compressive stresses increase by 70-75% while the tensile stresses stay the same or reduce by about 15% when the crownwall is supported by an additional wall. For the Y-direction, the compressive stresses increase by about 55-60% while the tensile stresses stay the same or reduce by 15%. The effects of the additional supporting wall are therefore greater on the compressive stresses than on the tensile stresses and greater in the X-direction than Y-direction. The additional supporting wall acts as a support in the X-direction which explains why the compressive stresses are more affected by its presence. The reduction in tensile stresses when the supporting wall is added might be explained by the bending moment reduction mentioned at the beginning of this chapter, which also causes the decrease in displacements.

Figures 3.17 and 3.18 show contour plots of the stress distribution in X- and Y-direction in the vertical part of the crownwall and the front part of the slab at the moment of maximum tensile stresses, as well as the pressure distribution and the location of the total force at that moment. The maximum stresses occur simultaneously as the maximum pressure and maximum total force. For W7, as mentioned in chapter 3.1.2, the point of application of the total force of the largest wave is just above the centre of the curve. Only the contour plots for W7 are presented here, but the contour plots for all wave states are presented in appendix B.

Table 3.6: Linear analysis results: maximum compressive (σ_c) and tensile (σ_t) stresses in global X- and Y-directions in the unsupported and supported crownwalls, for each wave state, and the total displacement of point 52 ($u_{XY,P52}$).

Crownwall	Wave state	H [m]	T [s]	$\sigma_{c,XX}$ [MPa]	$\sigma_{t,XX}$ [MPa]	$\sigma_{c,YY}$ [MPa]	$\sigma_{t,YY}$ [MPa]	$u_{XY,P52}$ [mm]
Unsupported	W5	5	8	-0.98	0.31	-1.23	1.33	0.61
	W6	6	8	-3.05	1.18	-3.85	5.04	2.18
	W7	7	11	-3.89	1.61	-4.99	7.20	3.05
Supported	W5	5	8	-1.64	0.33	-1.90	1.34	0.40
	W6	6	8	-5.14	1.03	-5.93	4.56	1.40
	W7	7	11	-6.85	1.39	-8.06	6.50	2.03

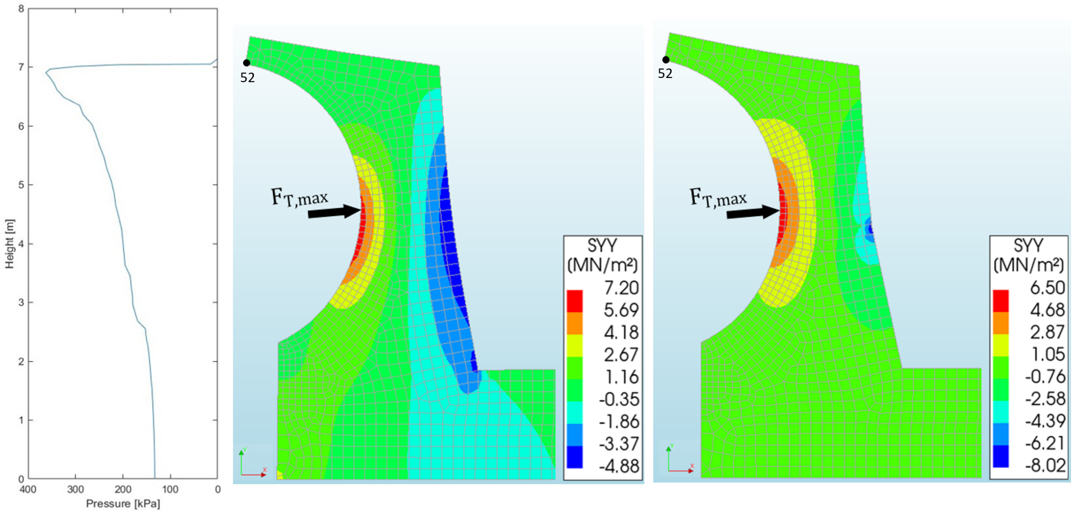

Figure 3.17: Stresses in Y-direction at the moment of maximum tensile stresses, the pressure distribution and total force at that moment. Unsupported crownwall to the left and supported crownwall to the right.

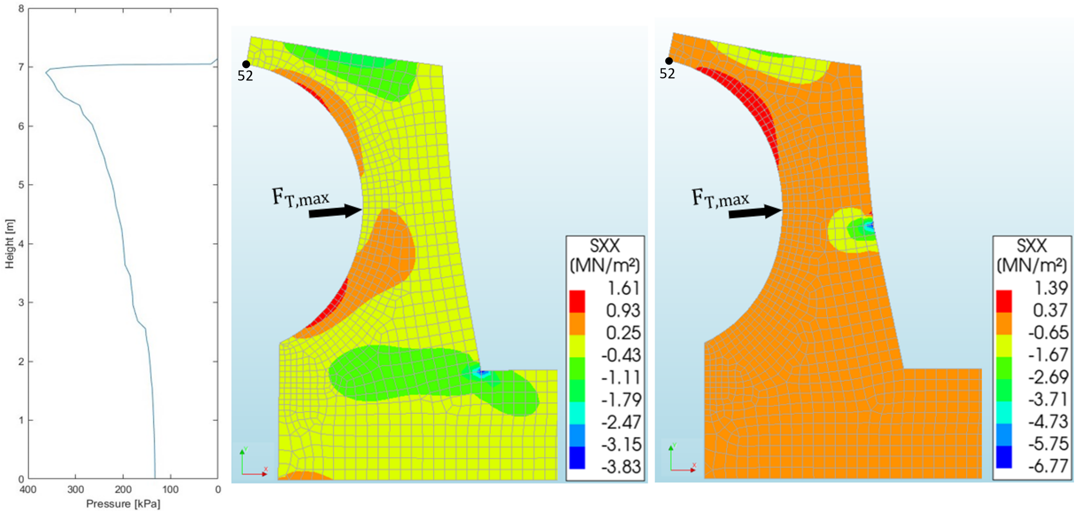

Figure 3.18: Stresses in X-direction at the moment of maximum tensile stresses, the pressure distribution and total force at that moment. Unsupported crownwall to the left and supported crownwall to the right.

The maximum tensile stresses (shown in red in figure 3.17) in Y-direction are located in the centre of the curve of both crownwalls and as they exceed the tensile strength of the concrete for W6 and W7, cracks are expected to form at that location. For the unsupported crownwall, the back side of the crownwall is all in compression in the Y-direction and the maximum compressive stresses (shown in blue) are located just above the re-entrant corner of the wall. In the X-direction (figure 3.18), the maximum tensile stresses are located in the bottom half of the curve, while the maximum compressive stresses are in the re-entrant corner. The localized maximum compressive stresses that can be seen in the re-entrant corner of the unsupported crownwall in the X-direction and just above the added supporting wall of the supported crownwall in bot X- and Y-directions are so-called *singularities*. That means that the stresses at these locations will not converge to a finite value and if the mesh size is reduced (h-refinement) or the mesh order increased (p-refinement), the stresses will increase. However, the compressive stresses are still far from the maximum compressive strength of the concrete and are therefore not of great concern. For the supported crownwall, the maximum tensile stresses in the X-direction are located in the top half of the curve for W7, opposite to the unsupported crownwall, but for W5 and W6, they are a singularity located directly above the maximum compressive stresses above the added supporting wall.

3.3.3. Nonlinear analysis

Nonlinear analysis is performed to analyse the cracking of the concrete structures, for cases where the tensile stresses exceed the concrete's tensile strength. That occurs for wave states 6 and 7, both the unsupported and supported crownwall. These cases will be referred to as cases W6-U, W6-S, W7-U and W7-S, for simplicity, where U represents the unsupported crownwall and S the supported crownwall.

To reduce computational time, only the largest waves of W6 and W7 are applied to the models in the nonlinear analysis. The time series of the total force of these two waves are shown in figure 3.19, W6 to the left and W7 to the right. As discussed in chapter 3.1.2, the maximum total force of W6 is 1420 kN with a point of application just below the centre of the curve of the crownwall and the maximum total force of W7 is 1890 kN with a point of application just above the centre of the curve. The pressure distribution at the moment of the maximum total forces of these two waves are very different, as has been discussed in chapter 3.1.1 and can be seen in figure 3.1. The maximum pressure of the largest wave of W6 is 220 kPa at probe 38 (just above the centre of the curve), while the maximum pressure of the largest wave of W7 is 360 kPa at probe 48 (at the top of the curve).

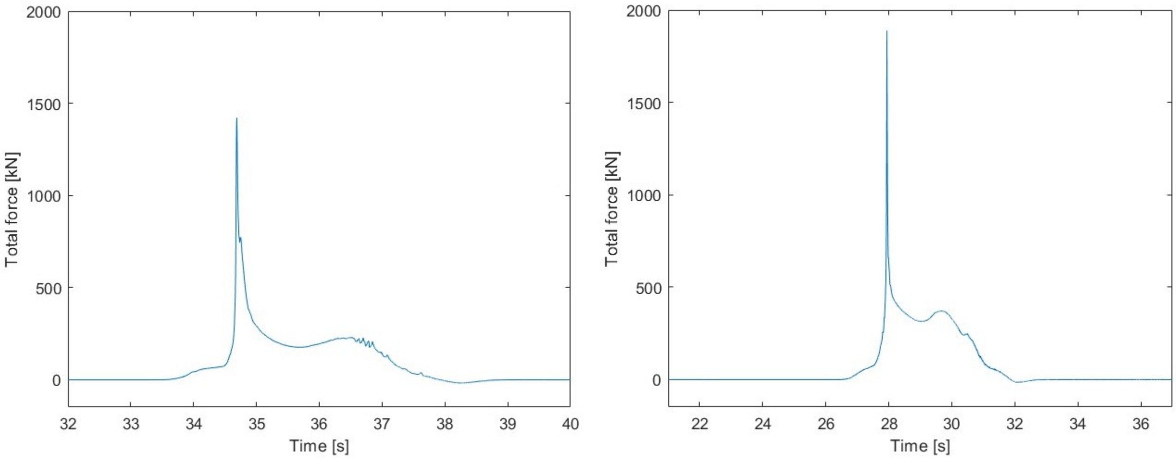

(a) W6 ($H = 6m, T = 8s$). **(b)** W7 ($H = 7m, T = 11s$).

Figure 3.19: Time series of the total force of the largest wave of W6 and W7 that are applied to the nonlinear models in Diana FEA.

Figure 3.20 shows the wave pressure-time series of W7 and the resulting time series of stresses in the Y-direction at the centre of the curve of the unsupported crownwall, case W7-U, where the maximum tensile stresses occur. The dark blue line shows the pressure-time series at the centre of the curve, the light blue line indicates the pressure-time series at the top of the curve, the yellow line indicates the stress-time series of the linear analysis and the orange line indicates the stress-time series of the nonlinear analysis. The black dashed line indicates the tensile strength of the concrete, $f_{ctm} = 3.2MPa$. It can be seen that shortly after the wave reaches the centre of the curve, at time t=27.77s, the compressive stresses reduce and when the wave has reached the top of the curve, at time t=27.87s, the stresses go from being compressive (negative) to being tensile (positive). The linear and nonlinear analyses result in equal stresses until the tensile stresses exceed the tensile strength of the concrete, at time t=27.93s. Then cracks form in the nonlinear model and the tensile stresses sharply reduce. The tensile stresses increase slightly at the moment of maximum pressure, at time t=27.94s, before sharply decreasing again. In the linear model, the stresses keep increasing and reach a maximum tensile stress of 7.20 MPa at the moment of max pressure, then vibrate and damp down. The same behaviour can be seen in the results of the other nonlinear models, the supported crownwall under the wave load of W7 (W7-S) and both crownwalls under the wave load of W6 (W6-U and W6-S).

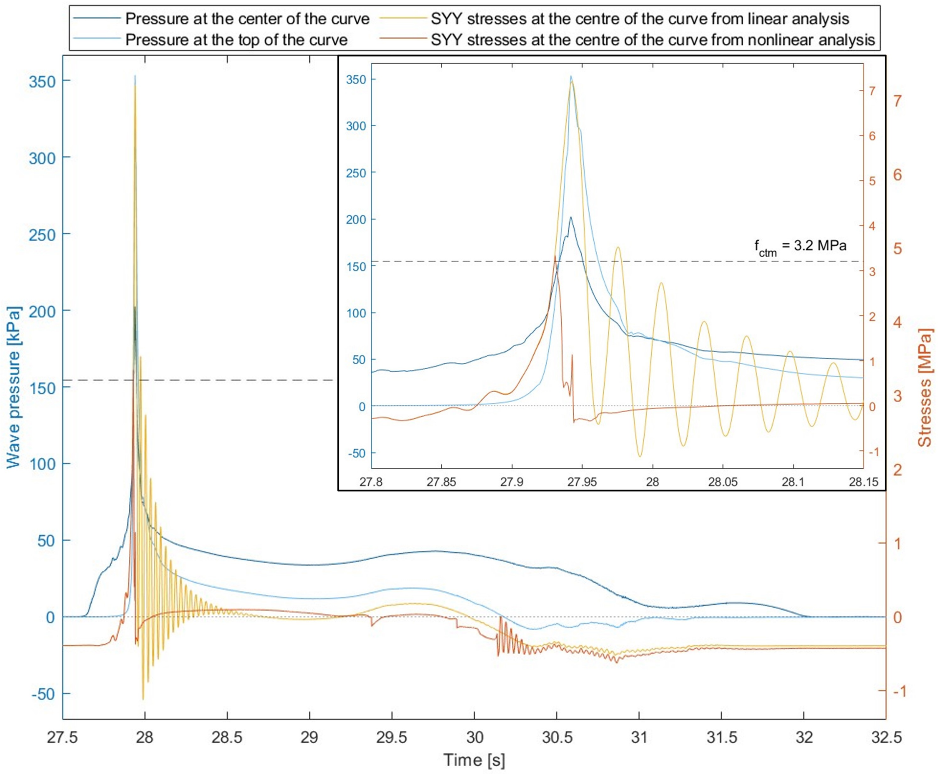

Figure 3.20: On the left axis in blue: wave pressure of W7. On the right axis in orange and yellow: resulting stresses (in the Y-direction) of the unsupported crownwall, case W7-U, in the centre of the curve where maximum tensile stresses occur.

Force-displacement graphs are presented in figure 3.21, where the total force of the wave load is on the y-axis and the total displacement of probe 52 at the top of the curve of the crownwall is on the x-axis (see figures 3.23i-3.23l). The two figures on the left are the results of the linear analysis, for W6 and W7 and both crownwalls, and the figures on the right are the results of the nonlinear analysis. For both the linear and nonlinear results, the displacement of probe 52 is zero until the force has reached about 350 kN, which is the moment the wave crest has reached the centre of the curve. This could also be seen in figure 3.15 where it was shown that the top of the crownwall did not start deflecting until the wave had reached the centre of the curve. For the linear analysis, the crownwalls deform elastically as the displacements increase when the force increases and when the force decreases, the wall vibrates and the displacements eventually return to the initial value.

The slope of the force-displacement graph indicates the stiffness of the structure, as it is defined as the change in force over the change in displacement. It is known from the eigenvalue analysis that the supported crownwall is stiffer than the unsupported crownwall. This can also be seen from all four force-displacement graphs, as the initial slope of the force-displacement graph of the supported crownwall (dark orange line) is steeper than the slope of the unsupported crownwall. The area under the force-displacement graphs indicates the energy absorbed by the structure from the wave force as it deforms. The results of the linear analysis show that there is more energy absorbed by the unsupported crownwall than the supported crownwall and more energy exerted on the structures by W7 than W6.

In the nonlinear model, the displacements also increase linearly with the increasing force, but due to the opening of cracks, the displacements keep increasing even though the force is reducing. For W6, figure 3.21b, the cracks open at the moment of the maximum total force. However, for W7, figure 3.21d, the cracks open before the maximum force is reached. Therefore, there is a sudden increase in the force-displacement graphs for W7 at the moment the cracks open. When the total force is down to 350 kN, the displacements reach maximum and start to reduce again. Eventually, they return to their initial value. There is therefore no permanent displacement of the top part of the crownwall above the cracked cross-section. For W6, when the total force is around 750 kN and the displacements around 10-15 mm, there is an increase in the force that can also be observed in figure 3.19a, which creates a hump in the force-displacement graph. Similarly, for W7, when the displacements are around 20-25 mm, there is a sharp decrease in the force which creates a dent in the force-displacement graph. The loops in the force-displacement graphs of W7 are due to the maximum quasi-static force. As shown in figure 3.19b, the force reaches a maximum quasi-static value of about 370 kN and due to that the displacements slightly increase again.

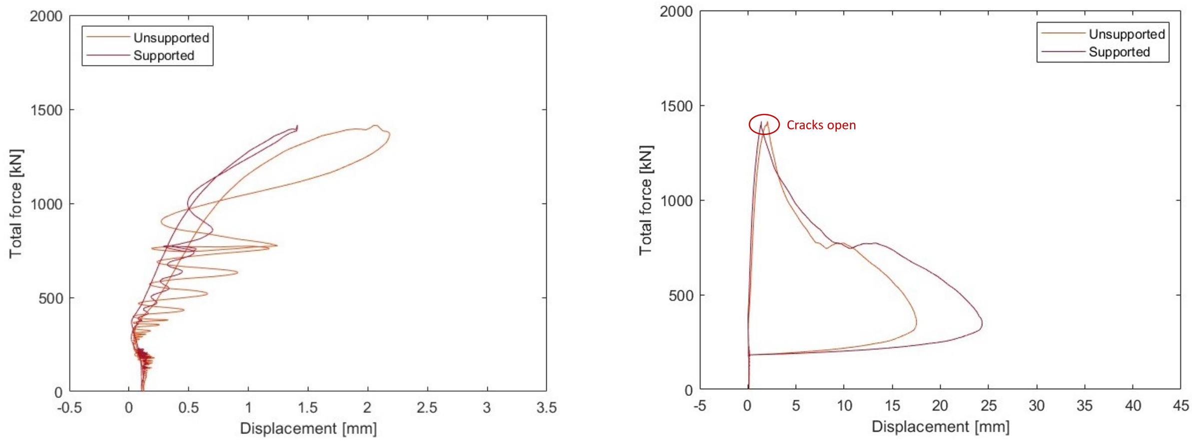

(a) W6 linear analysis.

(b) W6 nonlinear analysis.

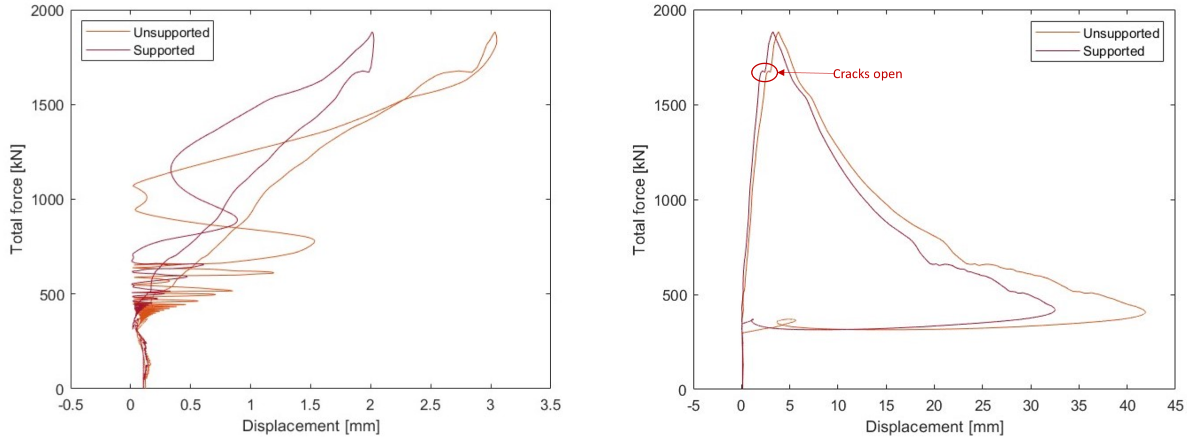

(c) W7 linear analysis.

(d) W7 nonlinear analysis.

Figure 3.21: Force-displacement diagrams for probe 52 at the top of the curve of the crownwall. To the left are the results of the linear analysis and to the right are the results of the nonlinear analysis. The results of the unsupported crownwall are shown in light orange and the results of the supported crownwall are in dark orange.

In figure 3.22 the resulting maximum crack widths in the Y-direction and the total displacement of probe 52 are presented in time, of both crownwalls for W6 (figure 3.22a) and W7 (figure 3.22b). The pressure-time series of the largest waves of W6 and W7 are again presented in blue in the same way as in figure 3.20. The crack widths and displacements are shown in green and orange respectively, where the results of the unsupported wall (cases W6-U and W7-U) are shown in light green/orange and the results of the supported wall (cases W6-S and W7-S) in dark green/orange. The crack width contour plots at three different moments in time are presented in figure 3.23. These moments are A: opening of cracks, B: maximum crack widths and C: closing of cracks in the front. The displacement contour plot at moment B is also presented as well as the location of the total force at each moment in time. These moments in time are also marked in figure 3.22 with black dots and the allocating letter. The crack widths shown in figure 3.22 are the sum of the crack widths at all nodes with positive crack widths in the front face of the crownwalls. For this reason, the maximum crack widths, at time B, in figure 3.22 show larger values than in figure 3.23. For W6, the maximum total crack widths are 22 mm and 29 mm for the unsupported and supported walls, respectively, and for W7 they are 48 mm and 38 mm respectively.

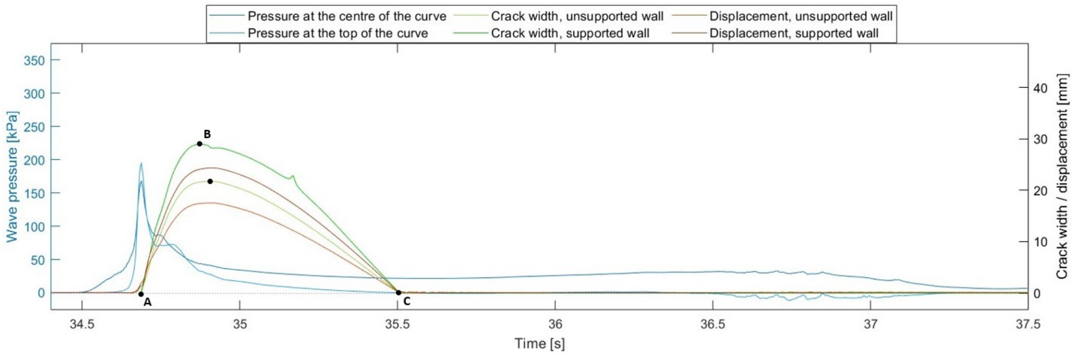

(a) W6 ($H = 6m$, $T = 8s$).

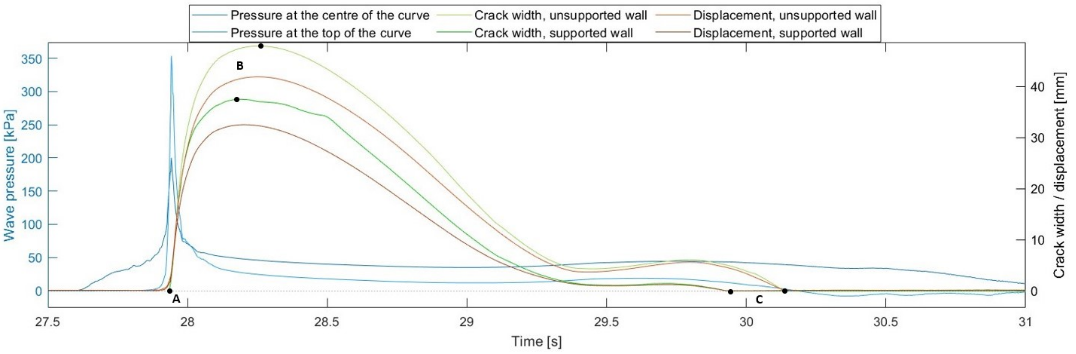

(b) W7 ($H = 7m$, $T = 11s$).

Figure 3.22: On the left axis in blue: wave pressure of W6 and W7. On the right axis in orange: resulting displacement of probe 52 of both crownwalls. On the right axis in green: resulting crack widths in the front face of the crownwalls, where maximum cracks occur.

In figure 3.23, each row of figures represents a moment in time (A, B or C) and each column represents the load case and crownwall type (W6-U, W6-S, W7-U or W7-S). At time A, when cracks start to open in the front face of the crownwalls (see figures 3.23a to 3.23d), the wave pressure of W6 has exactly reached maximum, but for W7 the wave pressure is still increasing, as discussed before. So, when the crownwalls are subjected to the maximum pressure of W7, the crack widths in the front face of the crownwalls are already up to 3 mm. As suspected, the supported crownwall starts to crack at the location where the added support wall ends at probe 35, while the initial cracks of the unsupported crownwall are more widely spread around the centre of the curve at probes 31-34. The cracks then propagate through the whole cross-section of the crownwalls, all the way to the backside.

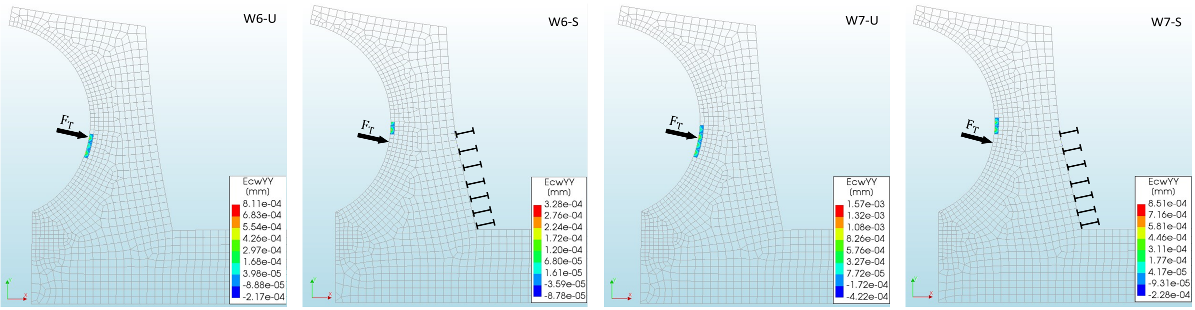

(a) W6, time A: cracks in unsupported wall

(b) W6, time A: cracks in supported wall

(c) W7, time A: cracks in unsupported wall

(d) W7, time A: cracks in supported wall

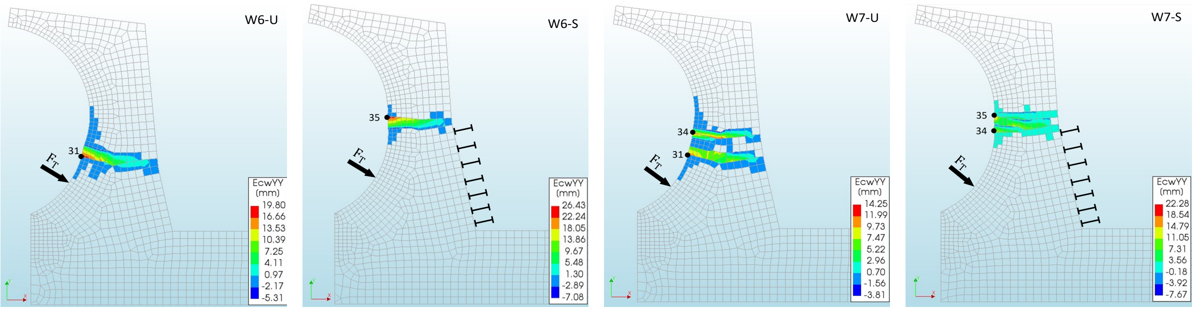

(e) W6, time B: cracks in unsupported wall

(f) W6, time B: cracks in supported wall

(g) W7, time B: cracks in unsupported wall

(h) W7, time B: cracks in supported wall

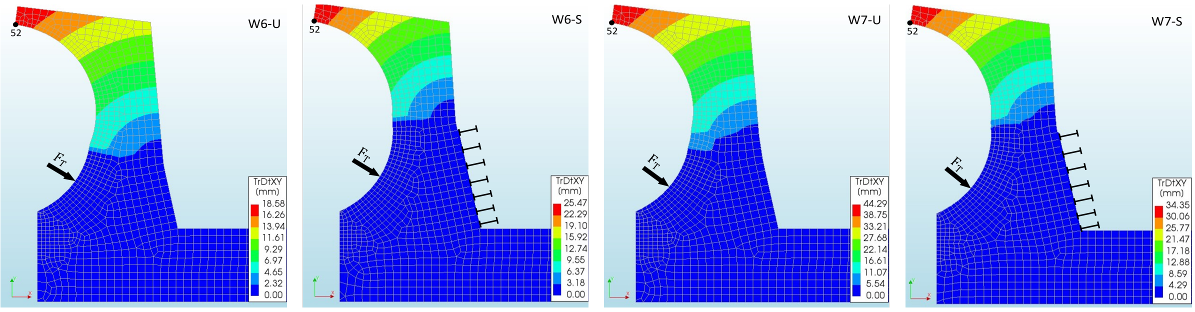

(i) W6, time B: displacements of unsupported wall

(j) W6, time B: displacements of supported wall

(k) W7, time B: displacements of unsupported wall

(l) W7, time B: displacements of supported wall

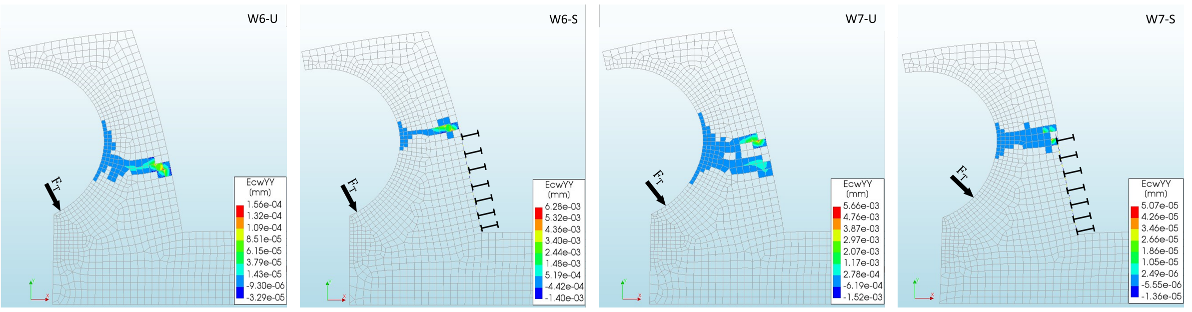

(m) W6, time C: cracks in unsupported wall

(n) W6, time C: cracks in supported wall

(o) W7, time C: cracks in unsupported wall

(p) W7, time C: cracks in supported wall

Figure 3.23: Development of cracks in the unsupported and supported crownwalls for W6 and W7. Time A is the moment cracking starts, time B is the moment of maximum cracking and time C is the moment that the cracks in the front of the wall close again and cracks in the front open. The displacement contour plots at the moment of maximum cracking (time B) are also shown.

It can be seen from figure 3.22 that for cases W6-S and W7-S, the crownwall reaches maximum crack width (point B on the dark green line) sooner than the unsupported wall (point B on the light green line). The explanation for this very slight difference in the response of the crownwalls is likely the fact that, as discussed in chapter 3.3.2, the whole vertical part of the unsupported crownwall can deflect while only the top part of the supported crownwall is free and therefore the response is slightly delayed for the unsupported crownwall. Another thing to take into account regarding this is that cracks are more widespread in the unsupported wall than in the supported wall, as can be seen in figure 3.23, which may also cause the unsupported crownwall to reach the maximum total crack width and displacement a little later.

When comparing the response of the crownwalls to the two wave states in figure 3.22, it can be noticed that for W6 the supported crownwall (case W6-S) shows larger total crack width and displacements, while for W7 it is the unsupported crownwall (case W7-U). This can also be seen in the force-displacement graphs in figure 3.21. The reason for this can be found in the location of the cracks. By looking at figures 3.23e and 3.23f it can be seen that the crack in the unsupported crownwall is located at probe 31 while the crack in the supported crownwall is much higher at probe 35. Therefore, the mass above the cracked cross-section is 24% larger for the unsupported crownwall and the cross-section at the location of the crack is 15% wider, which results in smaller crack widths and displacements. For W7, the crownwalls crack at similar locations, figures 3.23g and 3.23h. Two cracks are formed in both crownwalls, at probes 34 and 31 for the unsupported crownwall and probes 35 and 34 for the supported crownwall. The masses above the cracked area are therefore almost equal. Still, the unsupported crownwall being less stiff results in larger displacements and larger total crack width in the front face.

For W6, the cracks in the front face close about the same time as the wave pressure on the top part of the curve reduces to zero, for both case W6-U and W6-S. The cracks do not open again even though the pressure is still acting on the centre of the curve. For W7, the crack width reduces after reaching a maximum and then increases again when the pressure reaches maximum quasi-static pressure. The cracks in the front face of both crownwalls then close about the same time as the pressure at the top of the curve reduces to zero, as with W6, although the cracks in the supported wall close slightly earlier than the cracks in the unsupported wall. The total opening time of the cracks for W6 is 0.8 s and for W7 it is 2-2.2 s.

When the cracks in the front of the crownwalls have closed, the walls start to vibrate. This vibration can be seen in figure 3.20 of the stress-time series of the unsupported crownwall under wave load from W7, where the stress-time series starts to vibrate at about t=30.2 s, which is the time the cracks in the front close. The frequency of the vibrations are about 0.5-2 Hz lower than the eigenfrequency of the first eigenmodes of the two crownwalls meaning that the vibrations of the crownwalls are a bit slower in the cracked state than before cracking. This is because of the small cracks that are open in the back of the crownwalls. They cause a reduction in the structure's stiffness, but as the crack widths are very small, the reduction is also small.

4

Comparison to a recurved crownwall

The results of the analysis of the wave load acting on the fully curved crownwall and the results of the dynamic structural analysis are now compared to former studies on recurved crownwalls. Castellino et al. (2018a, 2018b) and Martinelli et al. (2018) have studied the wave load acting on recurved crownwalls of vertical breakwaters, both with numerical and physical studies. The CFD-generated pressure-time series of wave states 5, 6 and 7 for the recurved crownwall, produced and analysed by Castellino et al. (2018a), are used for the comparison of the wave load on the two crownwalls. The analysis of the wave load on the fully curved crownwall indicates that the C-CI phenomenon (Castellino et al., 2018a) is observed for W6 and W7 but it is not as evident for W5. The wave load acting on the fully curved crownwall can now be compared to the wave load, by the same three wave states, acting on the recurved crownwall. Figure 4.1 shows the pressure distribution at the moment of maximum total force for the largest waves acting on the fully curved crownwall and the recurved crownwall. The fully curved crownwall is shown in grey and the pressure distribution is in black. The recurved crownwall is shown in blue (transparent) and the pressure distribution is in blue. For the fully curved crownwall, the largest waves are wave 3 of W5, wave 3 of W6 and wave 2 of W7. For the recurved crownwall, the largest waves are wave 2 of W5, wave 4 of W6 and wave 2 of W7. It can be seen that at the moment of the maximum total force, the pressure along the height of the crownwall is in general larger for the fully curved crownwall than for the recurved crownwall. The curved face ”catches” the incoming wave and the weight of the water in the curve adds pressure to the lower part of the curve. The wave also gains momentum as it travels up the curve of the fully curved crownwall, which it does not gain at the vertical part of the recurved crownwall where it can be seen that the pressure decreases with height.

The localized maximum pressure is defined as the maximum pressure value along the height of the crownwall at the moment of the maximum total force. For W5, the localized maximum pressure is larger for the recurved crownwall than for the fully curved crownwall even though it is the opposite for pressure acting on the rest of the crownwall. The C-CI phenomenon is stronger for the recurved crownwall, as the pressure increase at the top of the crownwall is larger than for the fully curved crownwall. In the study of Castellino et al. (2018a), where the wave pressure on the recurved crownwall was compared to the wave pressure on a vertical wall, it was found that the threshold value for the C-CI phenomenon to occur is a relative freeboard $R_c/H = 1.62$ and for waves with $R_c/H \leq 1.3$ (W5) the phenomenon is evident. For the fully curved crownwall, these threshold values of the relative freeboard, for the C-CI phenomenon to occur and be evident, seem to be lower. That means that for recurved and fully curved crownwalls with the same freeboard, R_c, a larger wave height, H, is needed for the C-CI phenomenon to occur at the fully curved crownwall than the recurved crownwall. This is due to the fact that the confinement of the crest of the wave is greater for the recurved crownwall as the wave is free to travel up the crownwall until it reaches the bullnose at the very top. For the fully curved crownwall, the wave has to travel a longer distance and the shape of the curve softens the pressure increase at the top.

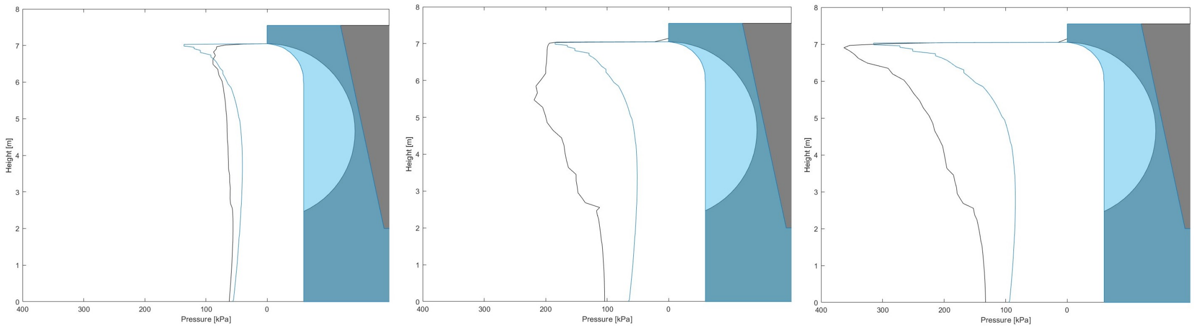

(a) W5 ($H = 5m$, $T = 8s$).

(b) W6 ($H = 6m$, $T = 8s$).

(c) W7 ($H = 7m$, $T = 11s$).

Figure 4.1: Pressure distribution along the wall height for the fully curved and recurved crownwalls at the moment of the maximum total force. Pressure on the fully curved crownwall in black and the recurved crownwall in blue.

Figure 4.2 shows the total force, vertical force, horizontal force and maximum pressure of the fully curved (FC) crownwall normalized with the values of the recurved crownwall (R):

$$F_{ratio} = F_{FC}/F_R$$

$$P_{ratio} = P_{FC}/P_R$$

The normalized total force is shown as a solid black line with asterisk markers and the normalized pressure as a solid black line with x markers. The normalized horizontal and vertical forces are shown as dashed black lines with circle and diamond markers, respectively. Values above the blue dashed line indicate that the force or pressure acting on the fully curved crownwall is larger than on the recurved crownwall, and the opposite for values below the blue dashed line. The figure clearly shows that the difference in the total force is the smallest for W5, with $F_{T,ratio} = 1.35$, and largest for W6, with $F_{T,ratio} = 2.5$. This is in accordance with the pressure distribution in figure 4.1, as the smallest difference is in the pressure distribution of W5 but the largest difference is in the pressure distribution of W6. For W7 the difference in the maximum total force is $F_{T,ratio} = 2.05$. However, when the average of the maximum total force of all waves in each wave state is considered, the difference between the fully curved and recurved crownwalls is less. For W5, $F_{T,ave,ratio} = 1$, for W6 $F_{T,ave,ratio} = 1.6$ and for W7 $F_{T,ave,ratio} = 1.7$.

The difference in the localized maximum pressure values is much less than the difference in the total force for W6 and W7 but for W5 the difference is the same, except the maximum pressure acting on the fully curved crownwall, is 35% smaller than the maximum pressure acting on the recurved crownwall. For the maximum pressure of W6 $P_{max,ratio} = 1.08$ and for W7 it is $P_{max,ratio} = 1.14$. For the average maximum pressure of all waves in each wave state, the difference between the fully curved and recurved crownwalls is slightly larger, opposite to the average maximum force. For W5, $P_{max,ave,ratio} = 0.5$ and for W6 and W7 $P_{max,ave,ratio} = 1.2$. So, on average, the maximum pressure of waves in W5 is two times smaller for the fully curved crownwall while the maximum force is on average equal to the recurved crownwall. For W6 and W7, the maximum pressure of each wave is on average 20% larger for the fully curved crownwall while the maximum force of each wave is on average 60-70% larger. However, for the structural analysis of the crownwalls, the maximum value of the wave force is what matters as that results in the largest stresses in the structure.

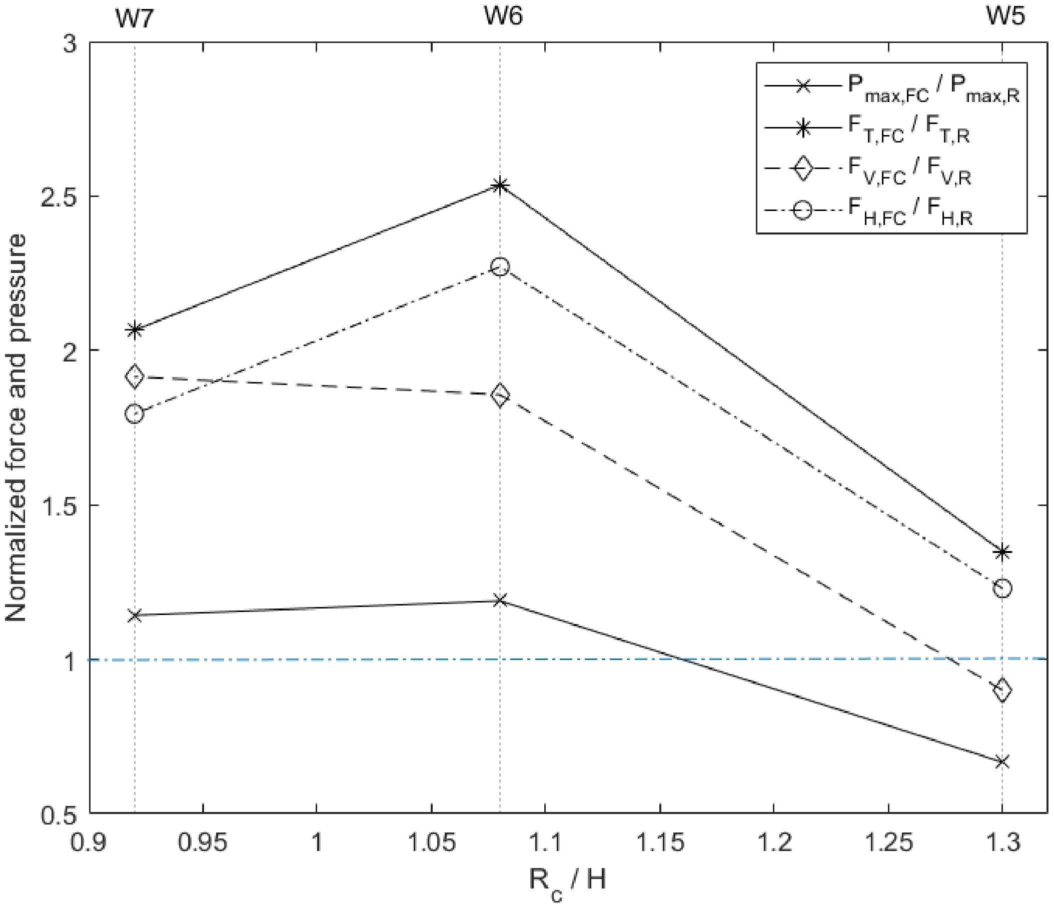

Figure 4.2: The wave load acting on the fully curved crownwall normalized with the wave load acting on the recurved crownwall as a function of freeboard over wave height.

For the horizontal component of the total force, the normalized values follow the same trend as the normalized total force, where the smallest difference between the horizontal force acting on the fully curved and recurved crownwalls is for W5 and the largest difference for W6. But for the vertical component of the total force, the distribution of the normalized values resembles the distribution of the normalized maximum pressure values. This was expected, as the vertical component only exists at the curved parts of the crownwall, so the pressure at the top of the curve, where the maximum pressure occurs, has high influence on the vertical force. For W5, where $P_{max,ratio} < 1$ also $F_{V,ratio} < 1$. The largest difference is for W7 where $F_{V,ratio} = 1.9$ and for that wave state $F_{V,ratio} > F_{H,ratio}$. This is also the wave state that has the strongest C-CI phenomenon for the fully curved crownwall.

Figure 4.3 shows the time series of the total force of the largest wave of each wave state acting on the fully curved (in black) and recurved (in blue) crownwalls. As the largest waves do not occur at the same time for both crownwalls, the time series of the recurved crownwall was moved a few seconds back or forth such that the maximum force would align in time with the maximum force of the fully curved crownwall. One apparent difference between the two time series, which can be seen for all wave states, is the change in slope of the fully curved force-time series as the force is increasing. As discussed in chapter 3.1.2, the force acting on the fully curved crownwall increases faster after the wave has reached the curve. For the recurved crownwall, the force increases steadily until the wave has reached the bullnose at the top of the crownwall and force becomes impulsive.

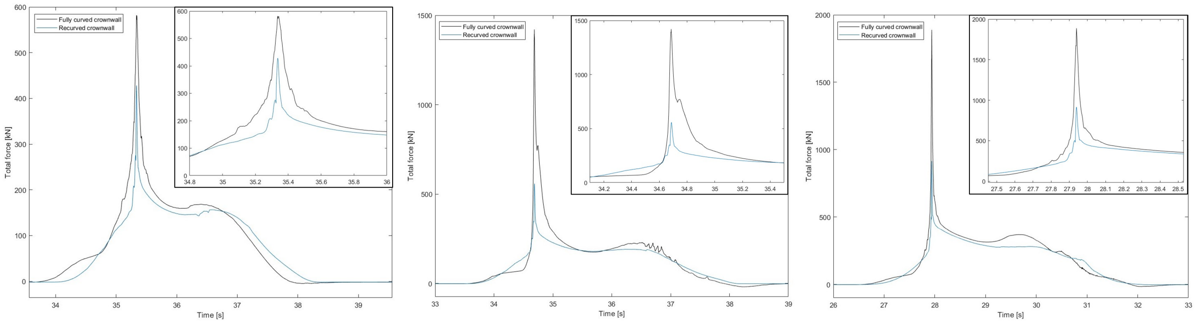

(a) W5 ($H = 5m$, $T = 8s$). **(b)** W6 ($H = 6m$, $T = 8s$). **(c)** W7 ($H = 7m$, $T = 11s$).

Figure 4.3: Time series of the total force of the largest wave of each wave state for the fully curved and recurved crownwalls.

Table 4.1 shows the maximum total force, the force impulse, the maximum pressure and the pressure impulse of the largest wave of each wave state for the fully curved and recurved crownwalls. All maximum force and pressure impacts were of an impulsive type according to the criterion given in table 3.1, that is, the maximum instantaneous force or pressure is over 2.5 times larger than the maximum quasi-static force or pressure. The pressure impulse was calculated for probe 47 on the fully curved crownwall and probe 70 on the recurved crownwall, see figure 4.4. These probes were chosen because most waves have the maximum pressure at these probes. However, one exception is the largest wave of W6 acting on the fully curved crownwall as it has the maximum pressure at probe 38. Therefore, the P_{max} and I_P values in table 4.1 are not at the same probe for that wave. As for the maximum force and pressure values, the difference in the force impulses between the two crownwalls is bigger than the difference in pressure impulses. It is interesting to see that even though the maximum pressure of W5 is larger for the recurved crownwall the pressure impulse is smaller. That is due to a longer impulse duration of the pressure impulses of the fully curved crownwall. The same can be seen in figures 4.3a-4.3c, where the force impulses of the fully curved crownwall have a longer duration.

Table 4.1: Wave load acting on the fully curved and recurved crownwalls and maximum tensile and compressive stresses: maximum total force $F_{T,max}$, force impulse I_F, maximum pressure P_{max}, pressure impulse I_P, maximum compressive (σ_c) and tensile (σ_t) stresses in X- and Y-direction.

Crownwall	Wave state	H [m]	T [s]	F_T [kN]	I_F [kNs]	P_{max} [kPa]	I_P [kPas]	$\sigma_{c,XX}$ [MPa]	$\sigma_{t,XX}$ [MPa]	$\sigma_{c,YY}$ [MPa]	$\sigma_{t,YY}$ [MPa]
Fully curved	W5	5	8	580	34	90	5.9	-1.64	0.33	-1.90	1.34
	W6	6	8	1420	81	220	4.7	-5.14	1.03	-5.93	4.56
	W7	7	11	1890	62	360	8.5	-6.85	1.39	-8.06	6.50
Recurved	W5	5	8	430	10	135	3.4	-	-	-	-
	W6	6	8	560	11	185	4.2	-2.14	0.58	-3.34	1.49
	W7	7	11	915	17	315	4.9	-5.22	0.72	-6.65	2.64

In their analysis of the recurved crownwall, Dermentzoglou et al. (2021) found that the pressure impulses of W6 and W7, at probe 70, were in the dynamic domain of the recurved crownwall, the same as was found for the fully curved crownwall. The dominant mode of the vertical part of the recurved crownwall was the first eigenmode with the eigenfrequency $f_{n1,R} = 56.6Hz$. The first eigenmode of the supported fully curved crownwall was also the dominant mode of the vertical part, but the eigenfrequency is $14Hz$ lower or $f_{n1,FC} = 42.6Hz$. This indicates that the recurved crownwall is a stiffer structure and that the natural period of the vibrations, T_n, is shorter. Because the pressure impulse durations of the recurved crownwall, $T_{d,R}$, are shorter than those of the fully curved crownwall, $T_{d,FC}$, the ratio between the impulse duration and natural period of the structures, for the largest waves of W6 and W7, is about the same for both structures: $T_d/T_n \approx 3-4$. As figure 4.5 shows, the modal shapes of the first eigenmodes of the structures are identical, where only the top of the crownwall above the additional supporting wall is deflecting.

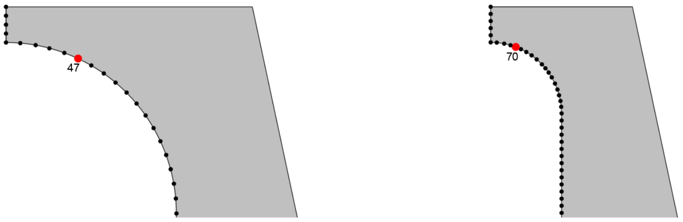

(a) Fully curved crownwall. **(b)** Recurved crownwall.

Figure 4.4: Top part of the crownwalls showing the probes where maximum pressure occurs for most waves. Pressure impulse (I_P) values in table 4.1 are calculated at these probes.

Table 4.1 also shows the results of the linear analysis of the *supported* fully curved crownwall and the results of the linear analysis of Dermentzoglou et al. (2021) on the recurved crownwall. Unfortunately, the results of the linear analysis of the recurved crownwall under the wave load of W5 are not available. However, a comparison of the results of W6 and W7 can give valuable insight on the effect of the shape of crownwalls on the dynamic response and failure. The stress distributions of stresses in X- and Y-direction for W7 of both the fully curved and recurved crownwalls are presented in figure 4.6. There it can be seen that in the X-direction, that the maximum compressive stresses (blue) are located just above the additional supporting wall for both structures. The maximum tensile stresses (red) are also located just above the additional supporting wall and both crownwalls have high tensile areas at the top of the curves. In Y-direction, maximum compressive stresses are again located just above the additional supporting wall and the maximum tensile stresses are located at the same height but in the front face of the crownwalls.

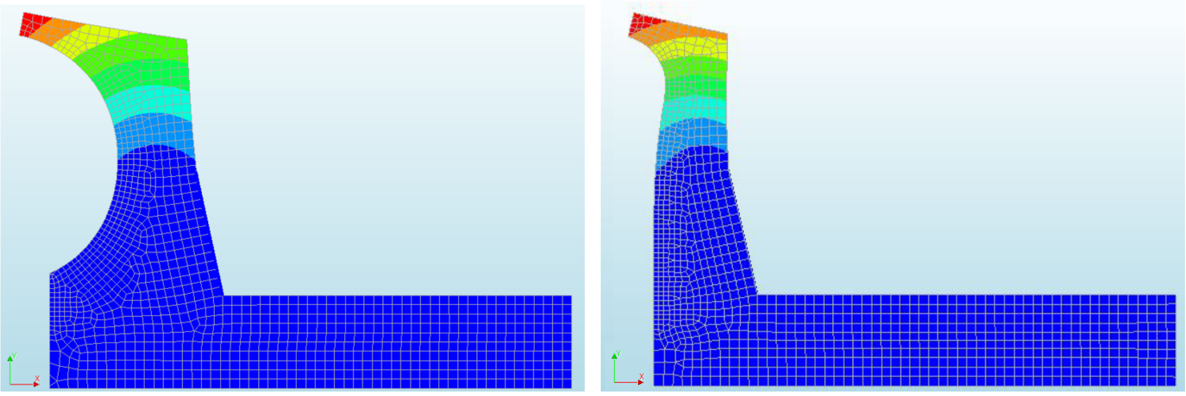

(a) First eigenmode of the supported fully curved crownwall with eigenfrequency $f_{n1,FC} = 42.6Hz$.

(b) First eigenmode of the recurved crownwall with eigenfrequency $f_{n1,R} = 56.6Hz$ (Dermentzoglou et al., 2021).

Figure 4.5: Modal shape of the first eigenmode of the two crownwalls.

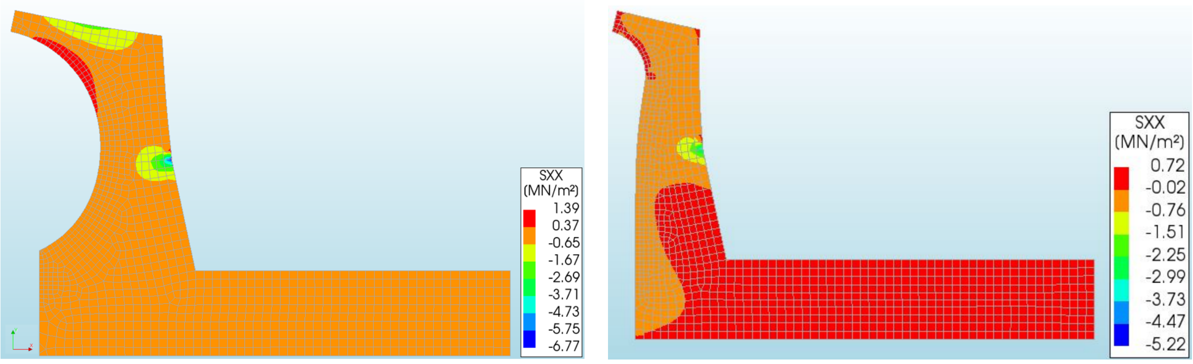

(a) Fully curved crownwall: stress distribution in X-direction.

(b) Recurved crownwall: stress distribution in X-direction (Dermentzoglou et al., 2021).

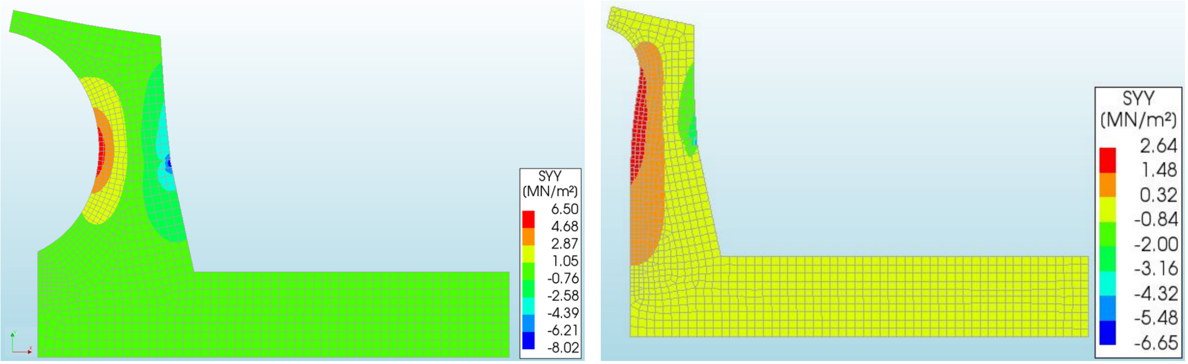

(c) Fully curved crownwall: stress distribution in Y-direction.

(d) Recurved crownwall: stress distribution in Y-direction (Dermentzoglou et al., 2021).

Figure 4.6: The stress distribution in X- and Y-direction at the moment of maximum stresses for W7.

It is evident from the results presented in table 4.1 and figure 4.6 that smaller stresses occur in the recurved crownwall than the fully curved crownwall. None of the maximum stresses that occur in the recurved crownwall exceed the compressive or tensile strength of the concrete, $f_{cm} = 43MPa$ and $f_{ctm} = 3.2MPa$ respectively. Similar to figure 4.2 for the wave load, figure 4.7 shows the maximum stresses of the fully curved crownwall normalized with the maximum stresses of the recurved crownwall for W6 and W7, as a function of R_c/H. Compressive stresses are shown in blue, tensile stresses are in red, the results of W6 are dashed lines with circle markers and the results of W7 are solid lines with diamond markers. The difference in maximum stresses is larger for W6 than W7, similar to the difference in total force, except for the tensile stresses in the X-direction. The maximum tensile stresses in the Y-direction of the fully curved crownwall are 3 and 2.5 times larger than those of the recurved crownwall, for W6 and W7 respectively, which is larger than the difference in the wave force (see figure 4.2). These are the most crucial stresses, as for the fully curved crownwall, they are larger than the tensile strength of the concrete.

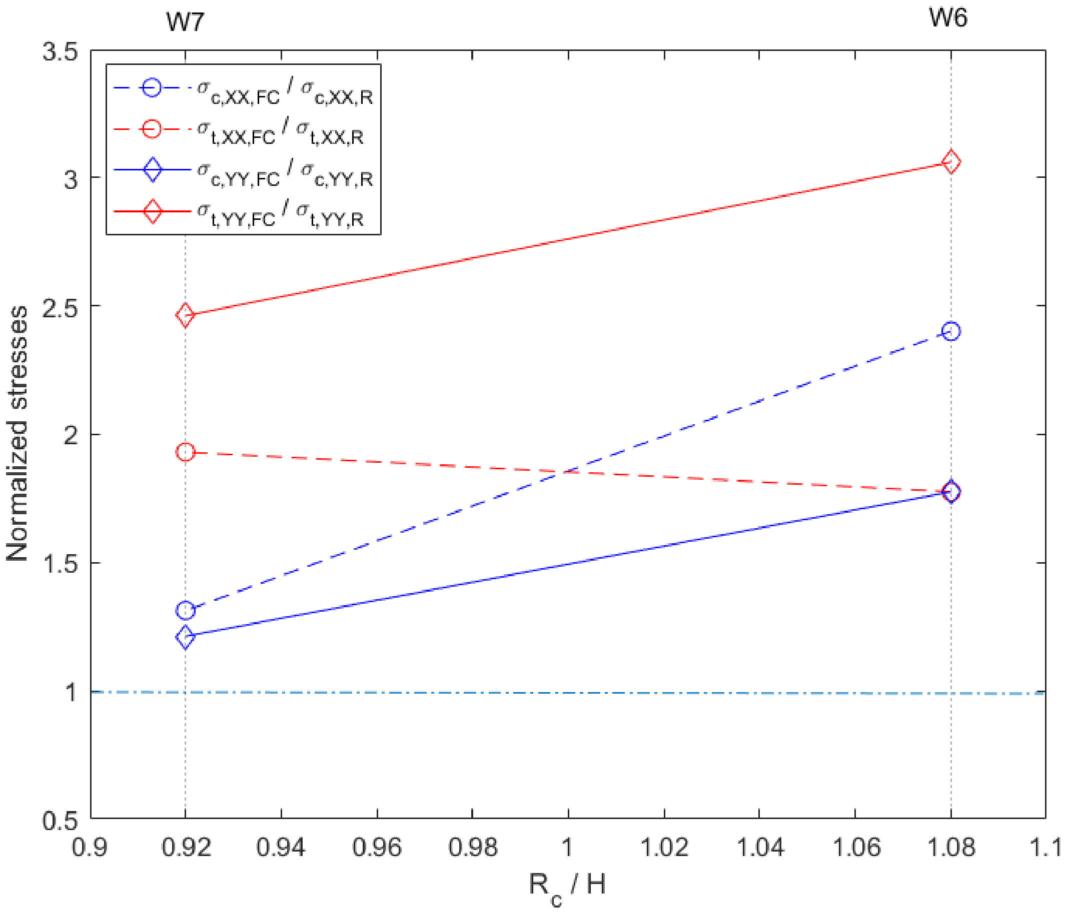

Figure 4.7: The maximum stresses of the fully curved crownwall normalized with the maximum stresses of the recurved crownwall as a function of freeboard over wave height.

To better understand the loading and structural response of the two different shapes of crownwalls, the loading on the top parts of the crownwalls is analysed further. Figure 4.9 shows the point of application of the horizontal ($F_{H,top}$) and vertical ($F_{V,top}$) wave forces acting on the crownwalls above the additional supporting wall at the moment of maximum total wave force. The figure also shows the centre of mass of the top part of the two crownwalls (W_{top}). The critical cross-section of the crownwalls is where the supporting wall ends, as it has been shown that at that location the largest tensile stresses occur (figures 4.6c-4.6d) and the fully curved crownwall cracks (figures 3.23f and 3.23h). Dermentzoglou et al. (2021) found that for a recurved crownwall made of concrete in strength class C25/30 under wave load of W7, cracks occur in that cross-section. The width of the critical cross-section is almost the same for both crownwalls, $b_{critical} = 1.7m$ and $b_{critical} = 1.6m$ for the fully curved and recurved crownwall respectively. As the crownwalls are fully supported below the critical cross-section, only the top part of the crownwalls, which are free to deflect, are considered here. To determine the vertical and horizontal forces, equations 4.1 and 4.2 were used. The pressure P at each probe i, at and above the critical cross-section, was multiplied by the area A surrounding the probe to obtain the total force acting on that specific part of the crownwall. Each total force was then split into its horizontal and vertical components by multiplying with the cosine or sinus of the angle φ, which is the orientation of each probe. The total horizontal and vertical forces are then simply the

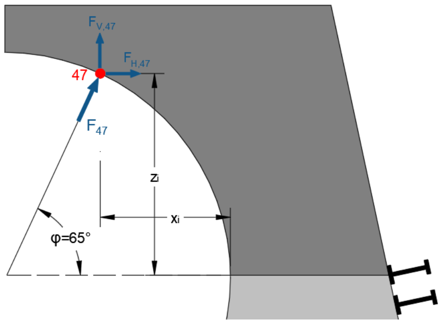

Figure 4.8: Calculation method for the horizontal and vertical forces.

sum of all the horizontal and vertical forces at each probe. To obtain the point of application of the forces, the weighted average of the forces is used as shown in equations 4.3 and 4.4. The method is visualized in figure 4.8 with probe 47 as an example, where all variables are presented. The vertical and horizontal wave forces are shown as blue arrows, the centre of gravity is shown as a black ”X” and the self-weight of the top of the crownwalls as a black arrow. The bending moment of each force is taken about the centre of the critical cross-section, shown as a red dot. The bending moment arms a_H, a_V and a_W are also shown in the figure, for the horizontal force, vertical force and self-weight, respectively.

$$F_{H,i} = \sum_{i=35}^{56} P_i A_i cos(\varphi_i) \tag{4.1}$$

$$F_{V,i} = \sum_{i=35}^{56} P_i A_i sin(\varphi_i) \tag{4.2}$$

$$z = \frac{\sum_{i=35}^{56} F_{H,i} z_i}{\sum_{i=35}^{56} F_{H,i}} \tag{4.3}$$

$$x = \frac{\sum_{i=35}^{56} F_{V,i} x_i}{\sum_{i=35}^{56} F_{V,i}} \tag{4.4}$$

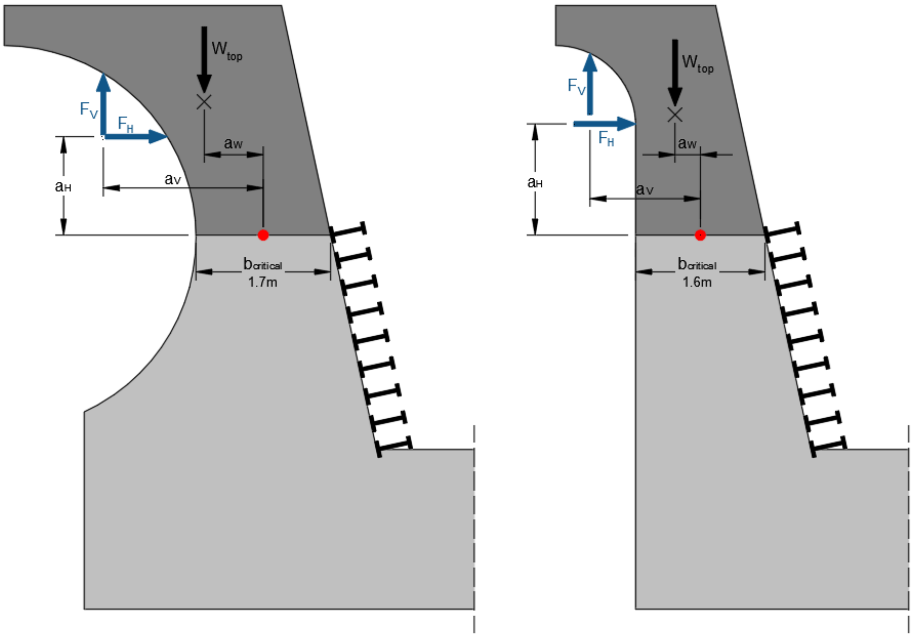

Figure 4.9: Fully curved (left) and recurved (right) crownwalls, the point of application of the horizontal ($F_{H,top}$) and vertical $F_{V,top}$ wave forces above the additional supporting wall at the moment of maximum total force and the centre of mass and self-weight (W_{top}) of the top part of the two crownwalls. The bending moment is taken about the centre point of the critical cross-section ($b_{critical}$).

Table 4.2 shows the results of the force and bending moment calculations. It can be seen that for the fully curved crownwall $F_{V,top}$ and $F_{H,top}$ are almost equal, as the curve is nearly a perfect quarter of a circle. But for the recurved crownwall, the horizontal force is larger, for all wave states, as a large part of the front of the crownwall is vertical. For the recurved crownwall, the bending moment arms of the vertical and horizontal wave forces are equally long, and as $F_{H,top} > F_{V,top}$ the horizontal wave force has a larger impact than the vertical wave force acting up under the bullnose. For the fully curved crownwall it is the opposite, as the vertical and horizontal forces are almost equal but $a_V > a_H$, so the vertical wave force has more impact. As figure 4.9 indicates, the self-weight of the top part of the fully curved crownwall is 60% larger than the top part of the recurved crownwall and the bending moment arm to the centre of mass, a_W, is 130% longer. This means that the fully curved crownwall has a larger bending moment to the left, created by the top mass, which works against the bending moment to the right, created by the wave load. The total vertical force is the result of the upwards-acting vertical wave force and the downwards-acting self-weight. It can be seen from the results in table 4.2 that the total vertical force, at the moment of the maximum total force, is acting upwards for both crownwalls and all wave states as $F_{V,top} > W_{top}$. This will also add to the tensile stresses in the whole cross-section.

Table 4.2: Loading of the top of the crownwalls, dark grey area in figure 4.9, above the critical cross-section. F_V, F_H: vertical and horizontal wave forces acting on the crownwalls above the critical cross-section. W_{top}: self-weight of the top parts. a_V, a_H and a_W: the bending moment arms of each force. M_V, M_H and M_W: the resulting bending moments. M_{tot}: total bending moment.

Crownwall	Wave state	$F_{V,top}$ [kN]	a_V [m]	M_V [kNm]	$F_{H,top}$ [kN]	a_H [m]	M_H [kNm]	W_{top} [kN]	a_W [m]	M_W [kNm]	M_{tot} [kNm]
Fully curved	W5	175	2	350	180	1.2	215	-145	0.7	-100	465
	W6	460		920	490		590				1410
	W7	695		1390	650		780				2070
Recurved	W5	100	1.4	140	160	1.4	225	-90	0.3	-30	335
	W6	140		195	220		310				475
	W7	235		330	370		520				820

Figure 4.10 visualizes the results presented in table 4.2. The figure shows $M_{ratio} = M_{FC}/M_R$, similar to figures 4.2 and 4.7, as a function of R_c/H. As mentioned above the difference in maximum tensile stresses in Y-direction between the two crownwalls was larger than the difference in the maximum total force. However, as can be seen from the figure, the difference in the total bending moment, M_{tot}, between the fully curved and recurved crownwalls is the same as the difference in the maximum tensile stresses for W6 and W7. This is because the total bending moment at the moment of the maximum total force is most influential on the stresses in the critical cross-section. The bending moment arm to the vertical wave force, a_V, is 43% longer for the fully curved crownwall than the recurved crownwall, while the bending moment arm to the horizontal wave force, a_H, is 25% shorter. The difference in $F_{V,top}$ is also larger than the difference in $F_{H,top}$, therefore the difference in M_V is larger than the difference in M_H.

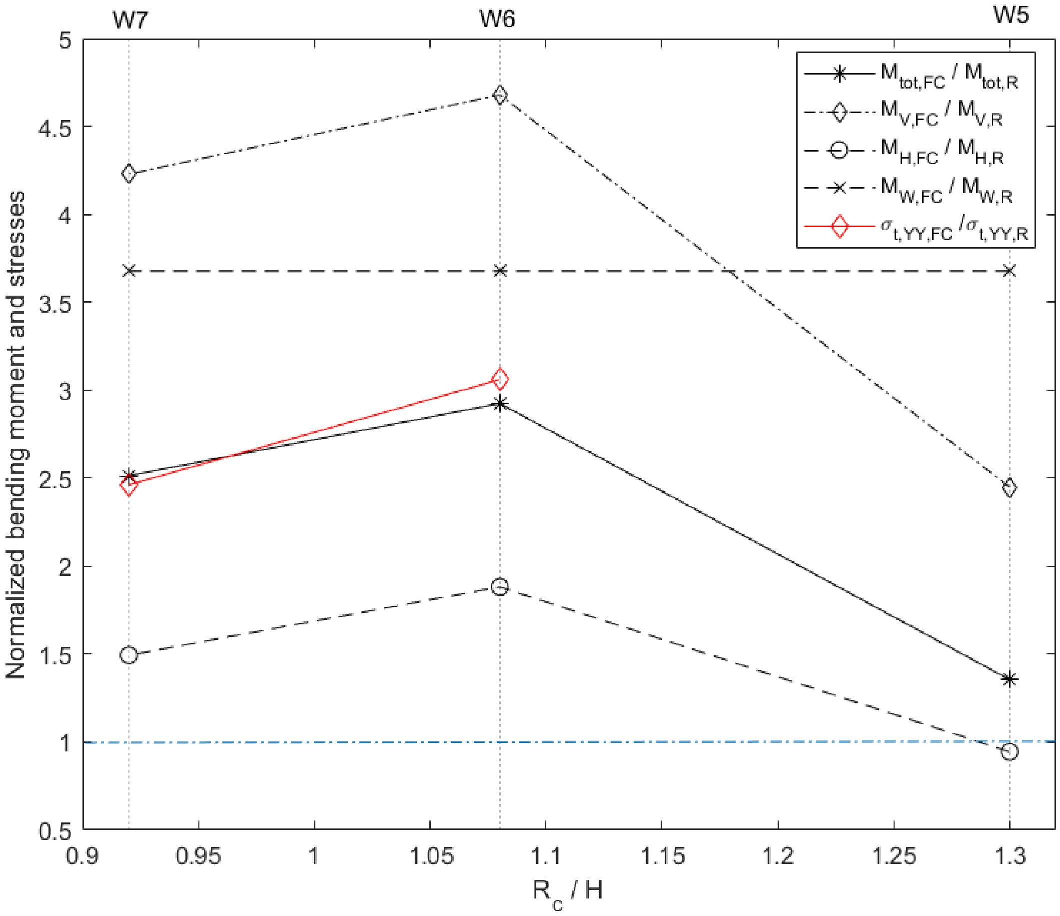

Figure 4.10: The maximum stresses of the fully curved crownwall normalized with the maximum stresses of the recurved crownwall as a function of freeboard over wave height.

5

Discussion

5.1. Failure modes of the fully curved crownwall

Figure 5.1 shows three possible failure mechanisms of the fully curved crownwall. Only one failure mode has been investigated in this study, structural failure. The other two failure modes are rigid body movements, sliding and overturning. These three failure mechanisms have occurred in vertical breakwater crownwalls, for example, the structural failure of the crownwalls in Civitavecchia Harbour, Italy (Castellino et al., 2018a), Ferrol Priorino Cape Harbour, Spain (Negro et al., 2018) and the port of the island of Alborán, Spain (Valdecantos et al., 2014), and the sliding and overturning of the crownwalls in the ports of Bermeo and Motril, Spain (Valdecantos et al., 2014; Negro et al., 2018). Figure 5.3 shows some of these failures.

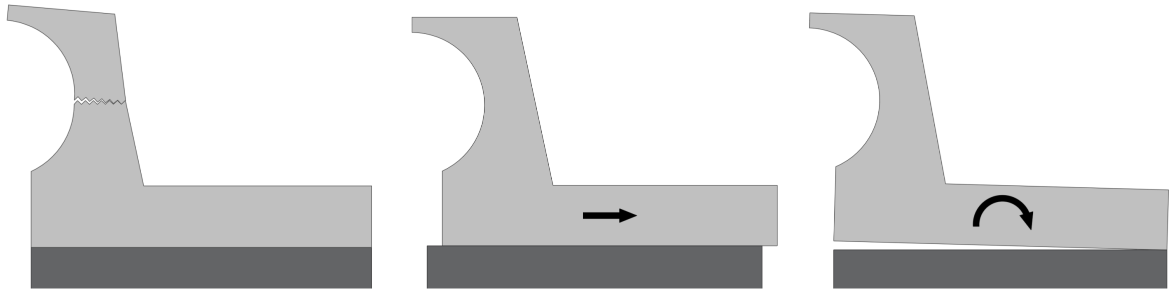

(a) Structural failure, cracking.

(b) Sliding.

(c) Overturning.

Figure 5.1: Three possible failure mechanisms for crownwalls.

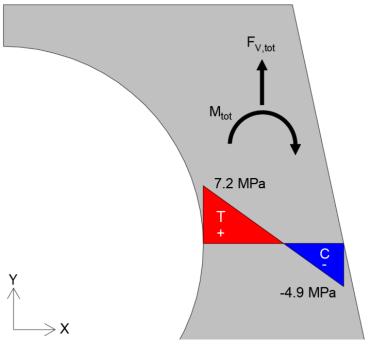

Figure 5.2: Distribution of stresses in the critical cross-section for case W7-U.

Figure 5.2 shows the stress distribution in the critical cross-section of the crownwall at the moment of maximum total force from the linear analysis (see chapter 3.3.2). This is the distribution of stresses in the Y-direction, σ_{YY}, in the *unsupported* crownwall under wave loading by W7 (case W7-U). The figure also shows the total bending moment, M_{tot}, and total vertical force, $F_{V,tot}$, acting on the crownwall at that moment. As shown in chapter 4, there is a total bending moment acting to the right due to the large wave forces and a total vertical force acting upwards, at the moment of the maximum total force. The vertical force will create tension in the entire cross-section but the bending moment will create tension in the front half and compression in the back half of the cross-section. Concrete is weak in tension, so, to design a fully curved crownwall that has sufficient bending moment resistance, two things can be done. Steel reinforcement bars can be added to increase the tensile strength of the concrete, as steel has high tensile strength. Another measure that can be taken is to increase the width of the critical cross-section of the structure. Stresses are defined as force (F) per cross-sectional area (A_c): $\sigma = F/A_c$. Therefore, by increasing the cross-sectional area of the crownwall, the stresses can be decreased. As the aim of the study was to, among else, compare the results of the analysis to the results of Dermentzoglou et al. (2021), reinforcement bars were not included in the FEM model as there were none included in their model of the recurved crownwall. That was because the recurved crownwall in Civitavecchia Harbour, Italy, was not constructed with reinforcement bars in the front of the crownwall but only in the back, as can be seen in figure 1.3a (Castellino et al., 2018a). However, reinforcement bars will be needed for the fully curved crownwall to avoid failure due to tensile cracking. The reinforcement bars have to be located in the curved front face of the crownwall and cover the entire part of the cross-section that is in tension at the moment of maximum stresses.

When comparing the results of the linear and nonlinear analysis of the *unsupported* and *supported* crownwalls, it is evident that the additional supporting wall does not have much influence on the structural failure of the crownwall. Both crownwalls show severe cracking for W6 and W7, as the cracks propagate through the entire cross-section. The tensile stresses will be lower in a supported crownwall, but when it comes to extreme waves of wave height larger than 6-7m, C-CI occurs and both the unsupported and supported crownwalls showed failure. The cracks occurred at or near the centre of the curve, which was also the case for a curved seawall in Strand, South Africa (Schoonees et al., 2014).

The assumption was made, in this study, that the crownwall is rigidly connected to the concrete caisson it rests on to simplify the FEM model and be coherent with the model of Dermentzoglou et al. (2021). However, hand calculations can quickly check whether the fully curved crownwall will slide or rotate under the wave loading of the three wave states. The role of the additional supporting wall behind the recurved crownwall in Civitavecchia harbour was to increase the weight of the crownwall and stop it from sliding. It is therefore worth checking whether the fully curved crownwall will also slide, as it is larger and has 10% more self-weight. The stability calculations, assumptions and results are in appendix C. The calculations show that under wave load from W6 and W7, the crownwall will slide and rotate, while for W5 it is stable, both with and without the additional supporting wall. To resist sliding under wave load from W7, the unsupported crownwall must have more than double its current self-weight. For the design of the fully curved crownwall, it should therefore be considered whether the wave conditions of W6 and W7 are likely to occur at the location and take appropriate measures in the design.

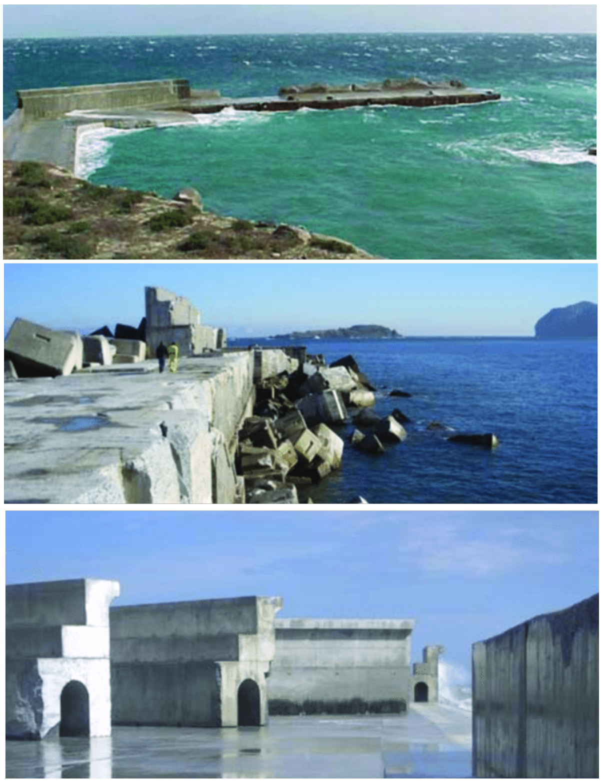

Figure 5.3: Structural failure in the port of the island of Albrán (top) and sliding and overturning of crownwalls in the ports of Bermeo (middle) and Motril (bottom), Spain (Valdecantos et al., 2014).

Regarding the geometry of curved crownwalls, studies on the radius and opening angle of crownwalls with a seawards facing overhang have shown that for a larger opening angle and a larger radius, the total force on the emerged part of the crownwall increases (Kortenhaus et al., 2003; Castellino et al., 2018a; Martinelli et al., 2018). For recurved crownwalls, the opening angle was found to have greater influence than the radius (Castellino et al., 2018b). The opening angle of recurved and fully curved crownwalls is the same, see figure 4.9, as the top of the curve of the overhang of both crownwalls is horizontal. The radius, however, is much larger for the fully curved crownwall ($r_{FC} = 2.4m$) than the recurved crownwall ($r_R = 1m$). The results of this analysis are therefore in comparison to other studies on the effect of a larger radius on the loading of crownwalls. To decrease the loading on the fully curved crownwall, the opening angle might be reduced from 90° to a smaller angle, although that will affect overtopping negatively (Castellino et al., 2018a).

5.2. Extended Goda method and static analysis

The load calculated by the extension of Castellino et al. (2021) to the Goda method (Goda, 1974) for C-CI wave loading and the CFD-generated wave load have been briefly compared in chapter 3.2. There it was found that the difference in maximum pressure was 2-11% and the difference in the total force was 5-35%, where the static load was larger than the CFD-generated load and the point of application of the total force was 0.1-0.5m higher. For comparison, the Goda method usually overestimates the wave force on a vertical wall by about 10% (Van Der Meer et al., 1994). Now the static FEM analysis results can be compared to the results of the dynamic linear analysis. It can be seen from figures 3.11 and 3.17 that the stress distributions are identical for the two analyses. Figure 5.4 shows on the y-axis the maximum stresses and displacement of probe 52 of the static analysis normalized with the maximum stresses and displacements of the dynamic linear analysis:

$$\sigma_{ratio} = \frac{\sigma_{static}}{\sigma_{dynamic}}$$

$$u_{xy,ratio} = \frac{u_{xy,static}}{u_{xy,dynamic}}$$

On the x-axis, the maximum total force calculated with the extended Goda method is normalized with the maximum total force of the largest wave in each wave state. The results of the unsupported crownwall are shown in red and the supported crownwall in blue. Normalized tensile stresses, in X- and Y-direction, are shown as a circle and diamond, respectively and normalized compressive stresses are shown as asterisks and ’x’ for the X- and Y-direction, respectively. The normalized displacements of probe 52 are shown as squares. The tensile stresses in the Y-direction are the most crucial, so they have a larger marker than other results.

The figure shows that for W5, the difference in force is larger than the difference in the static and dynamic analysis results, as all markers are to the right of the dashed diagonal line. For W6 and W7, the normalized total forces are also larger than most of the normalized stresses/displacements of the unsupported crownwall (red markers). For the supported crownwall (blue markers), it is the other way around, where most of the normalized stresses/displacements are larger than the normalized total force. This may be due to the high point of application of the static load, as it is located above the additional supporting wall and may affect the supported crownwall more than the unsupported crownwall. For W5, where the point of application of the total force was similar for both the static and dynamic load, the normalized stresses and displacements are all in a similar range of 1.2-1.35. However, for W6 and W7, where the point of application of the total force was higher for the static load, the normalized results for the supported wall are larger than the normalized results of the unsupported wall.

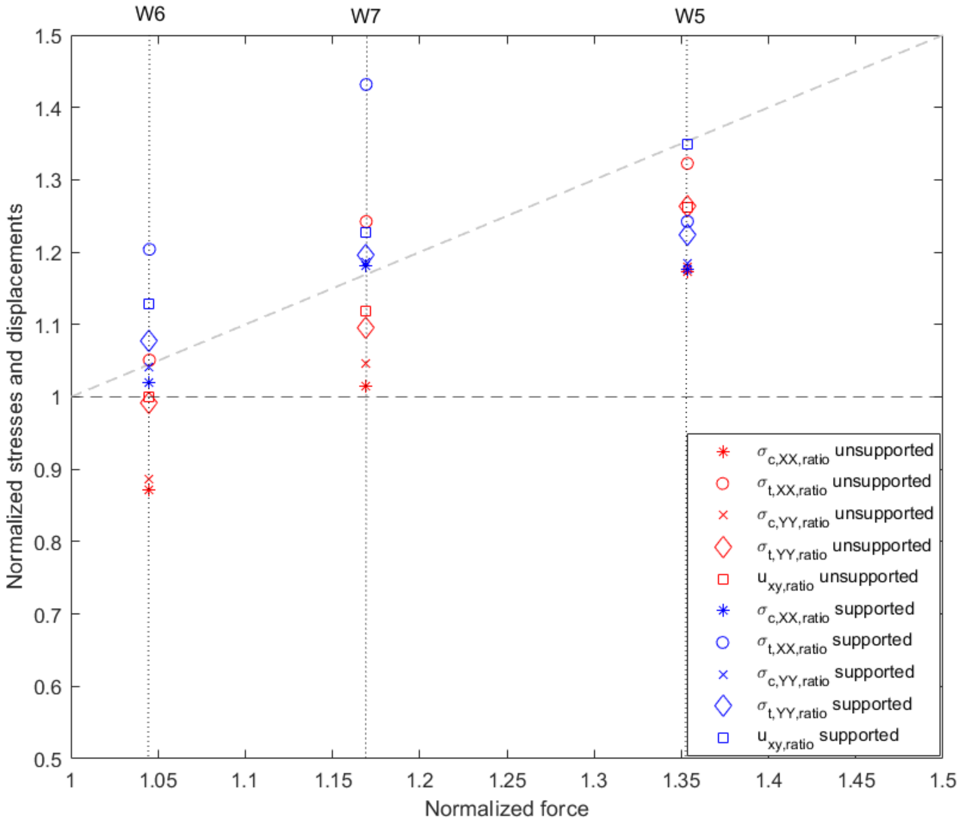

Figure 5.4: Stresses and displacements (of probe 52) of the static analysis normalized with the stresses and displacements of the dynamic analysis shown on the y-axis. The total force calculated with the extended Goda method normalized with the total force of the CFD-generated wave load.

In general, the results for stresses and displacements of the static analysis are larger than the results of the dynamic analysis. The normalized tensile stresses in the Y-direction (the diamonds in figure 5.4) are the most important results to discuss. For W6, the static analysis results in tensile stresses 0-7% larger than the dynamic analysis results. For W7, the static analysis results are 9-20% larger, and for W5, the static analysis results are about 25% larger for the unsupported and supported crownwall, respectively. For the unsupported crownwall, it can be seen that the normalized displacements and normalized tensile stresses in the Y-direction are almost equal or equal for all wave states. For the supported crownwalls, the normalized displacements are slightly larger than the normalized tensile stresses.

These results are promising for the usefulness of the extension of Castellino et al. (2021) to the Goda method to calculate the wave load for the static analysis of fully curved crownwalls. Regarding the tensile stresses, they are overestimated in all cases except for the unsupported crownwall under wave load from W6. It is preferable that the static method overestimates the wave force and response of the structure in order for the design of the structure to be on the safe side. It can therefore be estimated that for wave states with lower steepness and lower vertical wave velocity (W5 and W7), the method is more appropriate than for wave states with steeper waves. For steeper waves with higher vertical wave velocity, as in W6, the waves don't always run smoothly up the curve of the crownwall which may result in a different pressure distribution along the height of the crownwall.

One other thing to consider when comparing these results of the static and dynamic analysis is the possible amplification of the stresses and displacements due to the dynamic response of the structure in the dynamic analysis. In the design of hydraulic structures, it is common to use a dynamic amplification factor (DAF) to account for dynamic effects. For single degree of freedom (SDOF) systems, the DAF is simply the ratio between the dynamic and static response of the system, usually displacement or stresses, see equation 5.1 (Oumeraci & Kortenhaus, 1994). The static load or its response are then multiplied with the DAF to ensure a structurally sound design.

$$DAF = \frac{u_{dynamic,max}}{u_{static}} \tag{5.1}$$

Here, $u_{dynamic,max}$ represents the maximum displacement from a dynamic analysis and u_{static} is the displacement from a static analysis. The fully curved crownwall is, however, not an SDOF system as it has multiple eigenmodes which may be activated simultaneously and the response of the structure will be a superposition of several eigenmodes (Sleeuwaegen, 2020). According to Oumeraci and Kortenhaus (1994), it can be assumed that systems with more than one eigenmode are SDOF systems if the wave load has an impulse duration larger than 10% of T_n ($T_d \geq 0.1T_n$) and if the load is close to uniformly distributed over the front face of the structure. The first condition is fulfilled for the crownwall but not the latter condition.

The DAF method should therefore only be used in the preliminary design of the fully curved crownwall and not the final design, as it might underestimate the dynamic response of the structure. Calculating the DAF for the response of the crownwall to the three wave states can give an indication of whether the dynamic effects, mass and damping, amplify or reduce the response of the crownwall. The CFD-pressure time series is applied statically to the FEM model in Diana, meaning that dynamic effects are excluded. Using the resulting displacement of probe 52 in equation 5.1 it is found that the DAF for the three wave states is 1.1-1.3, which means that due to dynamic effects, the stresses and displacements are amplified by 10-30% depending on the loading. Therefore, it can be assumed that if the static load calculated with the extended Goda method were to be applied dynamically, the resulting displacements and stresses would increase by about 10-30%. These DAF values are in a similar range (1-1.5) as Oumeraci and Kortenhaus (1994) found in their dynamic analysis of caisson breakwaters under impulsive loading by breaking waves, where $1.5 < T_d/T_N < 3$.

6

Conclusion

In deep water conditions, curved crownwalls are often placed on top of vertical breakwaters to reduce wave overtopping. This thesis aimed to analyse the wave load of non-breaking waves on a fully curved crownwall and the dynamic response of the structure. This was to examine the difference in wave loading and dynamic response of a fully curved crownwall and a recurved crownwall. A fully curved crownwall with this specific shape has never been constructed on a vertical breakwater in non-breaking wave conditions but is more commonly used in seawalls where the wave load is by breaking or broken waves. In contrast, the shape of a recurved crownwall, with a seawards facing overhang at the top of the crownwall, has been widely used. e.g. in Civitavecchia Harbour. Another aim of the thesis was to estimate how well the extension by Castellino et al. (2018a) to the Goda method could estimate the static wave load on the crownwall. The extension was intended to be used for recurved crownwalls under C-CI wave loading. The following research question and sub-questions were formed and are answered in this chapter in the order they are listed.

What is the 2D dynamic response of a crownwall with a fully curved face to impulsive wave loading by non-breaking waves?

- How does the wave loading and dynamic response of a fully curved crownwall compare to that of a recurved crownwall?
- How does is effect the structural response of the crownwall to add a supporting wall behind it?
- How accurately does the extended Goda method for C-CI wave load by Castellino et al. (2021) estimate the wave load on the fully curved crownwall?
- How can this knowledge be used to give design recommendations regarding the geometry of curved crownwalls?

The analysis of a 2D CFD-generated pressure-time series of three different wave states showed that for the two largest wave states, W6 with $R_c/H < 1.08$ and W7 with $R_c/H < 0.92$, the C-CI phenomenon was evident in the pressure distribution along the height of the crownwall. However, the wave state with the lowest wave height, W5 with $R_c/H = 1.3$, had more of a trapezoidal pressure distribution and the pressure increase at the top of the crownwall was limited. Due to the considerable wave steepness of W6, $s = 6$%, the largest wave hits the crownwall differently from other waves, which results in a maximum pressure located just above the centre of the curve and a relatively large total force. Both the force and pressure impulses are found to be much less variable than the maximum force and pressure values. This indicates that the *pressure-impulse theory* might be suitable to evaluate the wave loading on fully curved crownwalls, e.g. as proposed by De Almeida and Hofland (2021).

Compared to the wave load by the same non-breaking wave states on the recurved crownwall, the analysis showed that the wave load is increased for the fully curved crownwall. The C-CI phenomenon is stronger for the recurved crownwall as there is a larger increase in pressure at the top of the crownwall than for the fully curved crownwall. However, the pressure over the height of the crownwalls is larger for the fully curved crownwall due to the momentum the wave gains as it travels up the curved front face. Thus, the maximum total force acting on the fully curved crownwall is 35-150% larger than the maximum total force acting on the recurved crownwall for all wave states. The difference in the maximum pressure is much less than in the total force for W6 and W7, about 15-20%, where the maximum pressure of the fully curved crownwall is larger. For W5, the difference in the maximum pressure is equal to the difference in the total force, about 35%, but the maximum pressure of the recurved crownwall is larger than the maximum pressure of the fully curved crownwall. In conclusion, the confinement of the wave crest is largest for the recurved crownwall, which results in a more significant pressure increase at the top of the crownwall, but as the pressure over the full height of the crownwall is larger for the fully curved crownwall, the fully curved crownwall is subjected to a larger total force.

Two FEM models were made in Diana FEA of the fully curved crownwall with different boundary conditions; one was only rigidly supported at the bottom, while the other was supported by a stiff boundary interface, reaching halfway up the vertical part of the crownwall. The stiff boundary interface replicates an additional supporting wall behind the crownwall. Pressure impacts were analysed for those waves of each wave state that reached the very top of the curve of the fully curved crownwall. By estimating the impulse duration, T_d, of the pressure impacts and comparing it to the natural period, T_n, of the two crownwalls, it was found that both W6 and W7 had waves in the dynamic domain of the structures, with $0.25 < T_d/T_n < 4$. Therefore, dynamic analysis was required to accurately evaluate the structural response of the crownwalls to the wave load. For the largest wave of W5, the pressure impulse durations were longer than four times the natural frequency of the structures, which means the wave was in the quasi-static domain of the crownwalls. Dynamic analysis was, however, performed for all wave states.

The linear analysis results show that when the fully curved crownwall is supported by an additional wall, the compressive stresses increase while the tensile stresses and displacements decrease. The decrease in displacements, and tensile stresses, of the top part of the crownwall, can be explained by the increased stiffness of the supported crownwall. The increase in the compressive stresses is due to the sharp change in boundary conditions where the additional supporting wall ends, as very high localized compressive stresses (singularities) occur at that location. For W6 and W7, the tensile stresses in the Y-direction, in the centre of the curve of both crownwalls, are larger than the tensile strength of the concrete. Nonlinear analysis was performed for the largest waves in W6 and W7, which showed severe cracking in both the unsupported and supported crownwalls. The maximum total crack widths for the unsupported crownwall are 22 mm and 48 mm for W6 and W7, respectively, while the maximum total crack widths in the supported crownwall are 29 mm and 38 mm. The supported crownwall cracks at the centre of the curve, for both W6 and W7, at the location where the supporting wall ends, where the cross-section is the narrowest. The unsupported crownwall cracks below the centre of the curve for W6, which is why the crack widths are smaller than for the supported crownwall. For W7, the unsupported crownwall cracks at two locations around the centre of the curve. Therefore, it can be concluded that for wave heights of 6-7m, both the supported and unsupported crownwall fail as cracks propagate through the whole cross-section. The fully curved crownwall must be steel reinforced concrete to not fail due to tensile cracking.

Comparing the results of the structural analysis of the supported fully curved crownwall and the results of the structural analysis of Dermentzoglou et al. (2021) on a supported recurved crownwall, it could be seen that the tensile stresses in the fully curved crownwall were up to 3 times larger than the tensile stresses in the recurved crownwall. The maximum tensile stresses in the recurved crownwall are below the concrete's tensile strength, and the wall did not crack under wave loading by W6 and W7. The large difference in the tensile stresses was linked to the large difference in the total bending moment by the wave load and self-weight of the top part of the crownwalls. There is a longer distance from the centre of the most critical cross-section to the point of application of the total vertical force for the fully curved crownwall. Combined with much larger wave forces, the bending moment created on the wall is much larger. One advantage of the geometry of the fully curved crownwall, compared to the recurved crownwall, is the size and shape of the top part, as it creates a 3.7 times larger bending moment to the left, compensating for the bending moment by the wave load. However, the increase in the bending moment by the self-weight is not large enough to fully compensate for the increased wave load on the fully curved crownwall compared to the recurved crownwall.

As a means to account for the C-CI phenomenon, Castellino et al. (2021) developed an extension to Goda's formulas, such that it can also be used for the static analysis of vertical breakwaters with a recurved parapet. Based on the results of this study, the method is considered suitable to estimate the C-CI wave load on a fully curved crownwall for preliminary static analysis, for wave states with wave steepness $s \leq 6\%$ and vertical wave load $u_z \leq 2.4m/s$. For waves with a larger wave steepness and vertical wave velocity, e.g. W6, the pressure distribution may differ from the C-CI phenomenon and the maximum pressure may not be at the top of the curve as assumed by the calculation method. The calculated total force is overestimated for all wave states by 5-35% and static analysis results (the maximum tensile stresses) are overestimated by 9-25%, for W5 and W7. The maximum tensile stresses in the *unsupported* crownwall for W6 are however underestimated. But, as the wave load is transient and, as shown in this study, pressure impulses of W6 and W7 are in the dynamic domain of the structure, the dynamic effects of the structure should be considered for the final design. That can be done either with a dynamic analysis or by applying a sufficiently large DAF to the static analysis. It should be kept in mind though that using a DAF to estimate the dynamic amplification might be an oversimplification of the dynamic response of the crownwall, as it is not an SDOF system.

The width of the cross-section of the fully-curved crownwall at the centre of the curve is the weakest part of the structure. Both the supported and unsupported crownwalls cracked at that location, as it is the narrowest part of the structure and has to take on all forces and moments exerted on the top part. Widening the narrowest part of the crownwall, at the centre of the curve, would reduce stresses and the chances of structural failure. However, if a sufficient amount of reinforcement bars are implemented in the design, widening the wall might be unnecessary. A cost-benefit analysis would be helpful to estimate what the optimal width is, based on the required amount of reinforcement bars.

In the re-entrant corner of the unsupported crownwall and at the location where the additional supporting wall ends, singularities occurred in the stress field. Sharp corners and sharp changes in boundary conditions should be avoided to avoid these large localised stresses. Re-entrant corners can be constructed with a certain small radius (fillet) and if additional supporting walls are needed, after a crownwall has been constructed, it should support the entire height of the crownwall or the width should be slowly decreased with height. Regarding the geometry of the curve of the crownwall, the results of this study support the findings of previous studies that an increase in the radius of the curve increases the wave load on the crownwall. It would be interesting to perform a parametric study of fully curved crownwalls, to investigate the effects of different radii and exit angles of the curve and how that might affect the wave load and overtopping.

Based on the results of this analysis, it can be concluded that fully curved crownwalls are less favourable than recurved crownwalls on vertical breakwaters. A fully curved crownwall, with the same freeboard (R_c) as a recurved crownwall, is a larger structure, so it requires more use of concrete. Due to larger tensile stresses, the fully curved crownwall also requires more steel reinforcement bars than the recurved crownwall. The construction of a fully curved crownwall will therefore cost more than that of a recurved crownwall. Following is a list of suggestions for future research:

1. **Wave load:** A more in-depth analysis of the results of the CFD-generated wave load on the fully curved crownwall would be necessary to understand better, for example, the loading by steep waves and the nature of the C-CI phenomenon. It would also be interesting to compare overtopping volumes of the fully curved and recurved crownwalls, to estimate which shape is more effective in reducing overtopping.

2. **Crownwall geometries:** Investigating further the effects of different radii of the curve of the fully curved crownwall. By, for example, changing the radius of the curve such that the critical cross-

section is made wider, might reduce the wave load on the structure and the maximum tensile stresses at the centre of the curve. This, however, might negatively affect the crownwalls performance with regard to overtopping as the exit angle will be smaller.

3. **Rigid body movements:** The FEM model used in this thesis did not account for rigid body movements, such as sliding and overturning. Modelling the crownwall with a friction interface instead of rigid connections would be interesting to investigate further sliding and overturning failures as they are known failure mechanisms of vertical breakwater crownwalls. This can be modelled in Diana FEA 10.5, by modelling the interface between the crownwall and the concrete caisson as a Coulomb friction interface. To allow for overturning of the crownwall, a specific tension cut-off value can be set such that when the normal traction in the interface reaches that tensile value the connection between the crownwall and the caisson is broken (DIANA FEA BV, 2021). For linear analysis of the crownwall with a nonlinear friction interface, the crownwall might have to be modelled with nonlinear material properties at the interface. It is, therefore, recommended to first start with a linear interface, then move to a Coulomb friction interface without a tension cut-off criteria (modelling only sliding) and model the bottom of the crownwall with nonlinear material properties. Finally, when that model has been validated and is working correctly, add the tension cut-off criteria (modelling sliding and overturning). It may be argued that, since the wall is more likely to slide than overturn (see appendix C), it is enough only to model the Coulomb friction interface, without the tension cut-off criteria. This assumption would simplify the already complicated model.

4. **3D analysis:** In this 2D analysis, it was assumed that the crownwall had infinite length, however, crownwalls have a finite length that depends on whether they are cast in situ or precast. A 3D FEM model of the crownwall could be used to study the dynamic reaction to oblique wave loading and the effects of the finite length of the crownwall. The method developed by Mares-Nasarre and van Gent (2020) to estimate the wave loading by oblique waves on crest walls could be used in this 3D analysis. The method estimates the reduction in the maximum wave force due to the incoming angle of the waves and estimates the spatial distribution along the length of the crownwall.

References

Bagnold, R. A. (1939). Interim Report on Wave-Pressure Research (Includes Plates and Photographs). *Journal of the Institution of Civil Engineers*, *12*(7), 202–226.

Castellino, M., Sammarco, P., Romano, A., Martinelli, L., Ruol, P., Franco, L., & De Girolamo, P. (2018a). Large impulsive forces on recurved parapets under non-breaking waves. A numerical study. *Coastal Engineering*, *136*, 1–15. https://doi.org/10.1016/j.coastaleng.2018.01.012

Castellino, M., Lara, J. L., Romano, A., Losada, I. J., & De Girolamo, P. (2018b). Wave loading for recurved parapet walls in non-breaking wave conditions: analysis of the induced impulsive forces. (36), 34–34.

Castellino, M., Romano, A., Lara, J. L., Losada, I. J., & De Girolamo, P. (2021). Confined-crest impact: Forces dimensional analysis and extension of the Goda's formulae to recurved parapets. *Coastal Engineering*, *163*. https://doi.org/10.1016/j.coastaleng.2020.103814

Chen, X., Hofland, B., Molenaar, W., Capel, A., & Van Gent, M. R. (2019). Use of impulses to determine the reaction force of a hydraulic structure with an overhang due to wave impact. *Coastal Engineering*, *147*, 75–88. https://doi.org/10.1016/j.coastaleng.2019.02.003

Cooker, M. J., & Peregrine, D. H. (1990). A Model for Breaking Wave Impact Pressures. *Coastal engineering proceedings*, 22.

Cooker, M. J., & Peregrine, D. H. (1995). Pressure-impulse theory for liquid impact problems. *Journal of Fluid Mechanics*, *297*, 193–214. https://doi.org/10.1017/S0022112095003053

Cuomo, G., Allsop, W., Bruce, T., & Pearson, J. (2010). Breaking wave loads at vertical seawalls and breakwaters. *Coastal Engineering*, *57*(4), 424–439. https://doi.org/10.1016/j.coastaleng.2009.11.005

Cuomo, G., Lupoi, G., Shimosako, K. i., & Takahashi, S. (2011). Dynamic response and sliding distance of composite breakwaters under breaking and non-breaking wave attack. *Coastal Engineering*, *58*(10), 953–969. https://doi.org/10.1016/J.COASTALENG.2011.03.008

De Almeida, E., & Hofland, B. (2021). Standing wave impacts on vertical hydraulic structures with overhangs for varying wave fields and configurations. https://doi.org/10.48438/jchs.2021.0010

De Almeida, E., Hofland, B. ; & Jonkman, S. J. ; (2019). Wave Impact Pressure-Impulse on Vertical Structures with Overhangs. *Coastal Structures*, 86–96. https://doi.org/10.18451/978-3-939230-64-9{_}010

De Almeida, E., & Hofland, B. (2020). Validation of pressure-impulse theory for standing wave impact loading on vertical hydraulic structures with short overhangs. *Coastal Engineering*, *159*. https://doi.org/10.1016/j.coastaleng.2020.103702

De Girolamo, P., Castellino, M., & Romano, A. (2019). Improvement in Workability if Terminals Placed Along the Inner Side of Port Vertical Breakwaters by Means of Recurved Parapet Walls. *WIT Transactions on The Built Environment*, *187*, 23–30. https://doi.org/10.2495/MT190031

Dermentzoglou, D. (2021). *Crownwalls with a fully curved face. An experimental study* (tech. rep.). Master's Thesis, Delft University of Technology. http://repository.tudelft.nl/.

Dermentzoglou, D., Castellino, M., De Girolamo, P., Partovi, M., Schreppers, G. J., & Antonini, A. (2021). Crownwall failure analysis through finite element method. *Journal of Marine Science and Engineering*, *9*(1), 1–17. https://doi.org/10.3390/jmse9010035

DIANA FEA BV. (2021). DIANA Finite Element Anlaysis - User's manual 10.5.

EurOtop. (2018). Manual on wave overtopping of sea defences and related structures. An overtopping manual largely based on European research, but for worldwide application. Van der Meer, J.W., Allsop, N.W.H., Bruce, T., De Rouck, J., Kortenhaus, A., Pullen, T., Schüttrumpf, H., Troch, P. and Zanuttigh, B. www.overtopping-manual.com

Fib. (2013). *Fib Model Code for Concrete Structures 2010* (tech. rep.). International Federation for Structural Concrete. Lausanne, Switzerland.

Goda, Y. (1974). New wave pressure formulae for composite breakwaters. *Coastal Engineering Proceedings*, 1702–1720.

Goda, Y. (1994). Dynamic response of upright breakwaters to impulsive breaking wave forces. *Coastal Engineering*, *22*(1-2), 135–158. https://doi.org/10.1016/0378-3839(94)90051-5

Google. (n.d.). Google Map image of curved seawall in Penhryn Bay, Wales. https://www.google.com/maps/@53.3181667,-3.7632883,3a,75y,280.25h,86.91t/data=!3m8!1e1!3m6!1sAF1QipNWnPMXuDvkGot4uvf9ik1PfK9q2FhH5YOrweoq!2e10!3e11!6shttps:%2F%2Flh5.googleusercontent.com%2Fp%2FAF1QipNWnPMXuDvkGot4uvf9ik1PfK9q2FhH5YOrweoq%3Dw203-h100-k-no-pi-0-ya98.010284-ro-0-fo100!7i5376!8i2688

Higuera, P., Lara, J. L., & Losada, I. J. (2013a). Realistic wave generation and active wave absorption for Navier–Stokes models: Application to OpenFOAM®. *Coastal Engineering*, *71*, 102–118. https://doi.org/10.1016/J.COASTALENG.2012.07.002

Higuera, P., Lara, J. L., & Losada, I. J. (2013b). Simulating coastal engineering processes with OpenFOAM®. *Coastal Engineering*, *71*, 119–134. https://doi.org/10.1016/J.COASTALENG.2012.06.002

Higuera, P., Lara, J. L., & Losada, I. J. (2014). Three-dimensional interaction of waves and porous coastal structures using OpenFOAM®. Part I: Formulation and validation. *Coastal Engineering*, *83*, 243–258. https://doi.org/10.1016/j.coastaleng.2013.08.010

Huang, J., & Chen, G. (2020). Experimental study on wave impulse and characteristic pressure of a vertical wall with overhanging horizontal cantilever slab. *Ocean Engineering*, *217*, 108055. https://doi.org/10.1016/J.OCEANENG.2020.108055

Huang, J., Chen, G., & Lowe, R. J. (2022). Experimental Study on the Probability of Different Wave Impact Types on a Vertical Wall with Horizontal Slab by Separation of Quasi-Static Wave Impacts. *Journal of Marine Science and Engineering*, *10*(5). https://doi.org/10.3390/jmse10050615

Kisacik, D., Troch, P., & Van Bogaert, P. (2012). Description of loading conditions due to violent wave impacts on a vertical structure with an overhanging horizontal cantilever slab. *Coastal Engineering*, *60*(1), 201–226. https://doi.org/10.1016/J.COASTALENG.2011.10.001

Kisacik, D., Troch, P., Van Bogaert, P., & Caspeele, R. (2014). Investigation of uplift impact forces on a vertical wall with an overhanging horizontal cantilever slab. *Coastal Engineering*, *90*, 12–22. https://doi.org/10.1016/J.COASTALENG.2014.04.011

Kortenhaus, A., Pearson, J., Bruce, T., Allsop, N. W., & Van Der Meer, J. W. (2003). Influence of parapets and recurves on wave overtopping and wave loading of complex vertical walls. *Coastal Structures 2003 - Proceedings of the Conference*, 369–381. https://doi.org/10.1061/40733(147)31

Kortenhaus, A., & Oumeraci, H. (1999). Classification of wave loading on monolithic coastal structures. *Coastal Engineering 1998*, 867–880.

Mares-Nasarre, P., & van Gent, M. R. (2020). Oblique Wave Attack on Rubble Mound Breakwater Crest Walls of Finite Length. *Water 2020, Vol. 12, Page 353*, *12*(2), 353. https://doi.org/10.3390/W12020353

Martinelli, L., Ruol, P., Volpato, M., Favaretto, C., Castellino, M., De Girolamo, P., Franco, L., Romano, A., & Sammarco, P. (2018). Experimental investigation on non-breaking wave forces and overtopping at the recurved parapets of vertical breakwaters. *Coastal Engineering*, *141*, 52–67. https://doi.org/10.1016/j.coastaleng.2018.08.017

Naeimi, N., & Moustafa, M. A. (2017). Three-dimensional finite element modeling of UHPC using total strain crack models. *AFGC-ACI-Fib-RILEM Int. Symp. Ultra-High Perform. Fibre-Reinforced Concr. UHPFRC.*

Negro, V., Martín-Antón, M., del Campo, J. M., López-Gutiérrez, J. S., & Esteban, M. D. (2018). Crown walls in mass and reinforced concrete: the way to aesthetics in maritime works. In *Coasts, marine structures and breakwaters 2017: Realising the potential* (pp. 471–480). ICE Publishing.

Oumeraci, H., & Kortenhaus, A. (1994). Analysis of the dynamic response of caisson breakwaters. *Coastal Engineering*, *22*(1-2), 159–183. https://doi.org/10.1016/0378-3839(94)90052-3

Oumeraci, H., Partenscky, H. W., Tautenhain, E., & Nickels, H. (1992). 13. Large-scale model investigation: a contribution to the revival of vertical breakwaters. In *Coastal structures and breakwaters: Proceedings of the conference organized by the institution of civil engineers, and held in london on 6-8 november 1991* (pp. 207–220). Thomas Telford.

Paultre, P. (2013). *Dynamics of Structures*. John Willey & Sons. https://books.google.nl/books?hl=en&lr=&id=XlRiWUJ_DxEC&oi=fnd&pg=PT12&dq=dynamics+of+structures+chopra&ots=DnF5gvZIG6&sig=zU7iP_go5ZkXq3-Isq1mCUJH4xQ&redir_esc=y#v=snippet&q=rayleigh%20damping&f=false

Pearson, J., Bruce, T., Allsop, W., Kortenhaus, A., & Van Der Meer, J. (2005). Effectiveness of recurve walls in reducing wave overtopping on seawalls and breakwaters. In *Coastal engineering 2004: (in 4 volumes)* (pp. 4404–4416).

Pedersen, J., & Burcharth, H. F. (1993). Wave forces on crown walls. In *Coastal engineering 1992* (pp. 1489–1502).

Ramkema, C. (1978). A model law for wave impacts on coastal structures. *Coastal Engineering Proceedings*, (16), 139–139.

Rots, J. G. (1991). Smeared and discrete representations of localized fracture. In *Current trends in concrete fracture research* (pp. 45–59). Springer. https://doi.org/10.1007/978-94-011-3638-9

Schoonees, T., Mr, S. : & Toms, G. (2014). *Impermeable recurve seawalls to reduce wave overtopping* (tech. rep.). http://scholar.sun.ac.za

Selby, R. G., & Vecchio, F. J. (1993). Three-dimensional constitutive relations for reinforced concrete. University of Toronto. *Department of Civil Engineering, 147*, 93–02.

Shimosako, K., Takahashi, S., & Tanimoto, K. (1994). Estimating the Sliding Distance of Composite Breakwaters due to Wave Forces Inclusive of Impulsive Forces. *Coastal Engineering Proceedings*, 24.

Sleeuwaegen, S. (2020). *The dynamic behaviour of hydraulic structures caused by wave impact loads: Enhancing the present design method in time and space* (tech. rep.). Master's Thesis, Delft University of Technology. http://repository.tudelft.nl/.

Słowik, M. (2019). The analysis of failure in concrete and reinforced concrete beams with different reinforcement ratio. *Archive of Applied Mechanics*, *89*(5), 885–895. https://doi.org/10.1007/s00419-018-1476-5

Stagonas, D., Lara, J. L., Losada, I. J., Higuera, P., Jaime, F., & Muller, G. (2014). Large scale measurements of wave loads and mapping of impact pressure distribution at the underside of wave recurves. *Proceedings of the HYDRALAB IV Joint User Meeting*, (1).

Stagonas, D., Ravindar, R., Sriram, V., & Schimmels, S. (2020). Experimental Evidence of the Influence of Recurves on Wave Loads at Vertical Seawalls. *Water 2020, Vol. 12, Page 889*, *12*(3), 889. https://doi.org/10.3390/W12030889

Streicher, M., Kortenhaus, A., Marinov, K., Hirt, M., Hughes, S., Hofland, B., Scheres, B., & Schüttrumpf, H. (2019). Classification of bore patterns induced by storm waves overtopping a dike crest and their impact types on dike mounted vertical walls - A large-scale model study. *Coastal Engineering Journal*, *61*(3), 321–339. https://doi.org/10.1080/21664250.2019.1589635

Takahashi, S. (2002). Design of vertical breakwaters. *PHRI reference document nr. 34*.

Takahashi, S., Tsuda, M., Suzuki, K., & Shimosako, K.-I. (1998). Experimental and FEM Simulation of the Dynamic Response of a Caisson Wall Against Breaking Wave Impulsive Pressures. *Coastal Engineering Proceedings*, (26).

Tieleman, O. C., Hofland, B., Tsouvalas, A., de Almeida, E., & Jonkman, S. N. (2021). A fluid–structure interaction model for assessing the safety of flood gate vibrations due to wave impacts. *Coastal Engineering*, *170*, 104007. https://doi.org/10.1016/J.COASTALENG.2021.104007

Valdecantos, V. N., GutiéRrez, J. S. L., Flors, J. I. P., & Molines, J. (2014). Discussion: Comparative study of breakwater crown wall - calculation methods. *Proceedings of the Institution of Civil Engineers: Maritime Engineering*, *167*(3), 154–155. https://doi.org/10.1680/maen.14.00002

Van Der Meer, J. W., D'angremond, K., & Juhl, J. (1994). PROBABILISTIC CALCULATIONS OF WAVE FORCES ON VERTICAL STRUCTURES. *Coastal Engineering Proceedings*, *1*(24). https://doi.org/https://doi.org/10.9753/icce.v24.{\%}p

van Gent, M. R. (2021). Influence of oblique wave attack on wave overtopping at caisson breakwaters with sea and swell conditions. *Coastal Engineering*, *164*. https://doi.org/10.1016/j.coastaleng.2020.103834

Vecchio, F. J., & Collins, M. P. (1986). The modified compression-field theory for reinforcedconcrete elements subjected to shear. *ACI J.*, *83*(2), 219–231.

Voorendt, M. Z., & Molenaar, W. F. (2020). *Manual: Hydraulic Structures* (tech. rep.). Delft University of Technology. Delft.

Wood, D. J., & Peregrine, D. H. (1996). Wave impact beneath a horizontal surface. *Coastal Engineering Proceedings*, (25).

Wood, D. J., Peregrine, D. H., & Bruce, T. (2000). Wave impact on a wall using pressure-impulse theory. I: trapped air. *Journal of Waterway, port, coastal, and ocean engineering*, *126*(4), 182–190.

List of Figures

List of Tables

A

Static wave load

A.1. Goda's method

The following calculation method of a static wave load on a vertical wall is an extended Goda method by Takahashi (2002).

$$\eta^* = 0.75(1 + cos\theta)\lambda_1 H_D \tag{A.1}$$

$$p_1 = 0.5(1 + cos\theta)(\lambda_1\alpha_1 + \lambda_2\alpha_2 cos^2\theta)\rho g H_D \tag{A.2}$$

$$p_3 = \alpha_3 p_1 \tag{A.3}$$

$$p_4 = \alpha_4 p_1 \tag{A.4}$$

$$p_u = 0.5(1 + cos\theta)\lambda_3\alpha_1\alpha_3\rho g H_D \tag{A.5}$$

in which:

$$\alpha_1 = 0.6 + 0.5\left(\frac{4\pi h/L_D}{sinh(4\pi h/L_D)}\right)^2 \tag{A.6}$$

$$\alpha_2 = max\left(\frac{(1 - d/h_b)(H_D/d)^2}{3}, \frac{2d}{H_d}\right) \tag{A.7}$$

$$\alpha_3 = 1 - (h'/h)\left(1 - \frac{1}{cosh(2\pi h/L_D)}\right) \tag{A.8}$$

$$\alpha_4 = 1 - h_c^*/\eta^* \tag{A.9}$$

$$h_c^* = min(\eta^*, h_c) \tag{A.10}$$

where:

η^*	is the elevation at which the wave pressure is exerted
θ	is the angle of the incident wave, normally incident waves have $\theta = 0°$
p_1	is the wave pressure at SWL
p_3	is the wave pressure at the toe of the wall

p_4	is the wave pressure at the top of the wall
p_u	is the uplift wave pressure acting on the bottom of the caisson
$\lambda_{1,2,3}$	are modification factors dependent on the shape of the structure, for a vertical wall $\lambda_1 = \lambda_2 = \lambda_3 = 1$
H_D	is the design wave height
L_D	is the design wave length
d	is the water depth above the top sill
h_b	is the water depth at a distance of $5H_D$ from the wall
h'	is the water depth above the wall foundation plane
h	is the water depth in front of the sill
h_c	is the freeboard of the wall, $h_c = R = 6.5m$

Figure A.1 shows the parameters used in the Goda method and the wave pressure distribution. For this analysis, it is assumed that the seawall rests on a flat seabed, so $h = h_b = h' = d = 20m$, and as only the crownwall is being analysed the uplift pressure p_u is not calculated. The results of the calculations can be seen in table A.1.

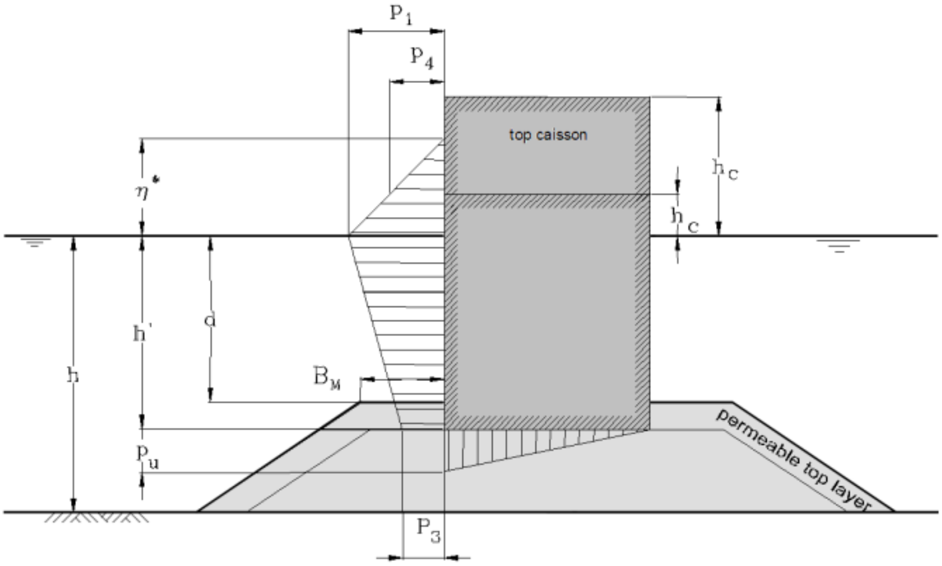

Figure A.1: Goda wave pressure distribution (figure from Voorendt and Molenaar (2020)).

Table A.1: Results of Goda's formulas for wave pressrue on a vertical wall.

Wave state	H [m]	T [s]	p_1 [kPa]	p_3 [kPa]	p_4 [kPa]
W5	5	8	33.5	17.6	4.5
W6	6	8	40.2	21.2	11.2
W7	7	11	60.8	49.5	23.2

A.2. Extended Goda method for curved parapets

The following method was developed by Castellino et al. (2021) as an extension to the Goda method (Goda, 1974) for recurved parapets, to account for the C-CI phenomenon. The total static wave pressure on a recurved parapet is indicated by P_R and can be calculated using the following equation:

$$P_R = P_V(1 + \tilde{p}) \tag{A.11}$$

where P_V is the wave pressure acting on a vertical wall calculated by the Goda method and the factor $\tilde{p} = P_R/P_V$ is the parameterized wave pressure distribution. Figure A.2 shows the location of the three different $\tilde{p}$ parametrization factors and figures A.3a and A.3b show the equations for $\tilde{p}_2$ and $\tilde{p}_3$. As figure A.2 shows $\tilde{p}_1$ is set equal to 1.

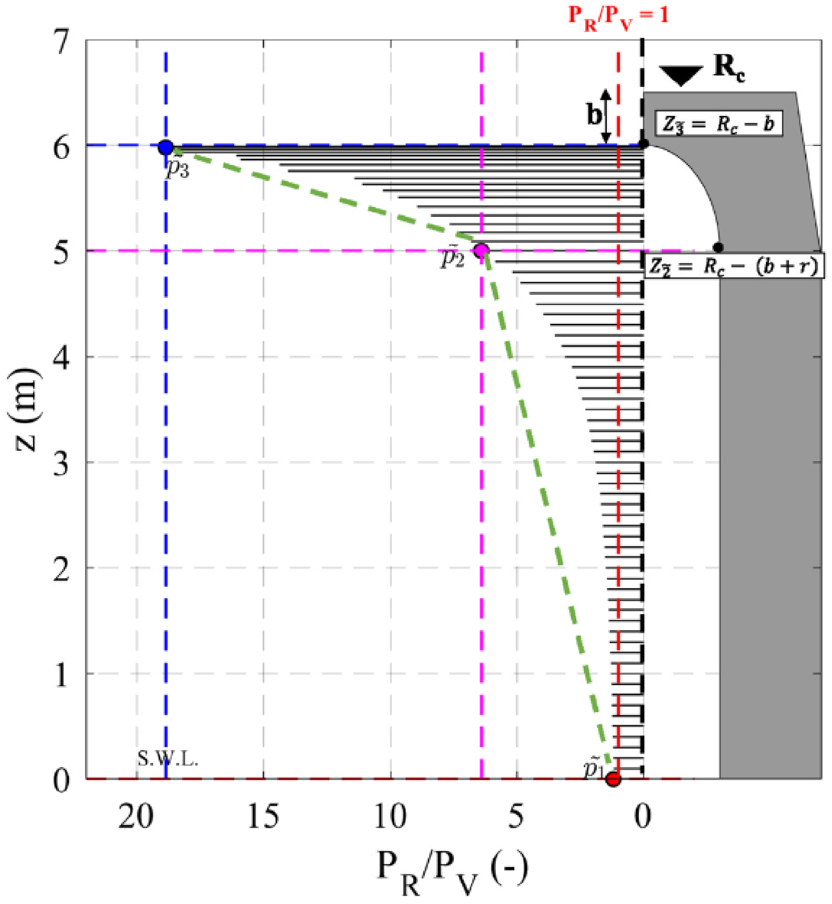

Figure A.2: Location of the parametrization factors $\tilde{p}_1$, $\tilde{p}_2$ and $\tilde{p}_3$ (figure from Castellino et al. (2021)).

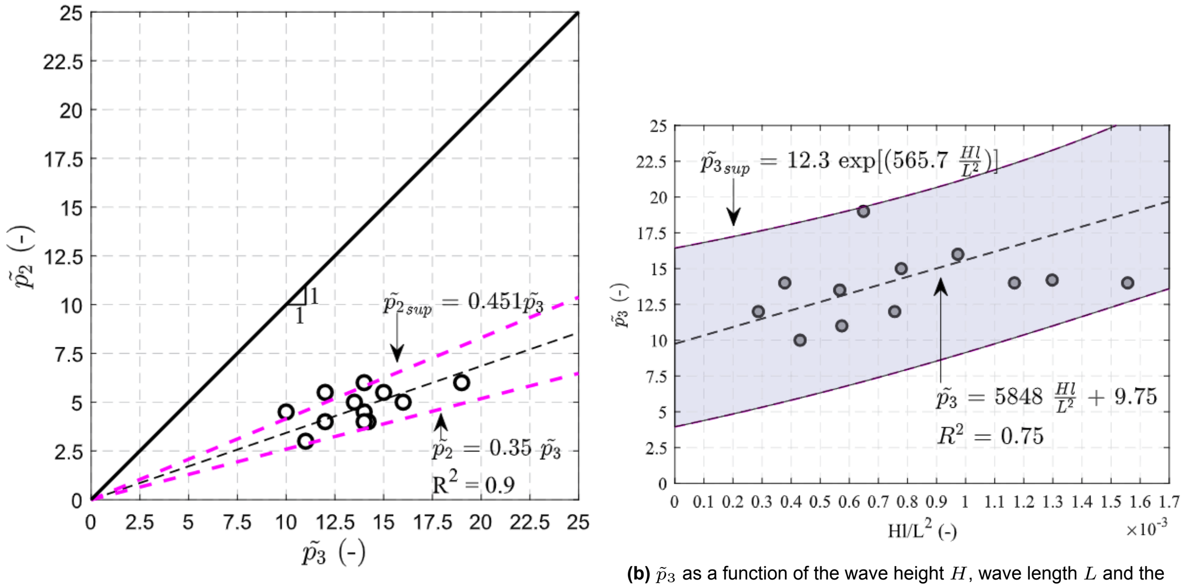

(a) $\tilde{p}_2$ as a function of $\tilde{p}_3$.

(b) $\tilde{p}_3$ as a function of the wave height H, wave length L and the overhang length l.

Figure A.3: Values of $\tilde{p}_2$ and $\tilde{p}_3$ for different geometries of the recurved crownwall and different wave conditions. Equations are given for the linear fitting line and the upper confidence band of the 95% confidence interval. Figures from Castellino et al. (2021)

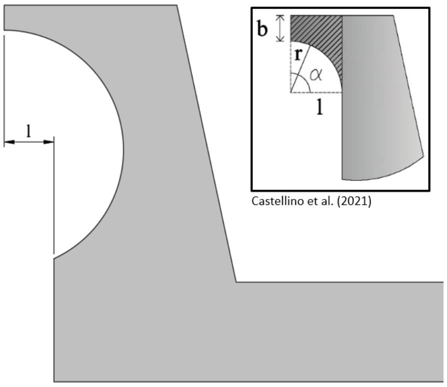

Castellino et al. (2021)

Figure A.4: Definition of the overhang length l for the recurved crownwall Castellino et al., 2021 and the fully curved crownwall.

For the recurved parapet, the overhang length is calculated as $l = r(1 - cos\alpha)$, where r is the radius of the curve and α is the opening angle, see figure A.4. For the fully curved parapet, the overhang length is taken as the horizontal distance from the vertical part of the crownwall to the top of the curve as shown in figure A.4.

For each wave state, $\tilde{p}_2$ and $\tilde{p}_3$ are calculated using the equation for the linear fitting line and for $\tilde{p}_3$ the equation for the upper confidence band is also used. The total static wave pressure, P_R, can then be calculated using equation A.11. It can be seen from figure A.5 that for wave states 6 and 7 the pressure distribution that results from using the upper confidence band for $\tilde{p}_3$ fits better to the pressure distribution of the CFD generated pressure time series at the moment of maximum pressure. However, for W5 the static wave pressure distribution looks wrong, as the maximum pressure is at the location of $\tilde{p}_2$ but not at $\tilde{p}_3$ as it should. From figure A.3a it can be estimated that the equation for the lower confidence band of the 95% confidence interval is:

$$\tilde{p}_{2,low} = 0.26\tilde{p}_3.$$

So, for W5 the equation for the linear fitting line is used for $\tilde{p}_3$ and the equation for the lower confidence band is used for $\tilde{p}_2$.

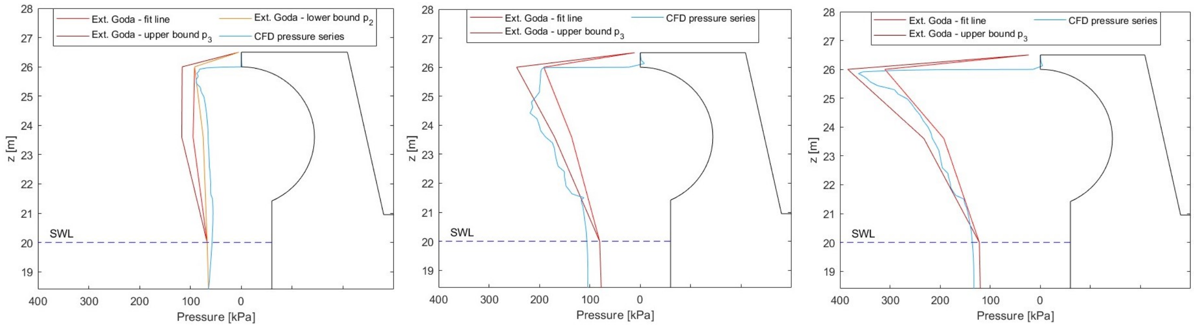

(a) W5 ($H = 5m, T = 8s$).

(b) W6 ($H = 6m, T = 8s$).

(c) W7 ($H = 7m, T = 11s$).

Figure A.5: Results of the extended Goda method Castellino et al., 2021 compared to the pressure distribution at the moment of max. pressure of the CFD-generated pressure time series (blue line). Results of linear fitting lines in bright red, results of linear fitting line for $\tilde{p}_2$ and upper bound equation for $\tilde{p}_3$ in dark red and for W5 results of lower bound equation for $\tilde{p}_2$ and fitting line for $\tilde{p}_3$ in orange.

B

Linear analysis results

B.1. Wave state 5

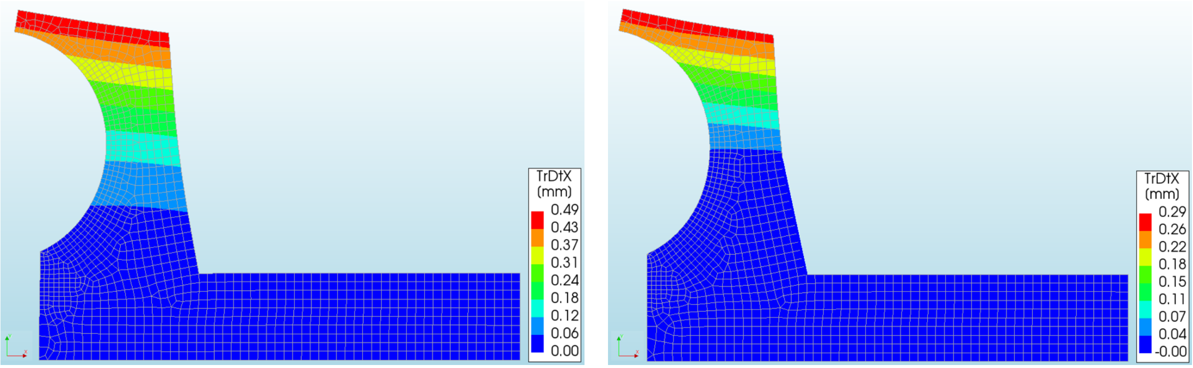

(a) Contour plot of displacements in x-direction, unsupported wall. **(b)** Contour plot of displacements in x-direction, supported wall.

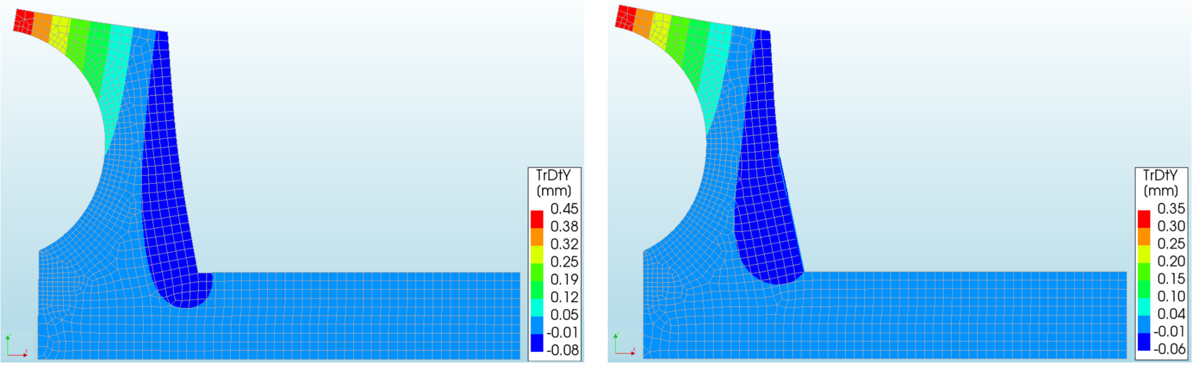

(c) Contour plot of displacements in y-direction, unsupported wall. **(d)** Contour plot of displacements in y-direction, supported wall.

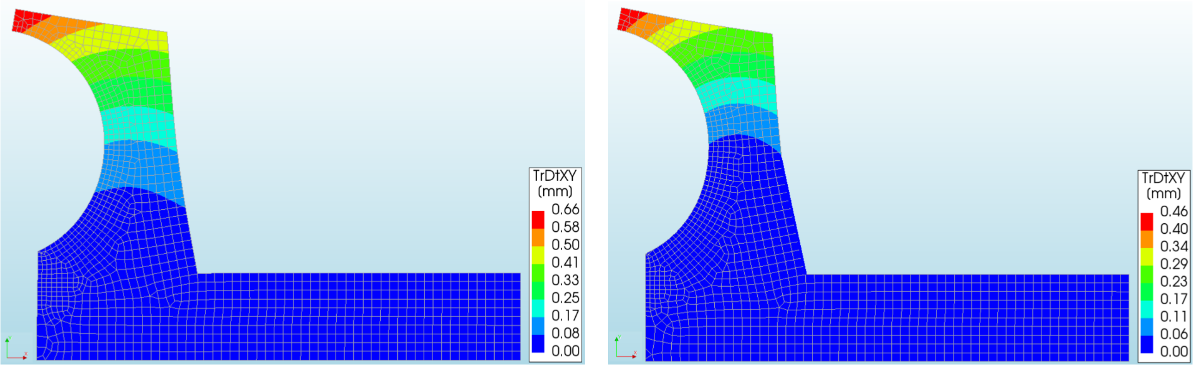

(e) Contour plot of displacements in xy-direction, unsupported wall. **(f)** Contour plot of displacements in xy-direction, supported wall.

Figure B.1: Contour plots of displacement for the unsupported (to the left) and supported (to the right) crownwalls at the moment of maximum pressure of W5.

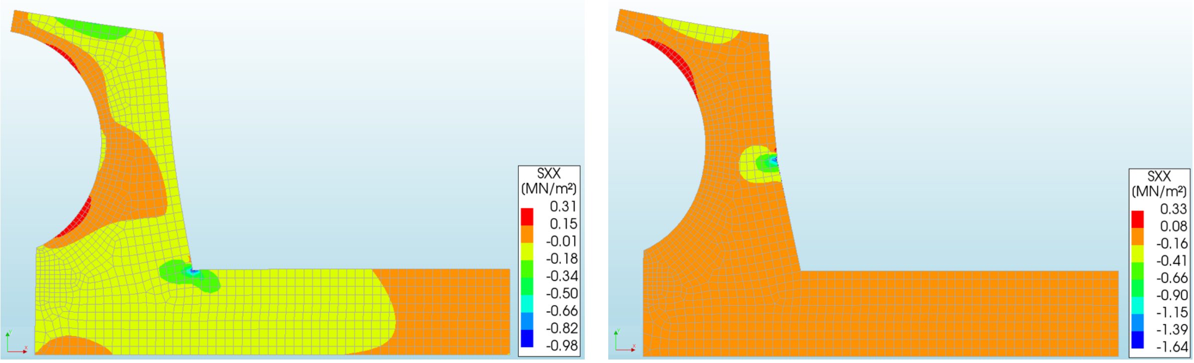

(a) Contour plot of stresses in x-direction, unsupported wall.

(b) Contour plot of stresses in x-direction, supported wall.

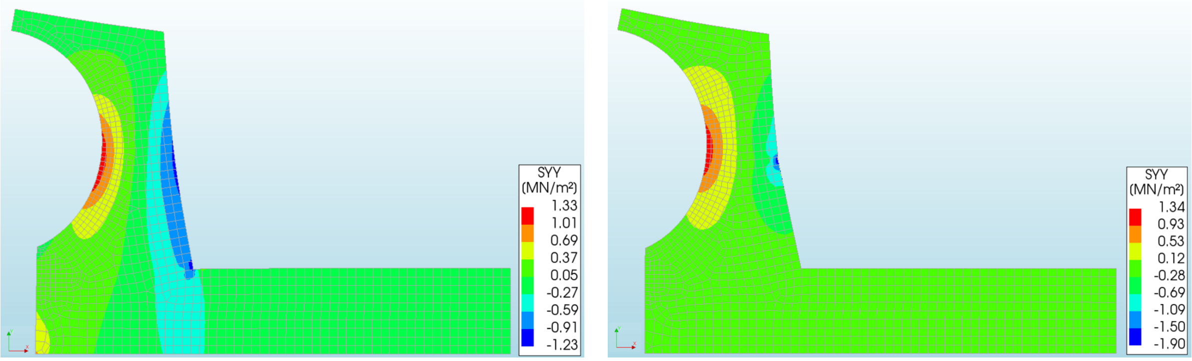

(c) Contour plot of stresses in y-direction, unsupported wall.

(d) Contour plot of stresses in x-direction, unsupported wall.

Figure B.2: Contour plots of stresses for the unsupported (to the left) and supported (to the right) crownwalls at the moment of maximum pressure of W5.

B.2. Wave state 6

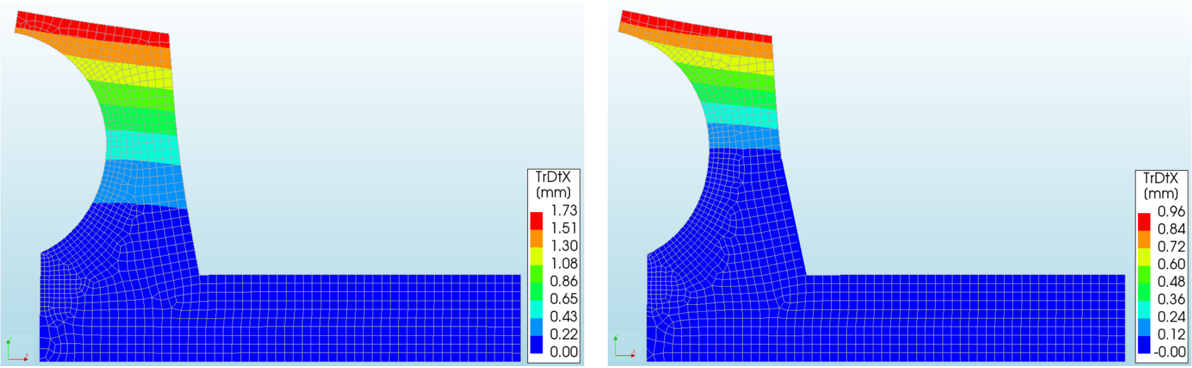

(a) Contour plot of displacements in x-direction, unsupported wall. **(b)** Contour plot of displacements in x-direction, supported wall.

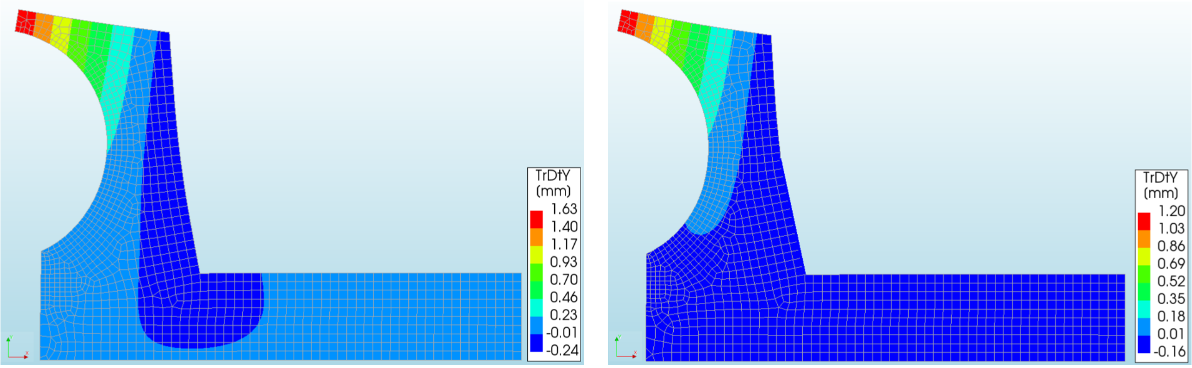

(c) Contour plot of displacements in y-direction, unsupported wall. **(d)** Contour plot of displacements in y-direction, supported wall.

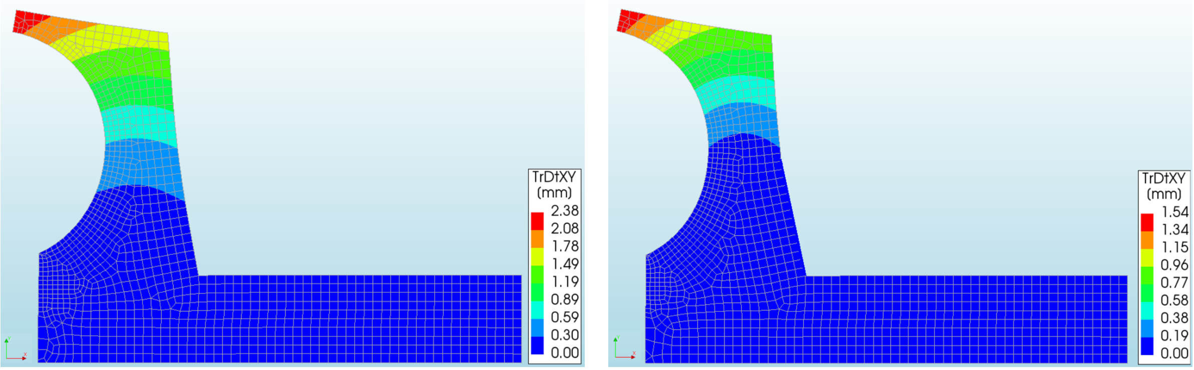

(e) Contour plot of displacements in xy-direction, unsupported wall. **(f)** Contour plot of displacements in xy-direction, supported wall.

Figure B.3: Contour plots of displacement for the unsupported (to the left) and supported (to the right) crownwalls at the moment of maximum pressure of W6.

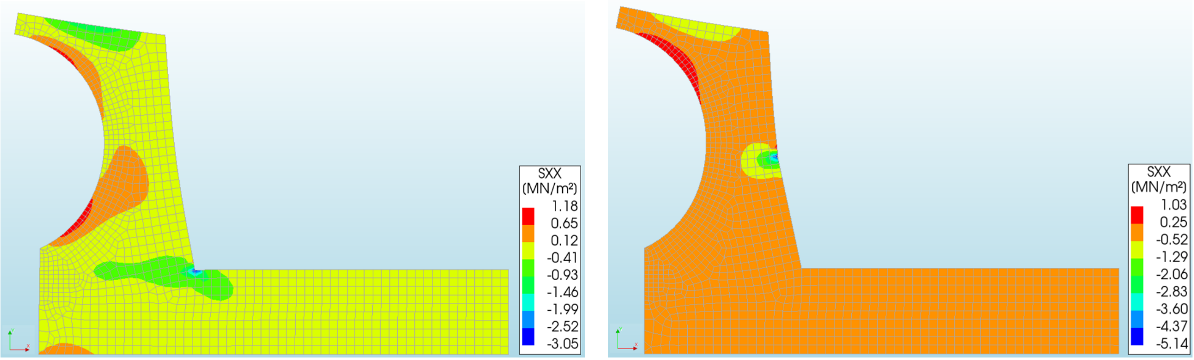

(a) Contour plot of stresses in x-direction, unsupported wall.

(b) Contour plot of stresses in x-direction, supported wall.

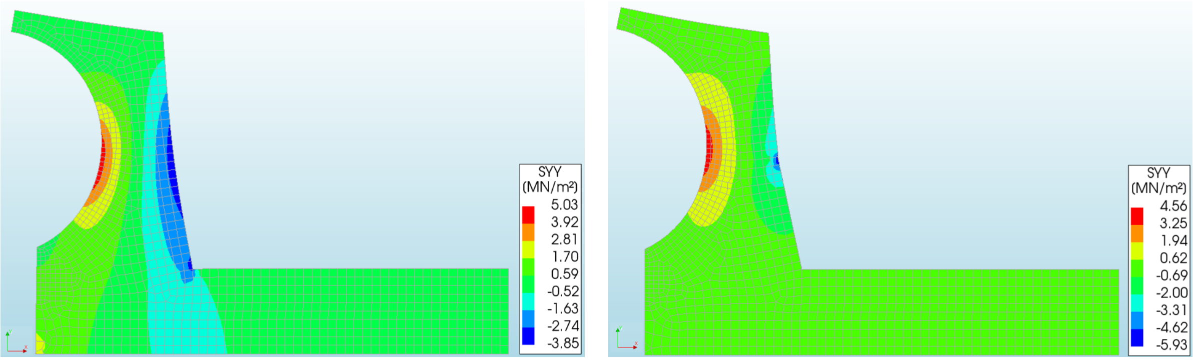

(c) Contour plot of stresses in y-direction, unsupported wall.

(d) Contour plot of stresses in y-direction, supported wall.

Figure B.4: Contour plots of stresses for the unsupported (to the left) and supported (to the right) crownwalls at the moment of maximum pressure of W6.

B.3. Wave state 7

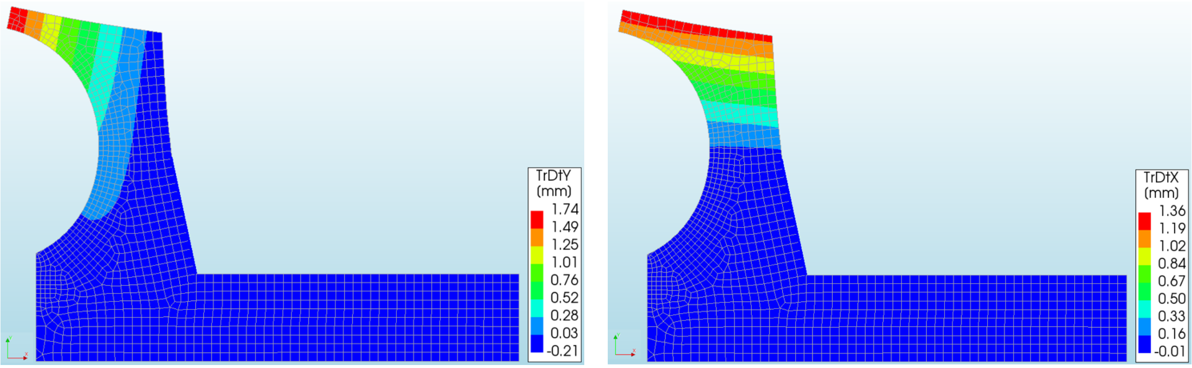

(a) Contour plot of displacements in x-direction, unsupported wall.

(b) Contour plot of displacements in x-direction, supported wall.

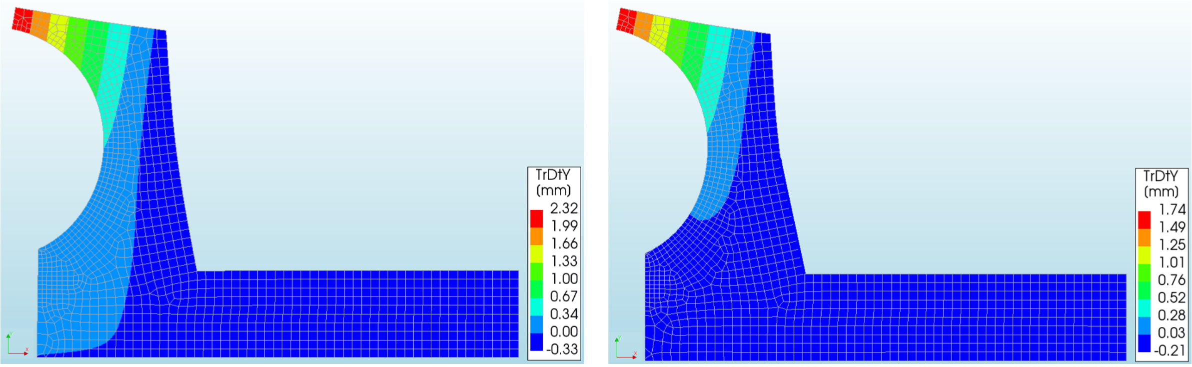

(c) Contour plot of displacements in y-direction, unsupported wall.

(d) Contour plot of displacements in y-direction, supported wall.

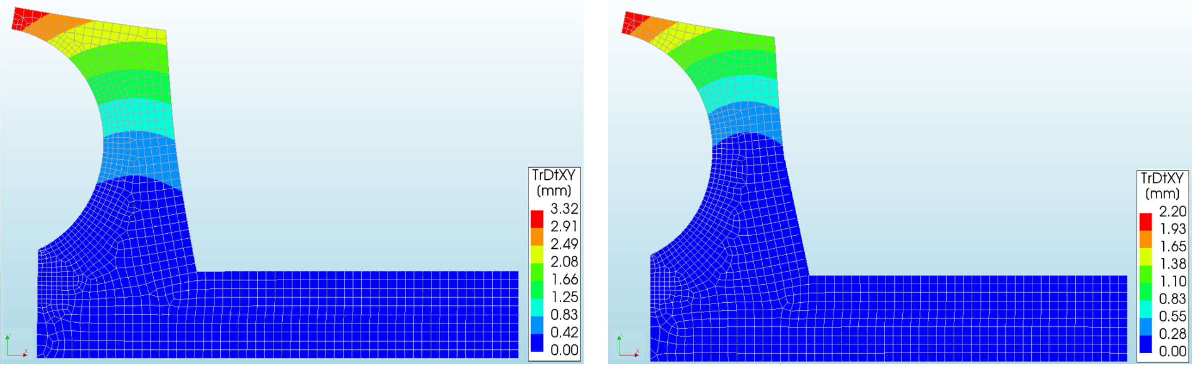

(e) Contour plot of displacements in xy-direction, unsupported wall.

(f) Contour plot of displacements in xy-direction, supported wall.

Figure B.5: Contour plots of displacement for the unsupported (to the left) and supported (to the right) crownwalls at the moment of maximum pressure of W7.

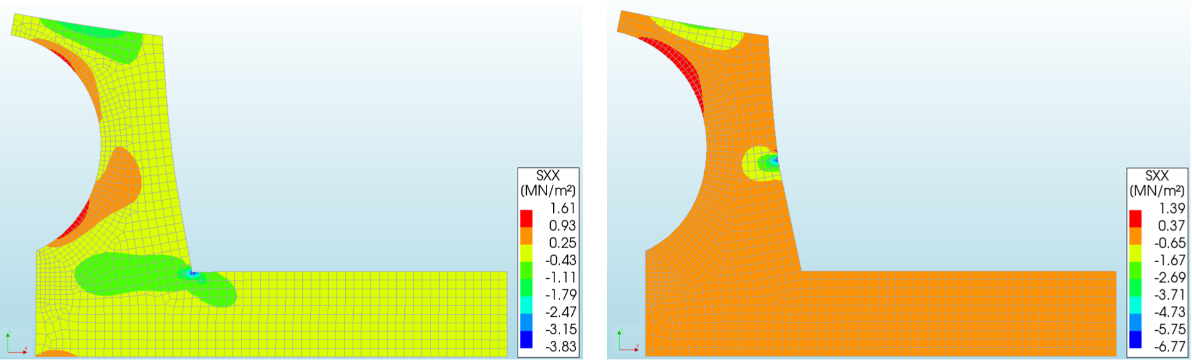

(a) Contour plot of stresses in x-direction, unsupported wall.

(b) Contour plot of stresses in x-direction, supported wall.

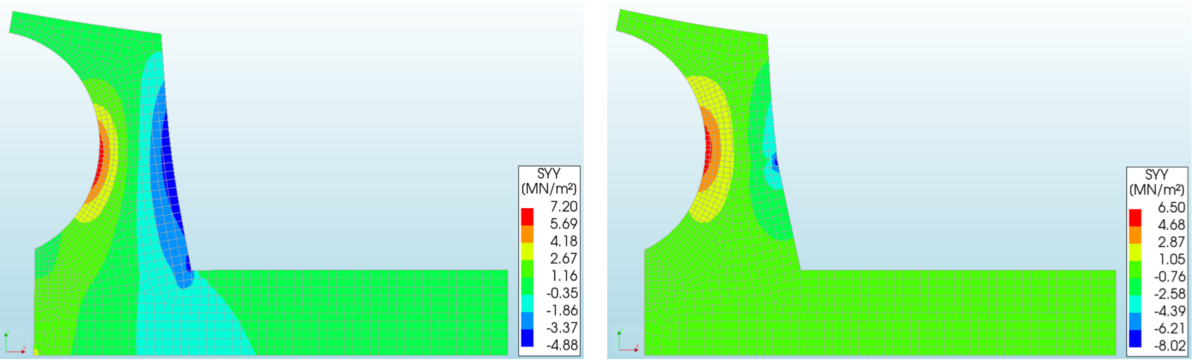

(c) Contour plot of stresses in y-direction, unsupported wall.

(d) Contour plot of stresses in y-direction, supported wall.

Figure B.6: Contour plots of stresses for the unsupported (to the left) and supported (to the right) crownwalls at the moment of maximum pressure of W7.

C

Stability

The following unity checks need to be fulfilled in order for the crownwall to be resistant to sliding (equation C.1) and overturning (equation C.2).

$$\frac{\mu W}{F_{T,H}} > 1 \tag{C.1}$$

$$\frac{M_W}{M_{F_{T,V}} + M_{F_{T,H}}} > 1 \tag{C.2}$$

Here, μ is the friction coefficient, W is the self-weight of the crownwall, $F_{T,V}$ and $F_{T,H}$ are the maximum vertical and horizontal wave force, M_W is the bending moment of the self-weight about point A in figure C.1 and $M_{F_{T,V}}$ and $M_{F_{T,H}}$ are the bending moments by the vertical and horizontal wave forces. All forces are indicated in figure C.1. It is assumed that the interface between the concrete caisson and the crownwall is a rough interface with a friction coefficient $\mu = 0.7$ (EN 1992-1-1, 2004). Table C.1 and C.2 show the results of the stability calculations. The width of the additional supporting wall is unknown but based on photos from Civitavecchia harbour it is assumed to have a width of 2m. The weight of the additional wall is accounted for in the self-weight of the supported crownwall.

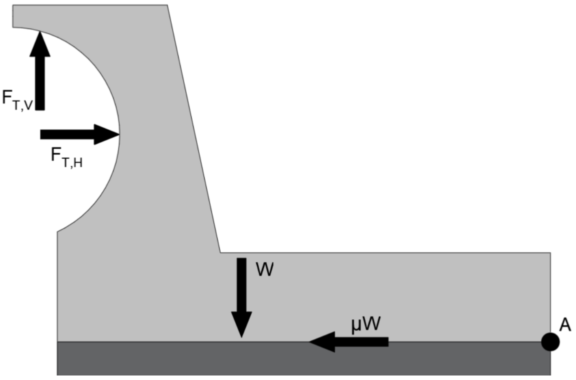

Figure C.1: Stability of crownwall. $F_{T,V}$ and $F_{T,H}$ are the vertical and horizontal components of the total wave force, W is the self-weight of the crownwall and μW is the friction force. The bending moments are taken at point A.

Table C.1: Sliding results.

Crownwall	Wave state	H [m]	T [s]	$F_{T,H}$ [kN]	W [kN]	μW [kN]	Unity check [-]
Unsupported	W5	5	8	455	830	580	1.3 > 1
	W6	6	8	1095			0.5 < 1
	W7	7	11	1400			0.4 < 1
Supported	W5	5	8	455	960	670	1.5 > 1
	W6	6	8	1095			0.6 < 1
	W7	7	11	1400			0.5 < 1

Table C.2: Overturning results.

Crownwall	Wave state	H [m]	T [s]	$M_{F_{T,V}}$ [kNm]	$M_{F_{T,H}}$ [kNm]	M_W [kNm]	Unity check [-]
Unsupported	W5	5	8	1010	1700	5810	2.1 > 1
	W6	6	8	2900	4410		0.8 < 1
	W7	7	11	5000	5780		0.5 < 1
Supported	W5	5	8	1010	1700	6625	2.4 > 1
	W6	6	8	2900	4410		0.9 < 1
	W7	7	11	5000	5780		0.6 < 1

Based on these preliminary hand calculations on sliding and overturning, the fully curved crownwall will slide and rotate under wave loading of W6 and W7, even when the additional supporting wall is included. In order to resist sliding under the wave load of W7, the crownwall will have to have more than double its current self-weight.